Colossal creations of gravity

From clusters of galaxies to active galactic nuclei

Andreas Skielboe

Dark Cosmology Centre, Niels Bohr Institute
University of Copenhagen

This thesis has been submitted to the
PhD School of SCIENCE, University of Copenhagen
for the degree of
Doctor of Philosophy

October 2016

This thesis is dedicated to my loving parents.

Acknowledgements

The work presented in this thesis would not have been possible without the support and inspiration of my family, friends and co-workers. In particular, I would like to thank all the staff and students of the Dark Cosmology Centre, for having created and maintained one of the best research environments in the world. I also extend my sincere gratitude to the Astronomy and Astrophysics group at the University of California, Santa Barbara for having hosted me during creation of major parts of this work. In particular, I am grateful to Tommaso Treu and Anna Pancoast for being exceptionally friendly and helpful during my stay. I thank my supervisors Kristian Pedersen and Darach Watson for being good friends and for being patient and honest throughout my PhD studies. Mia Lind deserves thanks for being patient with me and for proof reading parts of the manuscript. Finally, I thank all my friends and family for always being loving and supportive.

Abstract

Gravity governs the evolution of the universe on the largest scales, and powers some of the most extreme objects at the centers of galaxies. Determining the masses and kinematics of galaxy clusters provides essential constraints on the large-scale structure of the universe, and act as direct probes of cosmological models, through the cluster mass function. Here, I present the first ever measurement of anisotropic kinematics in clusters of galaxies, providing evidence for anisotropic structure formation, and allowing assessment of systematics in galaxy cluster catalogs. While clusters of galaxies are the largest bound structures, supermassive black holes in active galactic nuclei (AGN) are the most massive compact objects. Probing the structure of AGN through reverberation mapping allows independent measurements of supermassive black hole masses. The masses of black holes in AGN have been shown to correlate with properties of the AGN host galaxy across orders of magnitude. In addition, black hole masses scale with the intrinsic luminosity of the AGN, suggesting that AGN can be used as independent distance probes for cosmology. Improving understanding of the structure of AGN paves the way for improved black hole mass measurements, as well as AGN cosmology. Here, I develop a new method for probing the structure of AGN using reverberation mapping. The method is based on regularized linear inversion with statistical modeling of the light curves. The method is applied to five nearby AGN, yielding velocity-resolved response maps for the Hβ emission line. The results can be compared to physical models of the broad emission line region in AGN, improving our understanding of active galaxies. While useful for studying AGN structure in individual objects, spectroscopic reverberation mapping campaigns require high cadence spectroscopy to isolate broad line emission from the underlying AGN continuum. This makes traditional reverberation mapping prohibitively expensive at higher redshifts $\gtrsim 1$, where the time delays between variations in the continuum and broad line emission is of the order of years. To address this issue, new methods for photometric reverberation mapping have recently been developed. I test the method of photometric reverberation mapping on data obtained from three nearby AGN, and discuss the possibility of using photometric reverberation mapping to constrain scaling relations at high redshift. These results show that photometric reverberation mapping can be a useful and cheap alternative to traditional spectroscopic reverberation mapping campaigns.

Table of contents

Chapter 1

Introduction

1.1 Gravity and the advent of physical cosmology

The study of gravity and its description, introduced by Newton (1687), as a fundamental force of universal gravitation, has profoundly changed the way in which we view the cosmos. Gravity governs everything from the motions of planets, over the formation of stars and galaxies to the evolution of the large-scale structure of the universe. The discoveries initiated by Einstein 100 years ago, revealed that gravity is much more than just another force of nature. In his theory of general relativity, Einstein describes gravity as the curvature of spacetime around massive objects, where objects move along geodesics in spacetime, which are the equivalent of straight lines in curved space (Carroll, 2004). The idea, that mass curves space, and that the curvature of space in turn determines how mass moves, is a radical departure from the classical view of spacetime as a static, flat backdrop on which the events of the universe occur (Wheeler, 1990).

The development of general relativity in the early 20th century also sparked the field of physical cosmology. Cosmology is the study of the origin, evolution and fate of the universe (Ellis, 2006). Because gravity is the only force relevant over cosmological distances[1], it is gravity that ultimately determines how the universe evolves (Dodelson, 2003). When Einstein published his papers on general relativity, it was generally believed that the universe was static (Bruno, 1584). But even Newton recognized that a universe filled will matter is unstable to gravitational collapse (Newton, 1692). Einstein's general relativistic cosmology did not provide a natural solution to this problem. Instead, to match the observations of a static universe, Einstein introduced a cosmological constant, Λ, into his equations, designed

[1]The strong and weak nuclear forces only act on atomic scales, and the universe is electromagnetically neutral on large scales, so the only relevant force on cosmological scales is gravity.

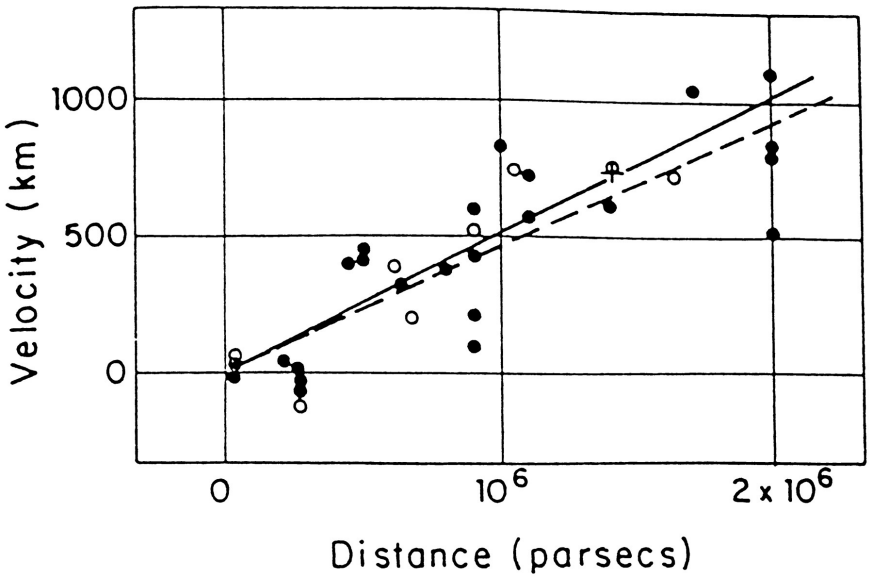

Fig. 1.1 Hubble's original diagram showing evidence for cosmological expansion. Reproduced from Hubble (1929).

to exactly balance the contractive force of gravity on cosmological scales, and prevent the universe from collapsing under its own weight (Einstein, 1917).

In the 1920s, Lundmark (1924) and Hubble (1929) presented evidence, based on earlier observations by Slipher (1915), that the redshift of galaxies increases with distance. The adopted explanation for the redshifts of galaxies is that, instead of being static, the universe is in fact expanding (Lemaître, 1927). The redshifts of galaxies can then be interpreted as Doppler shifting of the light traveling to us from far away galaxies, caused by the radial velocities of the galaxies induced by the expansion of spacetime (Bunn & Hogg 2009, but see also Chodorowski 2011; Kaiser 2014). Hubble's plot, known as a Hubble diagram (Fig. 1.1), indicates a constant local expansion. Because the data is limited to nearby sources, it poses few constraints on large-scale cosmological dynamics (Livio & Riess, 2013). The discovery of the cosmological expansion has had tremendous consequences for the development of physical cosmological models. The fact that the universe seemed to be expanding prompted Einstein to reconsider his cosmological constant, leading to the Einstein-deSitter model in which the universe is assumed to be flat and forever expanding, with no cosmological constant ($\Lambda = 0$) and the matter density exactly balancing the cosmological expansion (Einstein & de Sitter, 1932).

Contemporary standard models of cosmology are based on the assumption that, on large scales, the universe is homogeneous and isotropic. This idea is known as the cosmological principle, and allows the derivation of an exact solution to the Einstein equations for general

relativity, called the Friedmann–Lemaître–Robertson–Walker (FLRW) metric of spacetime (e.g. Robertson, 1935):

$$\mathrm{d}s^2 = -c^2\mathrm{d}t^2 + a^2(t)\mathrm{d}\Sigma^2, \tag{1.1}$$

where c is the speed of light, t is the time coordinate, a is the scale factor and Σ represents the spatial coordinates, which depend on the chosen coordinate system as well as the overall curvature of the universe. In the FLRW metric the scale factor $a(t)$ describes the relative size of the universe at two times, and formalizes uniform cosmological expansion (or contraction if $\mathrm{d}a/\mathrm{d}t < 0$). When combined with the Einstein equations, the FLRW metric provides time evolution equations for the scale factor $a(t)$, as a function of the matter and energy content of the universe (Carroll, 2004). These equations, describing the dynamics of the universe, are called the Friedmann equations (Friedmann, 1922). They allow us to compare observations of the expansion of the universe with different cosmological theories, containing varying amounts of matter and energy.

In the late 1990's two observational surveys of supernovae, measuring the expansion of the universe, radically altered the picture of a steadily expanding universe that had persisted since Slipher's observations 75 years earlier. Two separate groups, lead by Saul Perlmutter and Brian Schmidt, presented evidence that, rather than expanding at a constant rate, the expansion of the universe is accelerating (Schmidt et al., 1998; Perlmutter et al., 1999). This discovery leads to the profound conclusion that whatever makes the universe expand, is still around to this day. The accelerated expansion of the universe seems to be very accurately described by the exact same cosmological constant that Einstein had introduced years earlier, to reconcile a finite mean density with a static universe. Contemporary cosmological theories thus include a cosmological constant as an energy component of the universe (Copeland et al., 2006). The cosmological constant Λ enters the Friedmann equations with the equivalent of a negative pressure, producing uniform accelerated expansion, unlike any type of matter or energy otherwise known. For lack of a more accurate term, and because of the way it enters in the equations, we label this unknown type of negative pressure "dark energy" (Peebles & Ratra, 2003). The simplest form of dark energy is not diluted during cosmological expansion, i.e. the dark energy density is a constant $\mathrm{d}\rho_\Lambda/\mathrm{d}t = 0$. This points to dark energy being a fundamental property of spacetime, rather than a classical soup of particles. It also means that dark energy becomes more important as the universe expands. In our universe, the transition to dark energy dominated expansion occurred around 10 billion years after the Big Bang, and today dark energy is the dominant factor governing the cosmological evolution (e.g. Ryden, 2003).

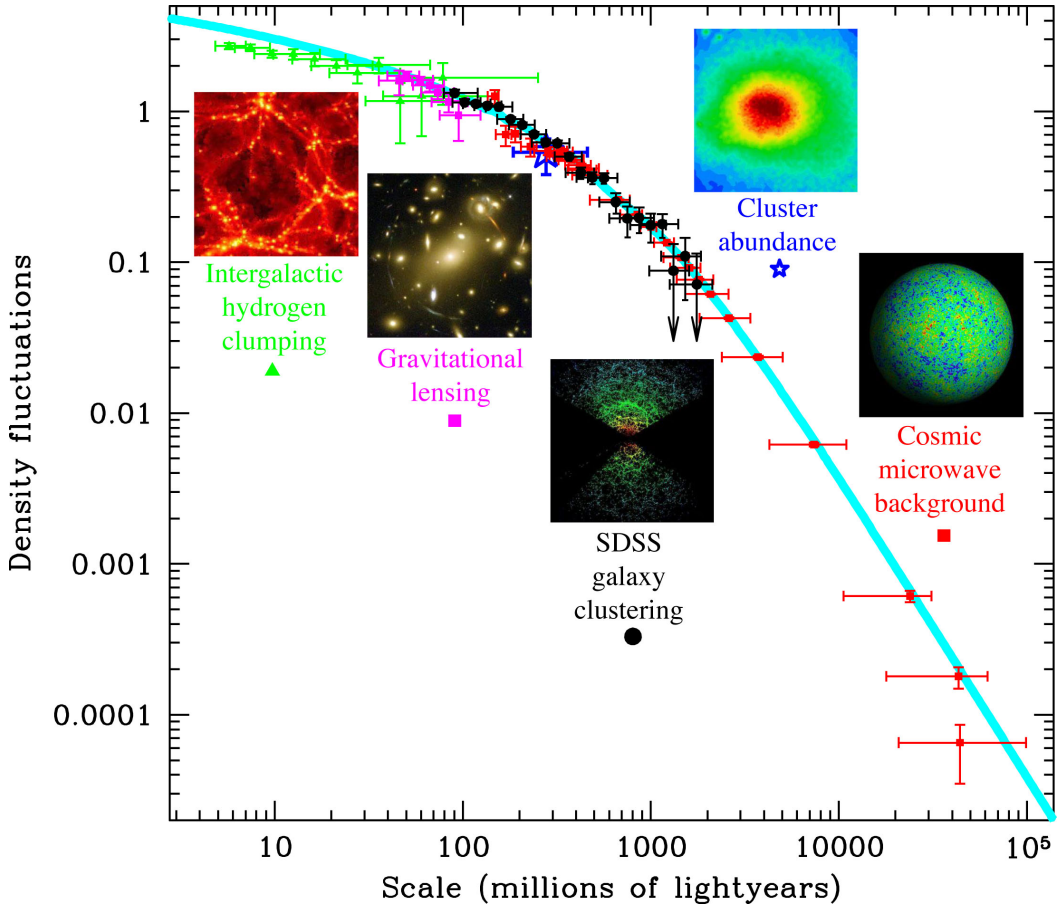

Fig. 1.2 Measuring the amount of "stuff" in the universe at different scales allows us to constrain cosmological models. This figure shows measured density fluctuations in the universe on different scales, and the blue band shows the prediction from the standard model of cosmology in a universe consisting of 5 % atoms, 25 % dark matter and 70 % dark energy (source: http://space.mit.edu/home/tegmark/sdss.html).

The expansion history of the universe has important consequences for how structure forms, and therefore determines the scale at which different types of structure exist. By measuring the distribution of structure in the universe on large scales we can compare to predictions from cosmological models, and constrain the parameters governing the constituents of the universe, including dark energy and dark matter (e.g. Weinberg et al., 2013), see Fig. 1.2. The largest structures in the universe are clusters of galaxies, which provide excellent laboratories for studying cosmology and formation of structure. At the other end of the scale we find supermassive black holes, which are the most massive compact objects in the universe. Like clusters, supermassive black holes provide unique insights into the nature of gravity and are important for the studying the formation and evolution of galaxies.

This thesis explores the observational evidence of gravitationally powered phenomena on the largest scales of structure in the universe; dominated by clusters of galaxies, and in the environments of the most extreme compacts objects; those around supermassive black holes in the centers of galaxies. In the following introduction I will describe how supermassive black holes are intimately linked to the evolution of galaxies through feedback mechanisms, and how they may play a role in galaxy clusters, by providing an energy source to heat the intra cluster medium. Studying the evolution of clusters of galaxies, informs us about the evolution of the universe as a whole, and studying supermassive black holes provides constraints on structure formation and galaxy evolution.

In the following sections I will introduce our current understanding of clusters of galaxies and supermassive black holes in active galactic nuclei (AGN). While they may look simple to the outside observer, they are both exceedingly rich in structure and physical phenomena. The introduction provides a short review of the physics of clusters and supermassive black holes, as well as our understanding of their mutual relationship. The subsequent chapters will dive into specific topics on the kinematical properties of clusters of galaxies, and techniques for studying the detailed structure surrounding supermassive black holes. These efforts will help us understand each of these types of objects individually, how they influence each other, and how they shape the history of the universe in which we live.

1.2 Clusters of galaxies

Clusters of galaxies are among the largest gravitationally bound structures in the universe. They appear on the sky as overpopulations of galaxies, containing between 10s of galaxies in groups, up to several 1000s of galaxies in the largest clusters (Abell, 1958; Zwicky et al., 1968; Koester et al., 2007; Rykoff et al., 2014). Galaxy clusters were first observed as concentrations of galaxies (called nebulae at the time) on the sky, while their interpretation as clusters of galaxies only came much later, after it was discovered that the nebulae were in fact galaxies (for a review see Biviano, 2000). Studies of the distribution of clusters revealed locally non uniform distributions, with most galaxies inhabiting groups and clusters, and many clusters inhabiting larger superclusters (Abell, 1962; Peebles, 1974). This provides early evidence for the current picture of structure formation by hierarchical clustering, in which structure forms on small scales first, and then gradually build up through merging events (Peebles & Dicke, 1968; Gott & Rees, 1975; Springel et al., 2005).

Zwicky (1933) provided the first estimate of the mass of a galaxy cluster, and showed that it was many times greater than the mass that could be accounted for by galaxies. This was the first evidence that a source of gravitation was missing from our models of the universe, and

lead to the theories of dark matter and modified gravity to explain the issue of the missing matter. An issue which has not been resolved to this day (for recent reviews see Bertone et al., 2005; Capozziello & de Laurentis, 2011).

That galaxy clusters are complex structures themselves, and not just collections of galaxies, becomes apparent when they are observed in X-rays (Giacconi et al., 1972). Rich galaxy clusters are bright X-ray sources, with spatially extended emission (for a review see Sarazin, 1986). The source of the X-ray emission is consistent with thermal bremsstrahlung from a hot (10^8 K) gas, called the intracluster medium (ICM), with a total mass greater than of all the galaxies in the cluster. The origin of the gas is unknown, but the abundance of metals in the gas suggests that a significant fraction has to have been reprocessed in stars, and so must come from galaxies (Serlemitsos et al., 1977; Baldi et al., 2007; Leccardi & Molendi, 2008).

While the mass of galaxy clusters is dominated by dark matter and the ICM, the electromagnetic emission is dominated by the cluster member galaxies. Studying the morphology, distribution and kinematics of cluster galaxies thus provides important clues to how clusters are formed, as well as how clusters, and the galaxies in them, evolve over time.

1.2.1 Galaxies in clusters

Compared to the field, galaxy clusters has an overrepresentation of early type elliptical and lenticular galaxies. The spatial distribution is furthermore segregated, with early type galaxies occupying the central regions of the cluster, while late type spiral galaxies are found more commonly in the outskirts of the cluster. The central regions in massive clusters are almost completely devoid of spiral galaxies (Dressler, 1980; Tanaka et al., 2005). Kinematically, early and late type galaxies in clusters also differ, with spiral galaxies tending to have significantly larger velocity dispersions compared with early type galaxies (e.g. Colless & Dunn, 1996).

The morphological segregation between cluster galaxies and field galaxies means that galaxies in clusters are less star forming, redder and has less neutral gas and dust (prerequisites of star formation). The fact that clusters contain mostly elliptical, non-star-forming galaxies, with smaller velocity dispersions compared to spirals, provides important clues to the formation and evolution of galaxy clusters. The primary interpretation of galaxy type segregation in clusters is that cluster ellipticals and spheroidals are remnants of spiral galaxies that have been perturbed and stripped from their outer layers of gas. The large sizes of some ellipticals in clusters, especially the central cluster galaxies, suggests that these have been formed by a combination of merging and outer gas stripping, with previous periods of active star formation as a result (for a review see Boselli & Gavazzi, 2006).

Interactions between galaxies in clusters are typically short lived due to the large velocities of cluster members. Galaxies falling in from the field may already be members of smaller galaxy groups where they will have been involved in close encounters with other galaxies. Because groups of galaxies are less massive than clusters, the galaxy velocity dispersion in groups is correspondingly smaller, leading to longer timescales for galaxy-galaxy interactions. The process of perturbing spiral galaxies, before they fall in to join a galaxy cluster, is known as preprocessing. While preprocessing may play a role in inducing star formation in spiral galaxies, and help remove some gas, the presence of spirals in galaxy clusters means that preprocessing cannot explain the large deficiency of late type galaxies in cluster cores. The explanation for this must be found in the physical process taking place inside the clusters themselves (Abadi et al., 1999; Fujita, 2004; Cortese et al., 2006; Blanton & Moustakas, 2009). This prompts us to look elsewhere for mechanisms to explain how late type galaxies may loose their gas, turning into early type galaxies in clusters.

The pressure of the ICM of massive clusters can be large enough to overcome the gravitational binding energy of extended gas in galactic haloes, in a process known as ram pressure stripping (Vollmer et al., 2001; Roediger & Hensler, 2005). Even when the ICM pressure cannot overcome the binding energy of the gas, it can still exert friction that drags gas out of the in-falling galaxy, albeit less efficiently than ram pressure stripping (Boselli & Gavazzi, 2006).

Removing the outer gas in galaxies has the effect of steepening the gravitational potential, which can drive gas into the center of the galaxy, inducing star formation and fueling the supermassive black hole in the center of the galaxy. The combination of increased star formation and AGN feedback may accelerate the speed at which neutral gas is depleted from the galaxy, pushing it further back the Hubble sequence, closer to the bona fide members of massive galaxy clusters (Byrd & Valtonen, 1990; Balogh et al., 2000). Formation and evolution of galaxy clusters is thus a complicated process, involving many physical mechanisms.

1.2.2 AGN feedback in clusters of galaxies

AGN activity plays an important role in clusters of galaxies. First of all they are part of the evolution of cluster members, where they take part in AGN galaxy feedback mechanisms, driving gas out of the galaxy in large scale outflows, depleting gas reservoirs required for star formation (Schawinski et al., 2007; McCarthy et al., 2010). Depending on the geometry and energy, outflows from AGN can also trigger star burst events by compressing the IGM in the outflow to densities required for gravitational collapse (Ishibashi & Fabian, 2012; Silk, 2013). Star bursts from AGN feedback, and gas removal by AGN outflows, both have the

effect of depleting the IGM in cluster galaxies. In time, this will drive the cluster members towards early types in the Hubble sequence, consistent with the observation that clusters contain mostly early type galaxies.

Besides taking part in galaxy evolution, AGN may play a role in determining the structure of the cluster as a whole, by providing a mechanism for transferring energy to the ICM (Planelles et al., 2014). The X-ray emission from the ICM in clusters cools the gas by radiating energy. If no energy is added to the gas it will cool rapidly, and fall to the cluster center. This is seemingly incompatible with the fact that we do not observe cool X-ray emission from clusters of galaxies. This inconsistency is called the cooling flow problem (Fabian, 1994). One of the possible explanations is that AGN activity in the central regions of the cluster deposit energy back into the ICM, pointing to a direct connection between supermassive black holes and clusters of galaxies (Yang & Reynolds, 2016, and references therein).

Studying how AGN activity can be stimulated by increased availability of fuel, and how AGN outflows affect the host galaxy, is important in understanding how galaxies evolve in general, and in cluster environments in particular. In order to understand how AGNs are fueled and how outflows are formed, we have to understand the structure of the AGN itself (Section 1.3).

1.2.3 Clusters as dark matter laboratories

Around the time that the cosmological expansion was discovered, Fritz Zwicky was studying redshifts of galaxies in clusters (Zwicky, 1933). By identifying the part of the redshift of galaxy cluster members associated with peculiar velocities[2] he was able to estimate the total gravitational potential of the cluster. Zwicky's discovery initiated a completely new branch of astrophysical research. Zwicky's observations showed that, while galaxies dominate the emission of clusters at optical wavelengths, they constitute only about one percent of the total matter content in clusters. Another $\sim 9\,\%$ is in the form of the hot ICM (Cavaliere et al., 1971), while the bulk of the mass $\sim 90\,\%$ cannot be associated with any known form of matter. This unknown matter component completely dominates the gravitational potential of the universe at large scales, and is called "dark matter" (for a review see Bertone et al., 2005).

The large quantities of dark matter in galaxy cluster haloes, make clusters compelling laboratories for probing the nature of dark matter. Interactions of merging galaxy clusters pro-

[2]The peculiar velocity of an object is the objects true velocity with respect to a given point of reference. In the case of galaxies in cluster the most meaningful point of reference is often the center of mass, or the minimum of the potential, which is selected observationally as the position of the brightest galaxy in the cluster.

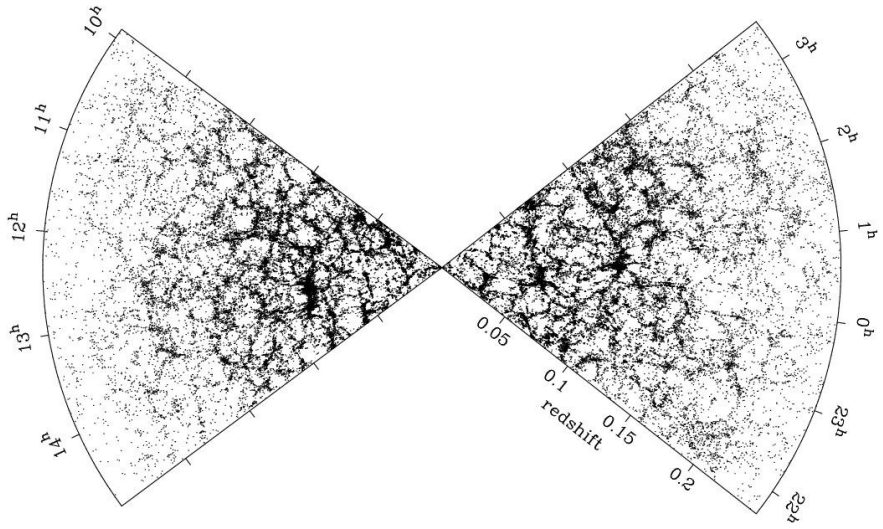

Fig. 1.3 The cosmic web as pictured from cosmological redshifts of more than 200,000 galaxies observed in the 2dF survey. Figure from Reshetnikov (2005).

vide direct evidence for dark matter, and puts concrete limits on dark matter self-interaction (Clowe et al., 2004; Markevitch et al., 2004; Clowe et al., 2006; Bradač et al., 2008; Harvey et al., 2015), while measurements of gravitational redshift in galaxy clusters help distinguish different dark matter models and alternative theories of gravity (Wojtak et al., 2011).

1.2.4 Clusters as cosmological probes

In order to study the evolution of the large-scale structure of the universe, and the nature and role of dark matter in the formation of structure, we have to understand the dynamics of galaxy clusters. Galaxy clusters are not just among the largest structures in the universe (challenged only by gravitationally unbound superclusters) they are also the clearest observable constituents of the cosmic web (Peebles, 1980). The cosmic web is a term given to the distribution of matter on cosmological scales (see Fig. 1.3) and which, together with the cosmic microwave background radiation, provides the most direct observational link to the creation of the universe (Eisenstein et al., 2005; Voit, 2005).

Calculating masses for clusters of galaxies provides an absolute mass scale for the largest structures of the universe. This scale can be used to calibrate and constrain cosmological models, describing the state and evolution of the very early universe, as well as the formation and evolution of the large-scale structure. Besides total cluster masses, ICM gas fractions and cluster pressure profiles can be used to constrain cosmological models by providing absolute distance measures to galaxy clusters (Allen et al., 2013).

1.2.5 Systematics in galaxy cluster mass measurements

In order to understand the dynamics and evolution of clusters of galaxies, as well as using clusters for high precision cosmology, it is important to understand and control systematics associated with measurements of cluster properties. It is typically assumed that clusters are spherical and dynamically relaxed, but simulations and observations show that this is often not the case (Binggeli, 1982; Limousin et al., 2013). Failure to address these issues may lead to biased estimates of cluster masses, which propagates to cosmological parameters derived from cluster mass functions (Corless & King, 2009; Meneghetti et al., 2010; Becker & Kravtsov, 2011).

When weighing clusters by measuring density profiles of the X-ray emitting ICM (Sarazin, 1986), the main assumption is that the gas is spherically symmetric (e.g. Ettori et al., 2002). The first order extension to sphericity is to allow one axis to be a different length than the others. Even if the overall change in the derived cluster parameters can be significant, constraining the shape when the cluster is non-spherical turns out to be rather difficult. The reason is that we cannot measure the shape of the X-ray emitting gas along the line of sight directly.

The issue of constraining the three dimensional shape of galaxy clusters was the topic of work I did in collaboration with Johan Samsing and Steen Hansen, and which is published in Samsing et al. (2012). We address the issue by probing the departure from sphericity by measuring subtle deviations in the X-ray gas temperature profiles in the plane of the sky. By assuming functional forms for the radial gas profiles we attribute any measured deviation therefrom to a non-spherical gas distribution. While this is a somewhat idealized case, it nonetheless provides an estimate of the degree of bias to be expected in cluster measurements assuming spherical matter distributions. We find that departure from sphericity can amount to about 10 % error on derived cluster masses, which in the era of high precision cosmology may lead to biased parameter constraints. This works highlights the importance of understanding ensemble galaxy cluster properties if we hope to use galaxy clusters as competitive cosmological probes.

1.2.6 Revealing signatures of cluster formation

Galaxy redshift surveys, such as the Sloan Digital Sky Survey (SDSS) and the (Two-degree-Field Galaxy Redshift Survey (2dF), provide stunning maps of the matter distribution in the universe, revealing the results of billions of years of cosmological evolution (Fig. 1.3). This snapshot of the fabric of the cosmos is given life by the addition of velocity information, adding a time dimension to our view of the universe. Because tangential velocities are

impossible to measure, except for very nearby objects, we rely on the line of sight velocity determined from the redshift of the object. The redshifts of far-away galaxies are dominated by the Hubble flow, the cosmological expansion of the universe, so unless we know the exact distance to the galaxy it is nigh impossible to constrain its peculiar velocity. The peculiar velocity is required to map the local velocity field around the galaxy, and without a well-defined frame of reference this mapping is meaningless.

In cluster of galaxies this is a different story. Because clusters are bound objects, the member galaxies will follow a velocity distribution defined by the potential of the cluster. If the cluster potential exhibits axial symmetries, the galaxy velocity distribution integrated along potential symmetry axes will also be symmetric. If we define a reference frame of the cluster, we can measure the galaxy line-of-sight velocity distributions in the frame of the cluster, and thereby identify member galaxies, as well as constrain properties of the cluster by studying the galaxy velocity distributions (Danese et al., 1980).

In Chapter 2 I present the first ever measurement of anisotropic kinematics in the line of sight velocity distributions in a stack of galaxy clusters from SDSS. The clusters are selected to have similar masses and redshifts, and the cluster member line-of-sight velocities are added to two distinct bins, according to their azimuthal position relative to the cluster halo major axis, estimated from the orientation of the central galaxy by assuming preferential alignment with the underlying cluster halo (Niederste-Ostholt et al., 2010). This provides a unique window into cluster formation, and points to anisotropic accretion of matter onto clusters, consistent with results from numerical simulations, which indicate clusters accrete mass primarily through large-scale structure filaments (e.g. Colberg et al., 1999). Probing galaxy cluster anisotropies thus yield insights into the formation and evolution of not only galaxy clusters, but the large-scale evolution of the universe. In addition, it provides important statistical means by which biases of clusters surveys can be assessed.

1.3 Active galactic nuclei

While clusters of galaxies make up the largest structures in the universe, black holes represent the most compact objects. So compact in fact, that until this day they have defied a consistent physical description, and posed challenges to the fundamental laws of nature. These mysterious regions of spacetime epitomize the ultimate display of the power of gravity. Formation of black holes is the consequence of increasing the local energy density to such an extent that the curvature of spacetime around the black hole bends all geodesics back towards the singularity at the center. Formation of black holes represents a fundamental departure

from classical physics, and their existence exemplify challenges in unifying gravity with the other fundamental forces of nature.

Observations indicate that most, if not all, galaxies host a supermassive black hole at the center. When matter falls inside the gravitational sphere of influence of the black hole, it can settle into bound orbits around the black hole. In order for orbits to be stable near the black hole, the matter will have to achieve very large orbital velocities, and the kinetic energy can be converted to thermal energy by internal friction in the turbulent accretion flow (for a review see Blaes, 2014). When the gas is heated sufficiently its thermal radiation peak will move to shorter wavelengths in the electromagnetic spectrum, and the active galactic nucleus becomes visible in the optical and UV (Salpeter, 1964; Wagoner, 1969; Rees, 1984). This conversion of gravitational energy to thermal radiation can be very effective, up to a point where the radiation pressure overcomes the gravitational potential of the black hole, and the accretion flow is impeded at the Eddington Limit (Eddington, 1926).

Supermassive black holes in the centers of galaxies, in an active accretion mode, are known as active galactic nuclei (AGN), and are the most persistently luminous objects in the Universe (Kormendy & Richstone, 1995; Miyoshi et al., 1995; Tanaka et al., 1995). AGN spectra are characterized by broad and narrow emission lines, on top of a strong power law continuum, extending across the electromagnetic spectrum (Fig. 1.4). Some AGN feature strong radio emission, associated with relativistic jets, and possibly powered by interaction between accretion flow magnetic fields and black hole spin (Blandford & Payne, 1982; Begelman et al., 1984; Urry & Padovani, 1995).

While all galaxies likely host supermassive black holes, some of which are active nuclei, not all active galaxies look the same. Some feature narrow as well as strong broad emission lines, as seen in the composite in Fig. 1.4, and are named Seyfert 1 galaxies, after Seyfert (1943). Other AGN show no broad emission, but only narrow emission lines, and are called Seyfert 2 galaxies. Some have parsec scale jets and strong radio emission, while others are radio quiet (Urry & Padovani, 1995; Zensus, 1997; Tadhunter, 2016).

1.3.1 The AGN unification paradigm

Much effort has gone into the development of unified models of AGN, to reconcile the diversity in emission properties (Antonucci, 1993; Elvis, 2000; Netzer, 2015). These models generally suggest a picture in which the accretion flow is in the form of an accretion disk surrounding the black hole (see Fig. 1.5). The radial extent of the disk explains the thermal temperature gradient responsible for generating continuum emission, while the disk structure explains how the disk can efficiently cool and how the cooling emission can escape the nucleus without being absorbed and impede the accretion flow.

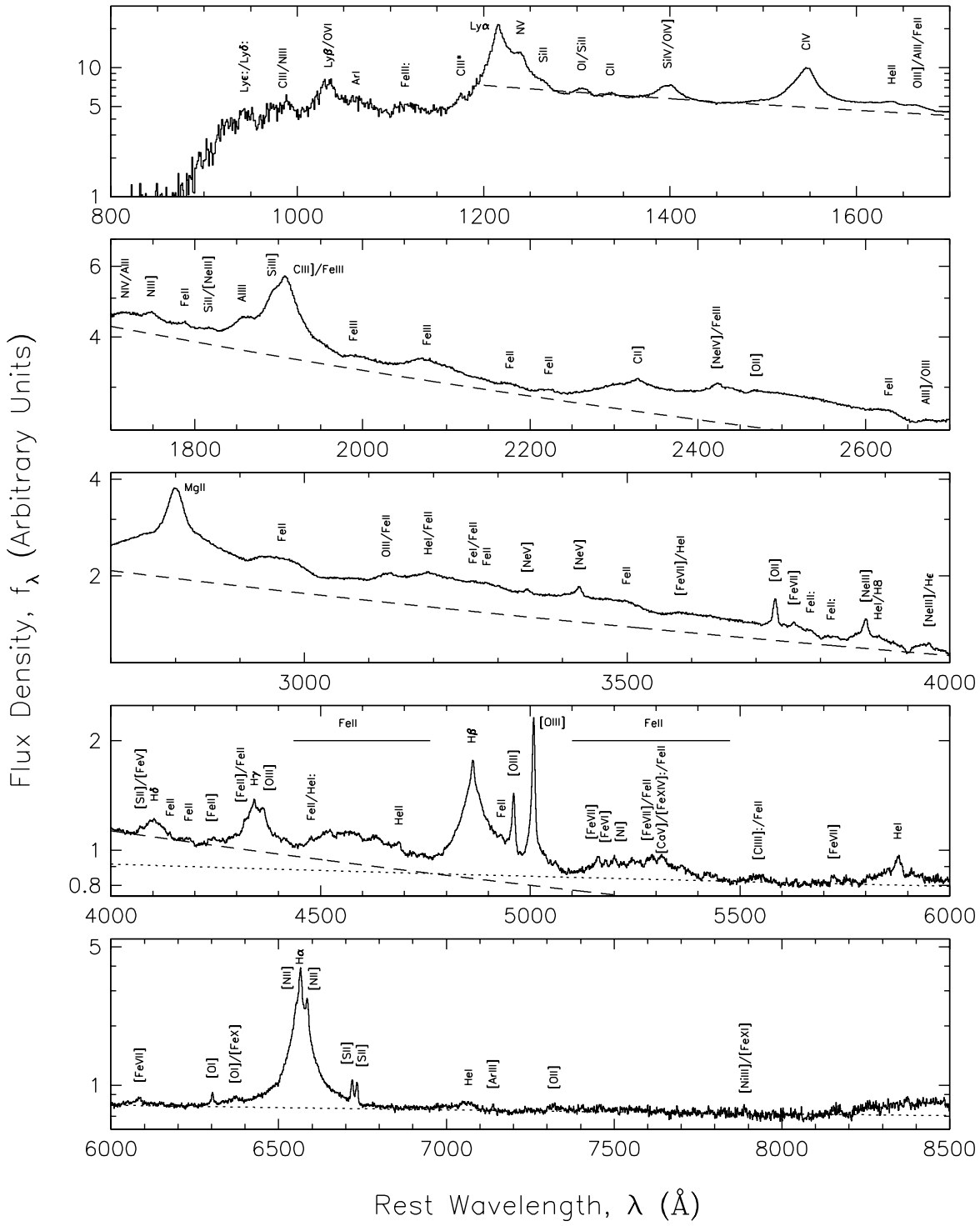

Fig. 1.4 Quasar / Seyfert 1 composite spectrum from SDSS. Reproduced from Vanden Berk et al. (2001).

While the accretion disk can in principle extend all the way to the innermost stable circular orbit (ISCO), the broad recombination lines observed in Seyfert 1 galaxies are associated with a distinct broad emission line region (BLR). The continuum and emission lines in AGN are observed to vary on timescales of days to years (Ulrich et al., 1997), and the broad emission follows the continuum emission closely, suggesting that the BLR is ionized by the continuum radiation from the accretion disk. The narrow emission lines, on the other hand, are largely non variable on short time scales, but have been shown to respond to continuum variations on time scales of years (Peterson et al., 2013). The narrow lines are associated with a distinct narrow line region (NLR), with lower densities and lower temperatures, manifested in the presence of forbidden lines, such as the strong [O III] lines (see Fig. 1.4), that are collisionally suppressed in the BLR (Mathews et al., 1980). The NLR is the only component of AGN resolved in optical observations (Wilson & Heckman, 1985).

Unification models attempt to reconcile differences between Seyfert 1 and Seyfert 2 galaxies, by suggesting that broad emission exists in the latter, but is obscured by an absorbing medium in the line of sight, or otherwise suppressed by low accretion activity. The simplest form of an obscuring medium is perhaps a dense dusty torus surrounding the nucleus, implying that Seyfert 2 galaxies are in fact Seyfert 1 galaxies observed at different inclinations (see Fig. 1.5). This picture is supported by observations of electron scattered broad emission observed in Seyfert 2 galaxies (Heisler et al., 1997; Ramos Almeida et al., 2016).

That inclination is not the only relevant parameter in AGN unification is demonstrated by observations indicating that AGN structure can change with AGN luminosity. This may explain why Seyfert 1 and Seyfert 2 galaxies look different, and provide a natural origin for the intrinsic scatter observed in AGN scaling relations (Kaspi et al., 2005; Bian & Gu, 2007). That AGN structure is related to luminosity is also corroborated by observations of Seyfert galaxies with unusually narrow broad emission lines. These objects are called narrow line Seyfert 1 galaxies (NLS1s Osterbrock & Pogge, 1985), and may be explained by low mass black holes in an early growing stage (Mathur, 2000). Whatever the origin of NLS1s, their existence is evidence that the observational differences between Seyfert 1 and Seyfert 2 galaxies cannot be parametrized by a single parameter such as inclination.

The broad emission line are very broad, with widths of several 1000s km/s, and originate in gas with temperatures of 10^4 K (Anderson, 1970). These velocities are too large to be associated with purely thermal line broadening[3]. Instead the interpretation is that the broad line emitting gas is orbiting in the gravitational field of the black hole. If the orbits are assumed to be virialized, such that the kinetic energy of the BLR gas can be uniquely related

[3]If the line widths were due to purely thermal broadening, it would correspond to temperatures upwards 10^9 K (Peterson, 1997), orders of magnitudes larger than the ionization temperature of hydrogen.

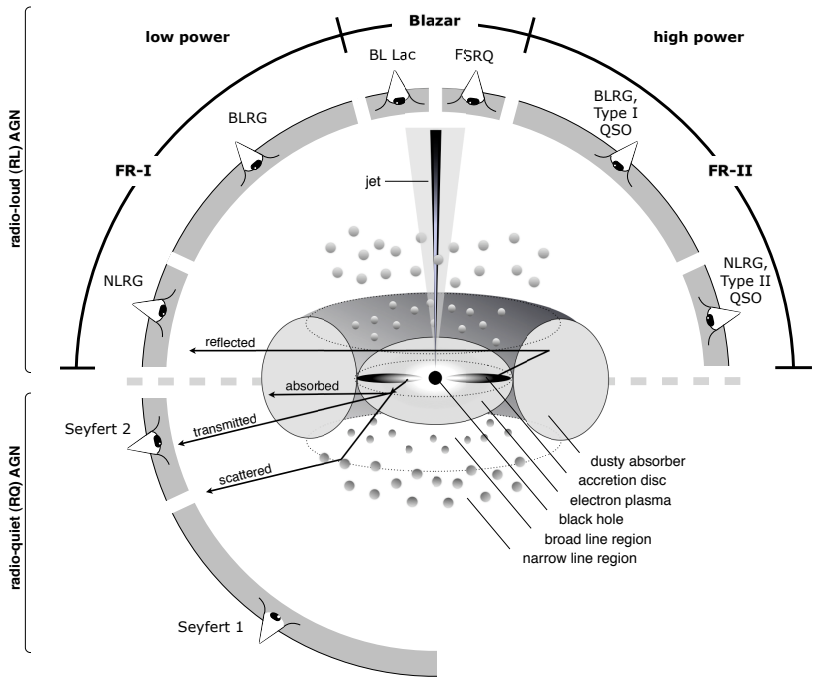

Fig. 1.5 Unification model of active galactic nuclei (see also Elvis (2000)). Reproduced from Beckmann & Shrader (2012).

to the black hole gravitational field, the black hole mass can be estimated, if we can somehow determine the radius of the BLR orbits.

Due to the long distance to the nearest galaxy hosting an active nucleus, and the small scale of the central emission region (1-100 light days), the BLR is not spatially resolved in experiments. In order to test models for AGN unification, and to better understand AGN fueling and feedback mechanisms, relevant for galaxy and black hole evolution, we need a way to observe the inner regions of AGN, close to the central energy source. The small size of the central engine, which makes the inner regions of AGN spatially unresolved, also results in short time-scale $\mathcal{O}(\text{days})$ stochastic variability (MacLeod et al., 2010). The variability resolves AGN in the time domain, and can be used to probe the inner structure at the μ-arcsecond scale, by the technique of reverberation mapping (Bahcall et al., 1972; Blandford & McKee, 1982; Peterson, 1993).

1.3.2 Reverberation mapping

The turbulent accretion flow in AGN creates strong stochastic variability patterns in the AGN continuum emission light curves. The continuum variability changes the ionization state of the broad emission line gas, which responds to the continuum variability in an

approximatively linear fashion[4]. The response of the broad emission lines to changes in continuum luminosity is not instantaneous, but is a combination of reprocessing time and geometrical light travel time in the AGN (Peterson, 1993, 1997).

The reprocessing time in the BLR is controlled by the hydrogen recombination time (Ferland et al., 1992; Korista & Goad, 2004) and is on the order of seconds (Peterson, 1997). Significant geometrical changes in the broad line region propagate on the dynamical time scale of the BLR, the time it takes for a broad emission gas cloud to cross the BLR. The dynamical time scale is controlled by the cloud velocities, which is given by the width of the broad emission lines (a few 1000 km/s), a factor 100 below the speed of light. Assuming that photons can travel freely in the BLR, we arrive at the conclusion that the primary time scale in BLR continuum reprocessing, is the light travel time between the ionizing continuum and the BLR. If we can measure the light travel time, we can map the BLR by determining the time delay between continuum and broad line variability patterns, a technique known as reverberation mapping (Blandford & McKee, 1982; Peterson, 1993).

In reverberation mapping, the broad line emission is related to the ionizing continuum emission by a simple transfer equation,

$$F_l(t,\lambda) = \int_{-\infty}^{\infty} \Psi(\tau,\lambda) F_c(t-\tau)\mathrm{d}\tau, \tag{1.2}$$

where F_l and F_c are the emission line and continuum light curves respectively, and Ψ is the two-dimensional transfer function, that encodes the response of the broad emission to changes in the continuum. The first moment of the response function provides a measure of the characteristic size of the BLR at the given wavelength λ, while the full transfer function can yield additional kinematical information and emissivity distributions (Perez et al., 1992; Goad et al., 1993).

Because of the number of dimensions involved, determining the full geometrical structure of the BLR is not possible without additional assumptions about its structure. For this reason, it is important to combine photoionization models with reverberation mapping results, to constrain the three-dimensional physical structure of the BLR (Goad et al., 1993; Horne et al., 2003). Besides constraining the structure of the BLR, reverberation mapping can be used to estimate the central black hole mass.

[4]The linear approximation is good to first order, but the actual response is almost certainly non-linear (Korista & Goad, 2004; Goad & Korista, 2014)

Black hole masses and the f-factor

Reverberation mapping can be used to measure the emissivity weighted radius of the BLR for a given emission line. If it is assumed that the BLR gas is in bound orbits around the black hole, the black hole mass can be calculated by combining the BLR radius with the broad emission line width,

$$M_{\rm BH} = \frac{f(\Delta V^2 R_{\rm BLR})}{G}, \tag{1.3}$$

where ΔV is the width, in units of velocity, of the varying part of the emission lines, $R_{\rm BLR}$ is the radius of the BLR, G is the gravitational constant and f is a dimensionless parametrization of our ignorance about the structure, ionization physics and kinematics of the BLR (Wandel et al., 1999).

A geometric contribution to the f factor could arise if the BLR clouds have an anisotropic velocity distribution, which would make the measured line of sight velocity of the BLR a function of inclination i,

$$f \propto \frac{1}{\sin^2 i}. \tag{1.4}$$

Unified models of AGN suggest that some differences between Seyfert 1 and 2 galaxies can be explained by inclination affects, so it is reasonable to expect some contribution from inclination to the f factor. In practice, the role of inclination is small compared to other systematic effects in black hole mass estimates (e.g. Collin et al., 2006). Diversity in AGN properties cannot be fully accounted for by geometrical effects. Black hole mass and accretion rate also play important roles. The accretion rate is difficult to measure directly (e.g. Merloni & Heinz, 2008), but is instead encapsulated in the bolometric AGN luminosity relative to the theoretical maximum Eddington luminosity, called the Eddington ratio (Eddington, 1926).

The diversity in AGN properties translates into systematic uncertainties on AGN black hole mass estimates, but systematics enter not only through the f factor, but also through the measure of the broad emission line width ΔV. The black hole mass equation (Eq. 1.3) assumes that the origin of the line width is virialized motion of the BLR clouds. In reality broad emission line profiles in AGN are much more complicated, and are affected by bulk flows and AGN accretion rates (Collin et al., 2006; Denney, 2012). The presence of bulk in or outflow in the BLR is particularly problematic for the assumption of virialized motion (Marconi et al., 2008).

For reverberation mapping to provide accurate masses it is important to understand any uncertainties and systematic effects, such as the f factor, that can bias reverberation mapping black hole mass measurements. An indirect way to constrain the average $\langle f \rangle$ is by calibrating

to AGN scaling relationships that connect the black hole mass to properties of the host galaxy (e.g. Onken et al., 2004).

1.3.3 AGN scaling relations

The M_{BH} - σ_* relation

Scaling relations between supermassive black holes and their host galaxies have been studied extensively in inactive galaxies, where the black hole mass can be inferred from kinematics of gas or stars in the neighborhood of the black hole (Barth et al., 2001; Sarzi et al., 2001; Davis et al., 2013). These measurements reveal a remarkably tight relationship between the black hole mass (M_{BH}) and the bulge stellar velocity dispersion (σ_*) of the host galaxy, called the $M_{\mathrm{BH}} - \sigma_*$ relation (Kormendy & Richstone, 1995; Magorrian et al., 1998; Ferrarese & Merritt, 2000; Gebhardt et al., 2000). Note that even if the black hole is massive, its gravitational sphere of influence is dwarfed by the size of the bulge. For this reason it is thought that the $M_{\mathrm{BH}} - \sigma_*$ relation has to be regulated by some type of co-evolution of the black hole and the host galaxy, possibly due to major mergers and black hole feedback during AGN activity (Silk & Rees, 1998; Haehnelt & Kauffmann, 2000; Umemura, 2001; Fabian, 2012; Kormendy & Ho, 2013).

Assuming that the $M_{\mathrm{BH}} - \sigma_*$ relation holds not only for inactive galaxies, but for active galaxies as well, the average $\langle f \rangle$ from reverberation mapping measurements can be calibrated by forcing alignment between the $M_{\mathrm{BH}} - \sigma_*$ relationship for active and inactive galaxies. This yields a value of $\langle f \rangle = 5.5 \pm 1.8$ (Onken et al., 2004).

The R_{BLR} - L_{AGN} relation

The observation that the broad emission follows the continuum closely, suggests that it is driven by photoionization by the continuum source. The strength of the broad recombination line emission is proportional to the fraction of ionized atoms in the BLR, and is controlled by the ionization parameter U. Provided that sufficient neutral gas is available, the value of the ionization parameter is controlled by the number of available ionizing photons. In the case of hydrogen, the number of ionizing photons available per second is an integral over the continuum luminosity above the Lyman limit,

$$Q_{\mathrm{H}} = \int_{\nu_{\mathrm{Lyman}}}^{\infty} \frac{L_\nu}{h\nu} \mathrm{d}\nu \tag{1.5}$$

where L_ν is the specific luminosity of the incoming photon field, ν is the photon frequency and h is the Planck constant. If the ionizing luminosity is emitted isotropically centered on the black hole, this leads to an ionization parameter that decreases with radius as $1/R^2$,

$$U = \frac{Q_{\mathrm{H}}}{4\pi R^2 c n_{\mathrm{H}}}. \tag{1.6}$$

For the ionized hydrogen gas to emit efficiently, to first order, the rate of ionization has to match the rate of recombination. Assuming that the hydrogen density in the BLR is not a strongly varying function of radius, the distance from the central source to the BLR will be the deciding factor in regulating the ionization parameter. If the shape of the ionizing continuum is not a function of luminosity, the broad line region radius R_{BLR} is related to the central source bolometric luminosity as

$$R_{\mathrm{BLR}} \propto L^{1/2}. \tag{1.7}$$

As compelling as these arguments may seem, the actual picture is naturally more complicated (see Baldwin et al., 1995; Goad & Korista, 2014, 2015, and references therein). Intriguingly, the simple relation stated in Eq. 1.7 is found to fit remarkable well with observations of AGN across several orders of magnitude (see Fig. 1.6). The observed relation between the BLR radius R_{BLR} and the central luminosity L is

$$\log(R_{\mathrm{BLR}}/1\,\mathrm{lt\text{-}day}) = K + \alpha \log(\lambda L_\lambda / 10^{44}\,\mathrm{erg\,s^{-1}}). \tag{1.8}$$

The current best fit values are determined by Bentz et al. (2013), and are found to be $K = 1.527 \pm 0.031$ and $\alpha = 0.533^{+0.035}_{-0.033}$, very close to the theoretical value of $\alpha = 0.5$ from Eq. 1.7. The fact that this relation seems to hold across orders of magnitude in luminosity provides evidence that AGN are, at least on average, self-similar objects, that have reached some sort of steady state in their evolution (Kaspi et al., 2000, 2005; Bentz et al., 2009a, 2013).

The radius luminosity relation has interesting applications. The intrinsic luminosity of high redshift AGN can be determined from the redshift, assuming a cosmological model, and then be converted to an estimate of the BLR size using the R-L relation. The BLR size together with the emission line width, determined from single epoch spectroscopy, can then be used to calculate the supermassive black hole masses at high redshift using Eq. 1.3 (McLure & Jarvis, 2002; Netzer, 2003; Vestergaard, 2004). This reveals black hole masses in the early universe that are orders of magnitudes larger than what can be accounted for by Eddington limited black hole growth, providing a direct link between supermassive black holes and early structure formation. These findings prompt suggestions that black holes in the

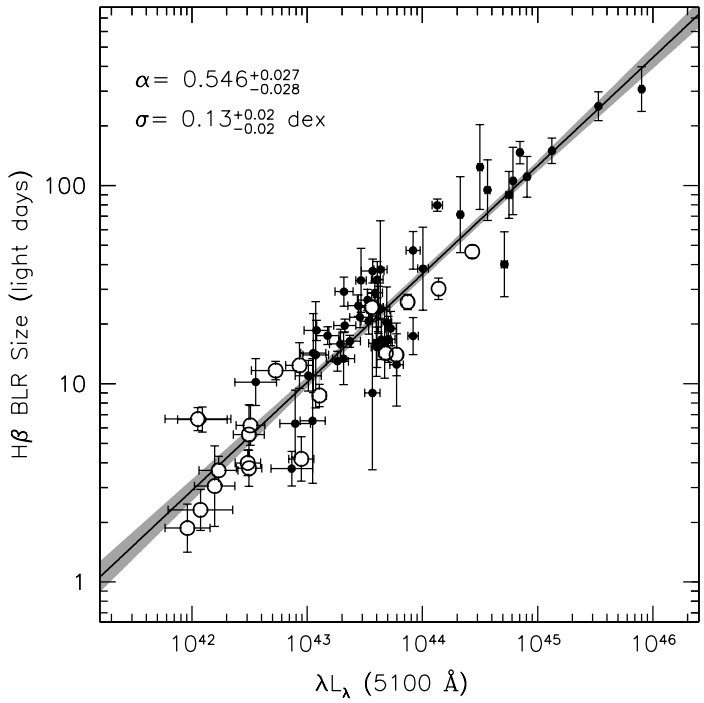

Fig. 1.6 Radius-luminosity relation for active galactic nuclei. Open circles indicate new data added by Bentz et al. (2013), while solid black circles is data from the literature. Reproduced from Bentz et al. (2013).

early universe may be seeded by direct collapse of gas in early dark matter haloes (Volonteri et al., 2003; Choi et al., 2013; Latif et al., 2013), or otherwise grown by super-Eddington accretion mechanisms in protogalactic haloes (e.g. Begelman et al., 2006).

Another proposed application of the radius luminosity relation is to measure BLR radii using reverberation mapping for a large number of AGN, at a range of redshifts, and then use the radius luminosity relation to estimate intrinsic luminosities. This provides an independent cosmological distance measure based only on AGN (Watson et al., 2011; King et al., 2014).

Despite successful applications of the radius luminosity relation, significant work is required to understand its intrinsic scatter, and the difference between radius luminosity relations for different broad emission lines. There are many approaches in tackling the scatter in AGN scaling relations, but most depend to some degree on our understanding of the structure and emission mechanism of AGN.

1.3.4 Revealing the structure of AGN

Besides being an excellent tool for measuring supermassive black hole masses, reverberation mapping can provide a unique picture of the intrinsic structure of AGN (e.g. Wanders et al., 1995). Advanced methods for reverberation mapping provide not only an emissivity weighted radius of the BLR (as described above), but a time resolved response function for a given emission line (e.g. Ulrich & Horne, 1996). The shape of this two dimensional response, or velocity–delay map ($\Psi(\tau, \lambda)$ in Eq. 1.2), is a combination of kinematics, geometry and ionization physics in the AGN. So while the response function does not provide a direct picture of the physical structure of the AGN, it does provide a means to select between various physical and geometrical models for the BLR. Ultimately, the hope is that we can use velocity-resolved reverberation mapping, combined with geometrical and photoionization models, to learn about the intrinsic structure of AGN. Using a complete physical model of the BLR it would be possible to measure black hole masses directly, determining the origin and value of f (from Eq. 1.3) in individual objects, and thereby better understand the intrinsic scatter in black hole mass scaling relations.

An important step in this direction is the development of reverberation mapping methods that provide response functions as a function of wavelength across an emission line. These two-dimensional response functions are called velocity–delay maps, as they provide response functions for each resolved velocity component across an emission line in a spectrum (Welsh & Horne, 1991). The most immediate application of velocity-resolved reverberation mapping is to discover possible signatures of bulk gas flows in AGN. Probing bulk flows in the BLR allows testing the virialization assumption implicit in reverberation mapping black hole measurements. Furthermore, two-dimensional response functions extract additional

information from reverberation mapping data, which can help break geometrical degeneracies inherent to integrated response functions (Perez et al., 1992; Horne et al., 2003). Finally, results from velocity resolved reverberation mapping could hint at ways the AGN are being fueled, as well as how they deposit energy into the surrounding medium of the host galaxy, to produce the observed AGN-host galaxy scaling relations.

In Chapter 3 I present a new implementation of a method for reverberation mapping based on regularized linear inversion (RLI; Vio et al., 1994; Krolik & Done, 1995), which includes modeling of the AGN light curves. This method enables analytical calculation of velocity–delay maps, and error estimation by modeling the light curves as Gaussian processes. The method has the advantage that it allows very fast and accurate calculations of velocity–delay maps, as well as integrated response functions, for reverberation mapping data. It does this while allowing for multimodal response functions and negative response values.

I apply the method to reverberation data for five nearby AGN, observed by the LICK AGN Monitoring Project (Bentz et al., 2008), and present new velocity–delay maps for all objects. Several of these maps show interesting features such as multi modal response and signatures of bulk gas flows in the BLR, and can be compared to predictions from theoretical models to help us better understand the physical structure of AGN.

1.3.5 Pushing the limits of AGN scaling relations

The exploration of AGN scaling relations is still in its infancy, and the full power of these relations has yet to be revealed. The possibility of using AGN scaling relations to relate the BLR radius to the intrinsic AGN luminosity, begs the consideration that AGN may be standardizable candles. That would make it possible to extend the cosmological distance ladder with large samples of AGN at redshift ranges previously inaccessible, constraining cosmological models in these new regimes (Watson et al., 2011), and investigating current tensions between measurements of H_0 (Riess et al., 2016). This only works if we can bring the uncertainty in the $R_{\rm BLR}$ measurements down to levels comparable to contemporary distance probes, such as CMB, supernovae and baryonic acoustic oscillations, which are currently at 1-3% (Planck Collaboration et al., 2016; Riess et al., 2016; Alam et al., 2016). Just like in the case of the f factor, this means that we need a better understanding of the structure and variation of the AGN BLRs, as well as systematic uncertainties associated with its exploration.

Besides controlling AGN intrinsic systematics, extending reverberation mapping surveys to larger samples and higher redshifts, is a challenging task in itself, but is required in order to make AGN useful as cosmological probes (King et al., 2014). Typical reverberation mapping

campaigns of nearby AGN require of the order 50 high quality spectra for each object, distributed approximately evenly over a full observing season (Bentz, 2015). This makes conventional reverberation mapping campaigns rather expensive in terms of observation time, and the cadence requirements pose additional challenges in scheduling observations. High signal-to-noise spectroscopy is required to do accurate spectral decomposition, to isolate individual broad emission lines, and for providing velocity information to produce velocity–delay maps. Finally, time dilation effects, and the fact that we observe more luminous AGN at higher redshifts, result in significantly longer time delays, that make conventional reverberation mapping surveys prohibitively expensive at high redshift. A way to overcome some of these issues is to use multi-object spectrographs, but this introduces other challenges such as doing atmospheric dispersion correction for multiple objects in the same field, and accurate flux calibrations.

Photometric reverbration mapping

The issues described above prompt us to look for alternative reverberation mapping methods for studying AGN scaling relations at progressively higher redshifts. A promising method for measuring emissivity weighted time delays at a fraction of the cost of conventional campaigns, is photometric reverberation mapping (Haas et al., 2011).

Photometric reverberation mapping was applied in the 70s by Cherepashchuk & Lyutyi (1973) to measure Hα time delays in NGC 3516 and NGC 4151. The method relies on separating continuum and broad emission line flux in separate photometric bands, and modeling the integrated light curves in each band to derive an estimate for the average time delay for broad line band. This method has been successful in measuring accurate time delays for Hα and Hβ in a number of objects (Haas et al., 2011; Pozo Nuñez et al., 2012, 2013, 2015).

Photometric reverberation mapping has its own intrinsic difficulties, such as dealing with continuum and emission lines blending into the same bands. Furthermore, significantly broad, asymmetric, double peaked, or varying emission line profiles observed in some AGN (e.g. Strateva et al., 2003) may bias the measured line flux, if not adjusted for. For measuring a time delay, a constant absolute flux error is not necessarily an issue, because we can construct light curves using relative photometry. But if the line profile or continuum contribution in the line band changes significantly during the observing campaign, systematic uncertainties will be introduced in the emission line light curves. These issues makes it difficult to disentangle the continuum and emission line components in individual epochs, and it is imperative that reverberation mapping methods relying on photometry study and deal with these issues effectively.

A direct way to evaluate the performance of photometric reverberation mapping would be to schedule observing campaigns where spectroscopic and photometric measurements are conducted simultaneously. This would allow a direct comparison between not just the ratio of emission components in individual photometric bands, but also a direct comparison between spectroscopic and photometric reverberation mapping results.

Another more indirect strategy to evaluate the performance of photometric reverberation mapping is to observe a large number of AGN, and derive scaling relations using only photometric measurements. This would allow comparison of scaling parameters from spectroscopic campaigns, and would reveal any overall systematic differences between the two methods. This may seem observationally expensive, given that the performance of photometric reverberation mapping on large samples of objects is untested. But because photometric observations can be conducted on smaller telescopes, with potentially many objects observed in a single exposure, it may in fact be cheaper than scheduling simultaneous spectroscopic observations for a large sample of objects. This does not mean that direct comparisons are unnecessary, but simply that it is not the sole strategy for assessing the feasibility of photometric reverberation mapping.

Finally, there is the challenge of selecting candidate AGN and constructing suitable narrow band filters that cover emission lines at the given redshift. Although these are not fundamental challenges, overcoming them may turn out to be difficult in practice. Monitoring several AGN in the same field would require some sort of filter mosaics for each field of interest, allowing for photometry to be obtained for multiple AGN at any one time. While not impossible to construct, this certainly poses challenges for initiating large scale photometric reverberation mapping campaigns.

In Chapter 4 I describe the method of photometric reverberation mapping, and present new results from photometric reverberation mapping of three nearby AGN using data from the *STELLA* Robotic Observatory on Tenerife. These results show that photometric reverberation mapping can provide competitive BLR time delays, by use of short exposures on small telescopes, significantly reducing the observing time required to extend scaling relations to more objects, and in time, to higher redshifts. This, and other photometric studies, lay the groundwork for developing future large scale photometric reverberation mapping campaigns.

Chapter 2

Measuring kinematics of galaxies in clusters

This chapter contains the paper:

"Spatial anisotropy of galaxy kinematics in SDSS galaxy clusters"
Skielboe, A., Wojtak, R., Pedersen, K., et al. 2012, ApJ, 758, L16

2.1 Abstract

Measurements of galaxy cluster kinematics are important in understanding the dynamical state and evolution of clusters of galaxies, as well as constraining cosmological models. While it is well established that clusters exhibit non-spherical geometries, evident in the distribution of galaxies on the sky, azimuthal variations of galaxy kinematics within clusters have yet to be observed. Here we measure the azimuthal dependence of the line-of-sight velocity dispersion profile in a stacked sample of 1743 galaxy clusters from the Sloan Digital Sky Survey (SDSS). The clusters are drawn from the SDSS DR8 redMaPPer catalog. We find that the line-of-sight velocity dispersion of galaxies lying along the major axis of the central galaxy is larger than those that lie along the minor axis. This is the first observational detection of anisotropic kinematics of galaxies in clusters. We show that the result is consistent with predictions from numerical simulations. Furthermore we find that the degree of projected anisotropy is strongly dependent on the line-of-sight orientation of the galaxy cluster, opening new possibilities for assessing systematics in optical cluster finding.

2.2 Introduction

Clusters of galaxies constitute the largest, gravitationally collapsed, structures in the universe. They offer a unique opportunity to study the formation and evolution of structure on cosmological scales. Additionally, the mass distribution of galaxy clusters can be observationally probed both dynamically and via weak lensing, making galaxy clusters ideal laboratories for studying dark matter and modifications to general relativity (e.g. Rapetti et al. (2010, 2013)).

Observations and simulations clearly show that clusters exhibit triaxial rather than spherical shapes (Binggeli, 1982; Bailin & Steinmetz, 2005; Gottlöber & Yepes, 2007). Hoekstra et al. (2004) made the first detection of the flattening of galactic dark matter halos using weak lensing and van Uitert et al. (2012) measured the azimuthal variation of the weak gravitational lensing signal around galaxies, constraining galactic dark matter halo ellipticity. Non-zero ellipticity of dark matter halos has also been confirmed in strong lensing measurements by studying the angular distribution of giant arcs around groups and clusters of galaxies (Dalal et al., 2004; More et al., 2012).

The velocity fields of galaxies in clusters are known to feature non-trivial radial dependencies, but azimuthal variations are often overlooked. If the shape of the underlying dark matter halo is indeed multiaxial, it is natural to think that it will be reflected in an anisotropic velocity field. Indeed this has been confirmed and studied using numerical simulations (Tormen, 1997; Kasun & Evrard, 2005; White et al., 2010; Saro et al., 2013). Because cluster mass estimators often assume spherically symmetric velocity fields, characterizing the degree of anisotropy in galaxy clusters is crucial in understanding its impact on cluster mass estimates. It may also provide clues to the ongoing formation of galaxy clusters.

The effect of an anisotropic velocity field should manifest itself in an azimuthal variation of the projected velocity dispersion of member galaxies. To our knowledge no attempts have been made to measure the azimuthal variation of galaxy velocity dispersions in a large sample of galaxy clusters.

The aim of this Letter is to test for azimuthal dependence of the projected velocity dispersion of cluster galaxies in a stacked sample of galaxy clusters. We use the Sloan Digital Sky Survey (SDSS) DR8 (Aihara et al., 2011) redMaPPer cluster catalog (described below) to search for an anisotropic velocity field by measuring the velocity dispersion of cluster galaxies along the major axis of the central galaxy (CG), and galaxies along the corresponding orthogonal axis. The results are compared with expectations from numerical simulations. We adopt a flat ΛCDM cosmology with $\Omega_m = 0.3$ and $H_0 = 70$ km s^{-1} Mpc^{-1}.

2.3 Methods

The expected degree of the relative difference in dispersion is of the order of a few percent (see Section 2.4.1). The strategy for detecting a signal of this magnitude is to stack a large number of galaxy clusters.

2.3.1 The redMaPPer Cluster Catalog

The red sequence is a tight relationship between galaxy color and magnitude of galaxy cluster members (Visvanathan & Sandage, 1977). The low scatter in the relation allows it to be applied in photometric galaxy surveys to locate clusters by requiring that their members follow the red sequence. Given a candidate galaxy cluster, cluster members can be added, and the cluster redshift estimated, by iteratively fitting galaxies to the red sequence for the given cluster (Gladders & Yee, 2000).

Our study utilizes the SDSS DR8 red-sequence matched-filter probabilistic percolation ("redMaPPer") cluster catalog (Rykoff et al., 2012), based on an optimized richness (i.e. the number of galaxies in the cluster) estimator λ (for details on the richness estimator see Rozo et al., 2009, 2010; Rykoff et al., 2012). redMaPPer is a photometric cluster catalog that identifies galaxy clusters as overdensities of red-sequence galaxies. The algorithm is divided into two stages: a calibration stage, where the red-sequence model is determined directly from the data, and a cluster-finding stage. These two stages are iterated several times before a final cluster-finding run is made.

In the calibration phase, redMaPPer empirically calibrates the color distribution (mean and scatter) of red-sequence galaxies as a function of redshift and magnitude. The calibration itself is also an iterative procedure. First, we use red galaxies from the SDSS luminous red galaxy (Eisenstein et al., 2001) and "main" (Strauss et al., 2002) spectroscopic galaxy samples (over 50% of the sky) as training galaxies. These galaxies are used as "seeds" to look for significant overdensities of nearby galaxies with the same color as the seed galaxy. The resulting cluster list is used to fit a full red-sequence model including zero point, tilt, and scatter. Moreover, the algorithm utilizes all colors ($u-g$, $g-r$, $r-i$, and $i-z$) simultaneously, so the "scatter" is characterized not by a single number but by a covariance matrix. The red sequence model is calibrated down to a luminosity threshold of $0.2\,L_*$ at the cluster redshift (the optimal depth for cluster richness estimation Rykoff et al., 2012), thereby leveraging the bright spectroscopic galaxy sample to obtain a model of the red sequence that extends to dim magnitudes.

With our model of the red sequence at hand, we proceed to run the cluster-finding algorithm as described below. The resulting cluster catalog is then used to re-calibrate the

model of the red-sequence as above, and the procedure is iterated until convergence in the red sequence model parameters is achieved. At that point, we perform one final cluster-finding run to arrive at the final redMaPPer catalog.

Given a red-sequence model, the cluster finding proceeds as follows. First, we consider all photometric galaxies as candidate cluster centers. We use our red-sequence model to calculate a photometric redshift for each galaxy, and evaluate the goodness of fit of our red galaxy template. Galaxies that are not a reasonable fit to the red-sequence model at any redshift are immediately discarded. For the remaining galaxies, we use this initial redshift guess and the red-sequence model to evaluate the richness (λ) and cluster likelihood, proportional to the probability that this is in fact a cluster, using a multi-color generalization of the method in Rykoff et al. (2012). When a significant number of red galaxies are detected, we re-estimate the cluster redshift by performing a simultaneous fit of all the high-probability cluster members to the red-sequence model. This procedure is iterated until convergence is achieved between member selection and cluster photometric redshift. The resulting list of candidate cluster centers is then rank-ordered according to likelihood, and membership probabilities are used to mask out member galaxies in the percolation step.

The final aspect of our algorithm is the selection of cluster CGs. Specifically, if the luminosity distribution of CGs as a function of richness is known, then one can evaluate the relative probability that any given galaxy with a color consistent with the red sequence is consistent with the CG distribution, with the satellite luminosity function; or with the foreground magnitude distribution. We also take into account a local density estimator by evaluating the offset of the proposed CG with respect to the local peak density, as CGs tend to reside in the densest parts of the cluster. In general, however, we find that the luminosity filter dominates in most cases. To define the filter functions, as with the red-sequence calibration we follow an iterative procedure: on our first iteration, centers are defined as the brightest high membership probability galaxy. These assigned centers are used to characterize a “first guess" for the luminosity distribution and local density of CGs. We then rerun our central selection algorithm iteratively until convergence. In the end, every galaxy in the cluster can be assigned a probability of being a CG, though typically no more than two galaxies have a significant probability of being the CG of the cluster.

2.3.2 Cluster and Galaxy Selection

To create the galaxy stack, we group cluster galaxies based on their azimuthal positions and relative line of sight velocities, with respect to the cluster central galaxies, including member galaxies for a large number of galaxy clusters, to study their combined line-of-sight velocity distributions as a function of azimuthal position.

To reduce an effect of stacking clusters of different sizes we choose richness cut in the catalog of $20 < \lambda < 50$, corresponding to the mass range $1.4 < M_{200c}/10^{14} M_{\odot} < 3.6$ (Rykoff et al., 2012). When stacking clusters there is also an issue of miscentering of the central galaxy, which will smear the distribution stacked galaxies on the sky. We alleviate issues of miscentering by using the centering probability $P_{\rm CG}$, reported in the redMaPPer catalog, to select clusters with $P_{\rm CG} > 0.95$, implying we expect $> 95\%$ of our galaxy clusters are properly centered. We impose no cut on redshift.

Cluster candidate members are selected from SDSS DR8. To get accurate relative velocities we use only galaxies with spectroscopic redshifts. For each CG we do an initial broad selection of member galaxies by choosing all galaxies that satisfy $|\Delta v| < v_{\rm max} = 4000$ km s^{-1} and $d < 6$ Mpc, where Δv is the difference in velocity between the galaxy and the CG and d is their projected separation. These cuts are intentionally generous, since interlopers are included in our velocity distribution model. If a galaxy is a candidate member for several clusters, we assign the galaxy only to the nearest cluster, based on the projected distance to the CG. Finally, we discard clusters with fewer than four spectroscopic candidates. To ensure that our results are insensitive to the precise selection criteria adopted, we repeat the analysis varying the richness, centering probability and velocity cut selection criteria by $10-20\,\%$. We recover consistent results in all cases, indicating that the exact values of the selection criteria are not contributing strongly to the final uncertainties on our results.

This leaves a total of 1743 clusters containing 49,524 candidate member galaxies (of which 13,565 have $d \leq 2$ Mpc) that were used in the final analysis.

2.3.3 Galaxy Positions Angles

CG major axis position angles are taken from the *R*-band photometric object position angles (E of N) from a de Vaucouleurs model fit provided in the SDSS DR8. To avoid ambiguity in determining CG position angles, we require that the projected axis ratio of the ellipticity for each CG is less than 0.9. Member galaxy coordinates are used to determine the azimuthal angle $\Delta\phi$ between the galaxy and the projected CG major axis. Galaxies are put in two spatial sections according to their position angle relative to the major axis of the CG (see Figure 2.1).

2.3.4 Line-of-sight Galaxy-velocity Model

Member galaxy velocities are calculated relative to the CG ($v_{\rm rel} = v_{\rm CG} - v_{\rm gal}$). This only makes sense if the CG is at rest with respect to the halo, otherwise we might observe a systematic offset of the mean of the velocity distribution of member galaxies. If the offset

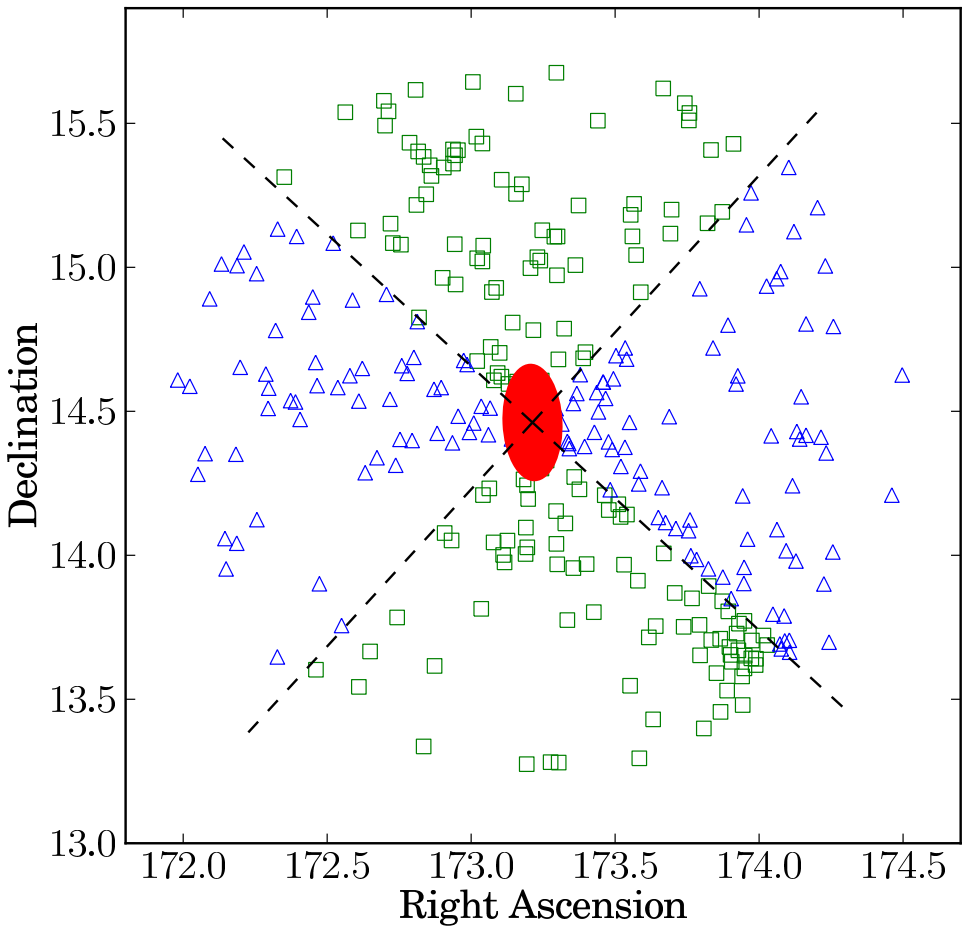

Fig. 2.1 Sky plot of a galaxy cluster with member galaxy candidates. The CG is represented by an exaggerated red ellipse. The azimuthal sections used in the analysis are indicated by dashed lines. Member candidates are marked according to their associated section, with green squares indicating galaxies closer to the CG major axis and blue triangles indicating galaxies closer to the minor axis. This plot contains interlopers as well as cluster members.

is random the mean will be zero, but the dispersion will become systematically larger. We find that for all stacked velocity distributions the mean is consistent with zero, within effects from gravitational redshift (see, e.g., Wojtak et al. (2011)).

The velocity distribution is modeled as a Gaussian probability distribution with mean μ and dispersion σ. Interlopers are assumed drawn from a flux-limited uniform background, which makes the background a linear decreasing function of recession velocity, given by a probability distribution with intercept n, and slope $s(n) = (1/(2v_{\rm max}) - n)/v_{\rm max}$ fixed by the probability distribution normalization condition. To ensure overall normalization, a parameter p is introduced, which is the probability for a galaxy to be a member of a cluster. The probability for a particular relative velocity $v_{\rm rel}$ in this model is given by

$$P(v_{\rm rel}|p,\sigma,\mu,n) = p\frac{1}{\sqrt{2\pi}\sigma}\exp\left[-\frac{1}{2}(v_{\rm rel}-\mu)^2/\sigma^2\right] + (1-p)(s(v_{\rm rel}+v_{\rm max})+n). \quad (2.1)$$

Each velocity derived from SDSS includes a measurement error of the order of a few tens of km s^{-1}, which has the effect of slightly increasing the measured dispersion of the stacked sample of velocities. This error is small and should not affect the results, especially when studying azimuthal variation in dispersion. We estimate the likelihood for a given velocity dispersion σ_v by a Bayesian likelihood analysis, multiplying probabilities over all velocities in the data sample,

$$\mathscr{L}(p,\sigma_v,\mu,n) = \prod_i P(v_i|p,\sigma_v,\mu,n). \quad (2.2)$$

To generate the posterior distribution for the parameter σ_v we sample the likelihood over the prior parameter space, while marginalizing over all other parameters, using the method of nested sampling (Feroz & Hobson, 2008). We use the publicly available software `MultiNest` (Feroz et al., 2009). An example of a model fit to data for a particular radial bin is presented in Figure 2.2.

2.4 Results

Figure 2.3 shows galaxy velocity dispersion as a function of radius for two populations of cluster member galaxies; those that lie closer to the projected CG major axis and those that lie closer to the projected CG minor axis. We find a decreasing relationship between velocity dispersion and radius, consistent with the result expected for a Navarro-Frenk-White (NFW) profile (Navarro et al., 1997), with concentration parameter $c = 5.5$ (Klypin et al., 2011) and

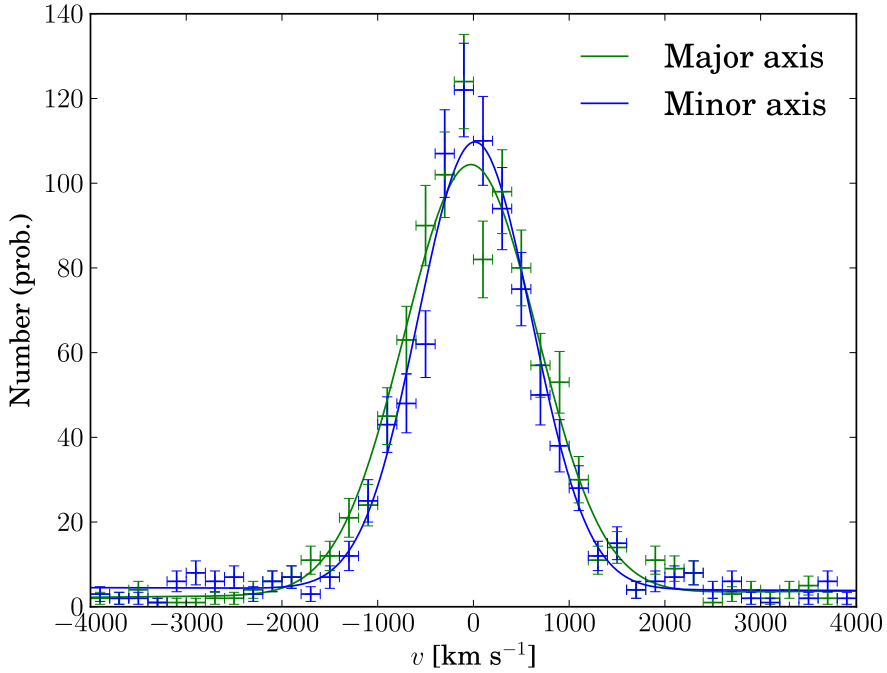

Fig. 2.2 Example velocity distribution of member galaxies along with the model from Eq. (2.1) with highest-posterior values obtained using MultiNest (solid lines). The green crosses/line shows velocities along the major axis, and blue crosses/lines shows velocities along the minor axis.

typical anisotropy of galaxy orbits in clusters (Wojtak & Łokas, 2010), convolved with the mass function of the redMaPPer clusters in the given richness range.

In Figure 2.4 we plot the measured difference in line of sight velocity dispersion as a function of radius, divided by the mean dispersion at the given radius. The weighted difference is calculated as $\Delta\sigma_v/\langle\sigma_v\rangle = 2(\sigma_v^{\rm maj} - \sigma_v^{\rm min})/(\sigma_v^{\rm maj} + \sigma_v^{\rm min})$. The dashed line (blue band) shows maximum likelihood ($\pm 1\sigma$) for a constant difference in weighted dispersion between the two azimuthal sections. The posterior for the constant weighted difference is $\Delta\sigma_v/\langle\sigma_v\rangle = 0.06 \pm 0.02$, corresponding to an absolute difference of $\Delta\sigma_v = 38$ km s$^{-1} \pm 13$ km s^{-1}. This indicates that galaxies along the projected major axes of the CGs exhibit preferentially higher velocity dispersions compared to galaxies lying along the projected minor axes.

We test whether the observed difference could be systematic in nature by repeating our experiment, but randomly orienting the halos when stacking, and then splitting the galaxy memberships along a random axis. As expected we do not detect any difference in the velocity dispersion of the two galaxy populations in this case. We also verify that our conclusions are valid if we remove the radial bin with the strongest offset ($R = 0.6$ Mpc), albeit at reduced significance of 2σ. Finally, we find that varying the cuts used to select candidate cluster members does not significantly alter our results (see Section 2.3.2).

2.4.1 Numerical Simulations

To compare our measurement with theoretical predictions, we analyzed velocity dispersion profiles of subhalos in cluster-size halos from the Bolshoi simulation[1] of a standard ΛCDM cosmology (Klypin et al., 2011). We used ~ 500 dark matter halos with masses $M_{200c} > 0.4 \times 10^{14} M_\odot$ and subhalos with at least 30 particles corresponding to a minimum mass of $M_{200c} > 2 \times 10^9 M_\odot$. Subhalos were identified using Bound Density Maximum algorithm (Klypin & Holtzman, 1997). For every halo we calculated projected velocity dispersion profiles as measured by a distant observer. The profiles were determined inside two equal sections along the projected major axes of the halos and along the perpendicular direction, likewise in the analysis of SDSS data. The major axes of dark matter halos were determined by diagonalization of the tensor of inertia computed using dark matter particles inside the virial spheres. We considered three fixed orientations of the line of sight with respect to the major axes of the halos, with angles 5°, 20° and 90°, and a fourth case corresponding to a fully random angle distribution of the light cones.

[1]The Bolshoi simulation is publicly available via the MultiDark database (http://www.multidark.org; Riebe et al. 2011).

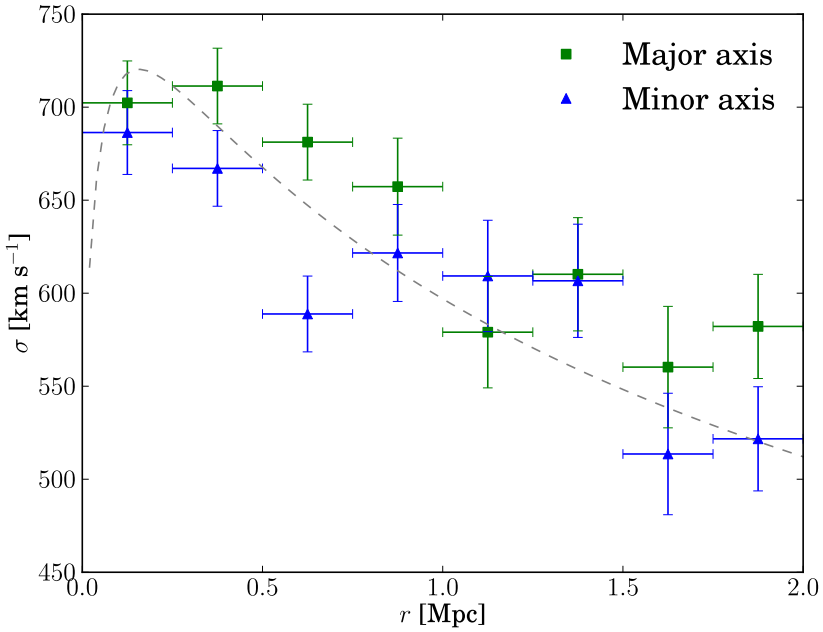

Fig. 2.3 Velocity dispersion of galaxies as a function of radius. Green squares are galaxies closer to the central galaxy major axis and blue triangles are galaxies closer to the central galaxy minor axis. The dashed gray line shows prediction from NFW.

The resulting profiles are shown in Figure 2.4. The dotted lines show the predicted weighted dispersion difference, with the colored bands representing the error of the mean determined by bootstrapping. The mean anisotropy of the velocity dispersion increases strongly with the angle between the line of sight and the major axis. Moreover, it is positive ($\sigma_v^{\mathrm{maj}} > \sigma_v^{\mathrm{min}}$) at all radii. The signal vanishes for sight lines parallel to the major axis of the halo. We checked that this result does not depend on the alignment of the intermediate and minor axes of the halos. Therefore, it is a direct consequence of the fact that halos are predominantly prolate (Gottlöber & Yepes, 2007).

Even though our calculation is based on purely dark matter simulation, the signal corresponding to random orientations of major axes of dark matter halos matches the observations with $\chi^2_{\mathrm{sim}}/\mathrm{dof} = 10.4/8 = 1.3$ (compared to $\chi^2_{\mathrm{iso}}/\mathrm{dof} = 15.3/8 = 1.9$ for an isotropic case, $\sigma_v^{\mathrm{maj}} = \sigma_v^{\mathrm{min}}$). We checked that the relative difference of the velocity dispersions only depends weakly on the halo mass and remains the same when we restrict our calculations to the halo masses corresponding to the selected richness range.

2.4.2 Systematics

Miscentering of the CG has the effect of boosting the measured velocity dispersion of galaxies. Because this boost is isotropic, it will tend to dilute the signal, while simultaneously increasing the observed velocity dispersion of the cluster stack. Furthermore, if the orientation of the ellipticity of the false centers is random this will likewise act to dilute the signal. We have attempted to minimize these systematics by requiring that all clusters be properly centered ($P_{\rm CG} > 0.95$), but strictly speaking our measurement can be thought of as a lower limit.

While CGs and host halos tend to be preferentially aligned in observed galaxy clusters, there is also a significant random component associated with the angular separation of their major axes (Niederste-Ostholt et al., 2010). This will tend dilute the observed signal relative to our predictions from numerical simulations. Thus, similarly in this case, one can think of our results as providing a lower limit to the anisotropic signal relative to the halo's major axis.

An additional concern is that because halo triaxiality depends on halo mass (e.g. Shaw et al., 2006), the relative satellite-weighted contribution of a single halo in a stack will be different along the major and minor axes. In other words, the effective halo mass distribution for stacks along the major and minor axes will be different, and this could lead to an artificial anisotropy signal. We have estimated the level of this effect by use of a toy model, in which we simulated the effect by generating stacks of galaxy velocities from clusters with mass dependent triaxialities, in the range described in Section 2.3.2. We found that, even when we we allow triaxiality to scale strongly with halo mass, the effect is negligible.

2.5 Discussion and conclusion

We present the first observational detection of anisotropic kinematics of galaxies in clusters of galaxies. We have measured line-of-sight velocity dispersions of member galaxies along the major and minor axes of the CG, in a large sample of stacked clusters from the SDSS. The projected CG position angle is used to separate galaxies into two section depending on their projected proximity to either axes. Galaxies closer to the projected CG major axis are found to have a preferentially larger velocity dispersion than those that are closer to the minor axis, with an average difference in dispersion of $\Delta\sigma_v = 38$ km s$^{-1} \pm 13$ km s^{-1}, corresponding to a relative difference of $\Delta\sigma_v/\langle\sigma_v\rangle = 6\% \pm 2\%$. These results are consistent with results from cosmological simulations, with $\chi^2_{\rm sim}/{\rm dof} = 10.4/8 = 1.3$.

The presence of this effect is a signature of a prolate velocity ellipsoid in galaxy clusters. Keeping in mind that velocity ellipsoid is aligned with the halo shape ellipsoid (Kasun &

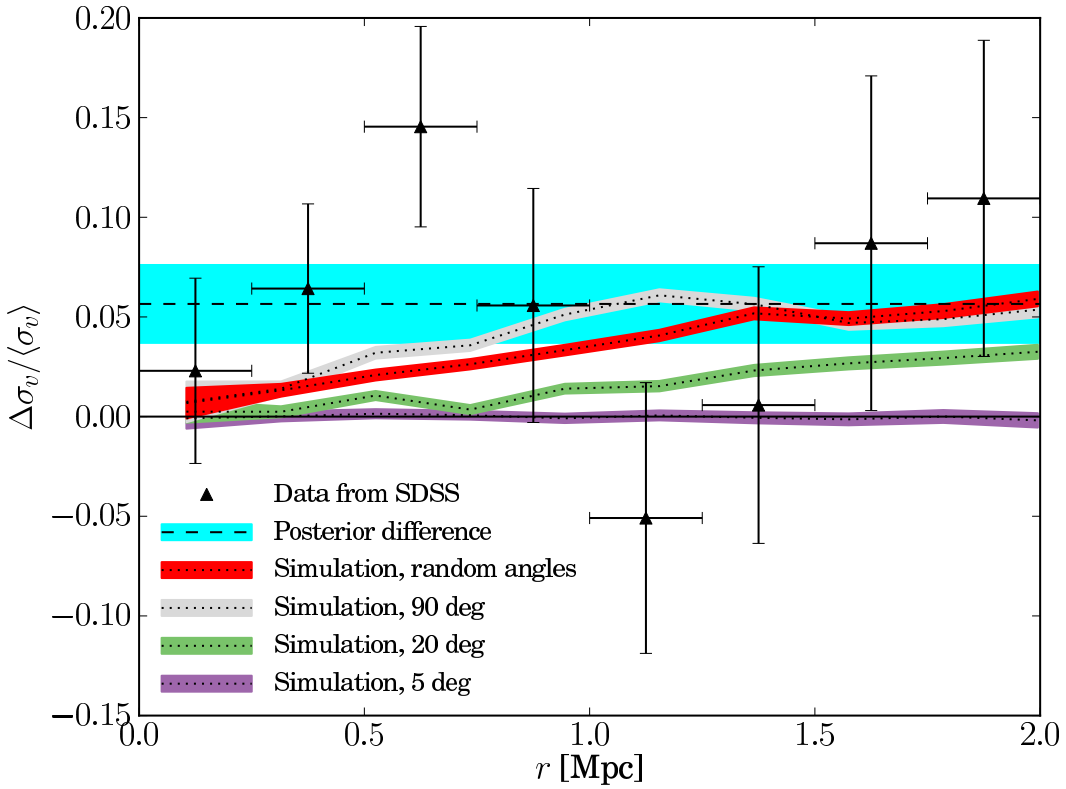

Fig. 2.4 Difference between galaxy velocity dispersion along projected major and minor axes of the CG, divided by the mean dispersion at the given radius. Positive values indicate $\sigma_v^{\rm maj} > \sigma_v^{\rm min}$. Triangles show results from our analysis of SDSS clusters. The dashed line (blue band) indicates the maximum likelihood for a constant offset ($\pm 1\sigma$ errors). The dotted lines (colored bands) show results from numerical simulations ($\pm 1\sigma$ errors from bootstrapping), with different lines corresponding to varying selection of angle between the line of sight and cluster halo major axis.

Evrard, 2005; Tormen, 1997; White et al., 2010) and the halos tend to be oriented with the cosmic web (Altay et al., 2006; Brunino et al., 2007), the effect is likely a remnant of an anisotropic halo formation (Sparre & Hansen 2012; R. Wojtak et al. 2012, in preparation). This raises an important question as to what extent cluster dynamics is influenced by the infall process and cluster location in the cosmic web. The result can also be interpreted in light of studies indicating preferential alignment between the CG and its host halo (Binggeli, 1982; Hashimoto et al., 2008; Niederste-Ostholt et al., 2010), strengthening the case for anisotropic cluster formation.

We furthermore find a clear correlation between the degree of projected anisotropy and the line-of-sight orientation of cluster halos in the simulations. This result opens exciting new possibilities for assessing the degree of random alignment of galaxy clusters. Specifically, it might be applied to a sample of optically selected clusters to evaluate the level of selection bias.

2.6 Acknowledgments

We warmly thank the referee, Andrea Biviano, for his comments and help in improving the manuscript. We thank Martin Sparre, Surhud More and Matthew Becker for helpful comments. Dark Cosmology Centre is funded by the Danish National Research Foundation. Kristian Pedersen acknowledges support from Instrument Center for Danish Astrophysics. Eduardo Rozo is funded by NASA through the Einstein Fellowship Program, grant PF9-00068. This work was supported in part by the U.S. Department of Energy contract to SLAC No. DE-AC02-76SF00515.

Chapter 3

Probing the structure of active galactic nuclei

This chapter contains the paper:

"Constraints on the broad line region from regularized linear inversion: Velocity–delay maps for five nearby active galactic nuclei"
Skielboe, A., Pancoast, A., Treu, T., et al. 2015, MNRAS, 454, 144

3.1 Abstract

Reverberation mapping probes the structure of the broad emission-line region (BLR) in active galactic nuclei (AGN). The kinematics of the BLR gas can be used to measure the mass of the central supermassive black hole. The main uncertainty affecting black hole mass determinations is the structure of the BLR. We present a new method for reverberation mapping based on regularized linear inversion (RLI) that includes modelling of the AGN continuum light curves. This enables fast calculation of velocity-resolved response maps to constrain BLR structure. RLI allows for negative response, such as when some areas of the BLR respond in inverse proportion to a change in ionizing continuum luminosity. We present time delays, integrated response functions, and velocity–delay maps for the Hβ broad emission line in five nearby AGN, as well as for Hα and Hγ in Arp 151, using data from the Lick AGN Monitoring Project 2008. We find indications of prompt response in three of the objects (Arp 151, NGC 5548 and SBS 1116+583A) with additional prompt response in the red wing of Hβ. In SBS 1116+583A we find evidence for a multimodal broad prompt response followed by a second narrow response at 10 days. We find no clear indications of

negative response. The results are complementary to, and consistent with, other methods such as cross correlation, maximum entropy and dynamical modelling. Regularized linear inversion with continuum light curve modelling provides a fast, complementary method for velocity-resolved reverberation mapping and is suitable for use on large datasets.

3.2 Introduction

Active galactic nuclei (AGN) are believed to be powered by the release of gravitational potential energy when matter falls onto supermassive black holes in the centres of galaxies. Some AGN have broad emission lines that are thought to be Doppler broadened emission from gas orbiting the central black hole. The broad lines vary in response to the continuum emission, suggesting that they are powered by ionizing radiation originating in the immediate vicinity of the black hole (Bahcall & Kozlovsky, 1969; Davidson, 1972). The time delay between the variations in the continuum and emission lines can be used to measure the structure and characteristic size of the broad emission line region (BLR) by the method of reverberation mapping (Bahcall et al., 1972; Blandford & McKee, 1982; Peterson, 1993).

The radius of the BLR combined with the width of the emission line provides a measurement of the mass of the central black hole (Peterson et al., 1998a; Kaspi et al., 2000). Reverberation masses have been found to correlate with properties of the host galaxy, such as stellar velocity dispersion (e.g. Ferrarese & Merritt, 2000; Gebhardt et al., 2000; Tremaine et al., 2002; Woo et al., 2010) and bulge luminosity (e.g. Bentz et al., 2009b; Kormendy & Ho, 2013), as has been found for black holes in inactive galaxies (e.g. Kormendy & Richstone, 1995; Magorrian et al., 1998; Ferrarese & Merritt, 2000; Gebhardt et al., 2000) and indicating a connection between supermassive black hole growth and galaxy evolution. In addition, BLR radii have been found to correlate with the UV/optical luminosity of the AGN (e.g. Kaspi et al., 2000, 2005; Bentz et al., 2009a, 2013), suggesting that AGN can be used as independent standard candles for cosmology (Watson et al., 2011; King et al., 2014). The radius-luminosity relation also enables black hole masses to be estimated out to large redshift ($z > 6$) by measuring the AGN luminosity and broad emission line width in a single spectrum, yielding single-epoch black hole mass estimates (e.g. Vestergaard, 2002; McLure & Jarvis, 2002; Vestergaard & Peterson, 2006; Shen, 2013).

Because of limited knowledge of the structure of the BLR, it is necessary to introduce a scaling factor in traditional reverberation mapping black hole mass measurements, such that the black hole mass is determined by

$$M_{\rm BH} = f\frac{\Delta V^2 R_{\rm BLR}}{G}, \tag{3.1}$$

where ΔV is the velocity width of the varying part of the emission line, G is the gravitational constant, and f is the order-unity scaling factor that encapsulates the unknown details regarding the BLR gas and kinematics (Wandel et al., 1999; Onken et al., 2004). The f-factor is generally calibrated using the $M_{\rm BH} - \sigma_\star$ relation between the black hole mass and the stellar velocity dispersion of the bulge in the host galaxy. This relies on determining $M_{\rm BH}$ independently in quiescent galaxies using stellar and gas dynamics (see Kormendy & Ho 2013 for a review), and then determining the average scaling factor $\langle f \rangle$ that brings the ensemble of active galaxies into agreement with the quiescent $M_{\rm BH} - \sigma_\star$ relation. This process only corrects for the average offset, but it results in black hole masses that are uncertain for any particular AGN by a factor of $2-3$. In addition, $\langle f \rangle$ is determined using Hβ, but often applied to other emission lines such as MgII λ2799 and CIV λ1549, although the structure of the BLR for these emission lines is very uncertain (Metzroth et al., 2006; Woo, 2008; Kaspi et al., 2007; Trevese et al., 2014).

The main uncertainty in measuring black hole masses using reverberation mapping thus comes from our limited knowledge of the kinematics and geometry of the BLR. A precise measurement of the kinematic and geometric structure of the BLR would improve our understanding of the physics and geometry behind the f-factor for nearby AGN, and could help inform empirical calibration efforts, that enable high redshift AGN single-epoch mass measurement. This could help reduce scatter in black hole mass determinations for all single epoch mass estimates and their applications (Kelly & Shen, 2013). A better understanding of changes in BLR structure with luminosity and redshift will also reduce systematic errors possibly affecting current scaling relations. To make a full map of the BLR we need to determine not just its characteristic radius, but also the full velocity-resolved transfer function that describes the relation between the continuum emission and the emission line response.

To first order, the problem of reverberation mapping can be formulated as a deconvolution problem in which the flux in the emission-line light curve, at a given wavelength λ, $F_l(t,\lambda)$ is given by a convolution of the AGN continuum light curve, over some wavelength range, $F_c(t)$ with a transfer function $\Psi(t,\lambda)$ that encodes the physics and geometry of the BLR,

$$F_l(t,\lambda) = \int_{-\infty}^{\infty} \Psi(\tau,\lambda) F_c(t-\tau) d\tau. \tag{3.2}$$

The transfer function, as a function of time delay and wavelength $\Psi(\tau,\lambda)$, is called the velocity–delay map (Welsh & Horne, 1991). In this approximation, the transfer function is assumed to be linear. Even though the detailed physics is likely to be more complicated, the linear approximation is currently sufficient given that observational datasets have only recently become good enough to probe the full velocity-resolved transfer function. Thus,

the transfer function introduced here represents an observed projection of the underlying structure of the AGN. A sound inference of the transfer function will need to account for any residual mismatches between the assumed model and the data, such as non-linearities.

Because transfer functions represent projections of the underlying physical structure, physical and geometrical models are required to interpret them. Several groups have gone through the exercise of predicting transfer functions based on underlying physical models for the BLR structure (e.g. Perez et al., 1992; Chiang & Murray, 1996; Bottorff et al., 1997; Goad et al., 2012). These studies provide a valuable catalogue of transfer functions that can be consulted when interpreting results from reverberation mapping.

Much effort has gone into developing efficient methods for estimating the BLR size and transfer function $\Psi(\tau, \lambda)$. Early attempts relied on estimating the time delay by-eye (Cherepashchuk & Lyutyi, 1973), but many sophisticated methods have been developed since. Blandford & McKee (1982) were the first to calculate transfer functions directly using the convolution theorem of Fourier transforms and provided a comprehensive catalogue of transfer functions for a number of idealised BLR structures. Unfortunately, the requirement for very high quality data, as well as difficulties in dealing with measurements errors, mean that the method has seen little application since its publication. This may change with future high cadence, high signal-to-noise reverberation mapping campaigns.

Another type of inversion procedure is the maximum entropy method that finds the solution for the transfer function that has the highest entropy, while still providing a good fit to the data (Skilling & Bryan, 1984; Krolik et al., 1991; Horne et al., 1991; Horne, 1994). Maximum entropy has been successful in estimating transfer functions and velocity–delay maps in a number of AGN (e.g. Krolik et al., 1991; Ulrich & Horne, 1996; Bentz et al., 2010b; Grier et al., 2013b). The downsides of maximum entropy are that it is computationally expensive, it relies on a number of assumptions about the shape of the transfer function, and it is difficult to carry out rigorous error analysis and model comparisons. The Subtractive Optimally-Localized Averages (SOLA) method by Pijpers & Wanders (1994) is another general inversion method method that estimates the 2D response as a weighted average of the emission line light curve data points (see also Horne 1999).

Another class of method is dynamical modelling in which a simplified physical model of the BLR is constructed, and its parameters are inferred within the framework of Bayesian statistics. The statistical framework allows for rigorous error analysis as well model selection (Pancoast et al., 2011). Furthermore, dynamical modelling circumvents the need for interpreting transfer functions by providing direct estimates of physical model parameters such as inclination and the black hole mass, which in turn allows for the f-factor to be calculated directly. Like other reverberation mapping methods, the current implementation

of dynamical modelling relies on the assumption that the BLR is in a stead configuration, and that the response is linear. The main challenges of dynamical modelling methods are that they require long computation times and the assumption that the model is flexible enough to provide a good description of the BLR.

Dynamical modelling and maximum entropy both provide useful and complementary constraints on the BLR structure. They also rely on a number of assumptions about the allowed shape of the transfer function and are fairly computationally expensive. It is therefore worthwhile to consider alternative methods for analysing reverberation mapping data that are less computationally expensive and allow for greater flexibility in estimating velocity-resolved transfer functions.

Here we develop a method for reverberation mapping based on regularized linear inversion (RLI; Vio et al., 1994; Krolik & Done, 1995), which we extend by including statistical modelling of the AGN continuum light curve light curves. The method is complementary to other reverberation mapping techniques, and has the advantage that it provides an analytical expression for the transfer function with very few assumptions about its shape. RLI is a flexible, free-form method, allowing the data to suggest the form of the inferred transfer function. This makes RLI an ideal tool for exploring BLR physics beyond the framework of current BLR models. At the same time RLI is one of the fastest reverberation methods that provides a direct estimate of the transfer function. We extend the RLI method to include error in the light curves by a combination of Gaussian process modelling and bootstrap resampling, thereby providing a robust estimate of the transfer function and its uncertainties.

As a first application, we apply our method to photometric and spectroscopic light curves of five nearby AGN measured by the Lick AGN Monitoring Project 2008 collaboration (LAMP 2008; Bentz et al., 2008). The main purpose of this project was to measure masses of supermassive black holes in 13 nearby ($z < 0.05$) Seyfert 1 galaxies (Bentz et al., 2009c). Besides improving black hole mass estimates, LAMP 2008 has produced a medley of scientific results including: AGN variability characteristics (Walsh et al., 2009), an update of the $M_{\rm BH} - \sigma_\star$ relation with reverberation mapped AGN (Woo et al., 2010), detailed reverberation mapping studies (Bentz et al., 2010a,b), probing the $R_{\rm BLR} - L$ relation in the X-rays (Greene et al., 2010), recalibrating single-epoch black hole masses (Park et al., 2012) and dynamical modelling of the Hβ BLR (Pancoast et al., 2014b).

We analyse five objects from LAMP 2008: Arp 151 (Mrk 40), Mrk 1310, NGC 5548, NGC 6814 and SBS 1116+583A, providing integrated response functions, time delays and velocity–delay response maps for the Hβ emission line in each object, as well as Hα and Hγ in Arp 151. We begin in Section 3.3 by describing how we obtained light curves from the LAMP 2008 dataset. In Section 3.4 we outline the RLI method and show results from

simulations. Section 3.5 presents the main results of our analysis. The results are discussed in Section 3.6 and finally we provide a short summary and conclusions in Section 3.7.

All time delay-axes in the figures are in the observed frame. All time delays quoted in the text and in Table 1 are in the rest frame of the AGN.

3.3 Data

We use data from LAMP 2008[1], a dedicated spectroscopic reverberation mapping campaign that ran for 64 consecutive nights at the Lick Observatory 3-m Shane telescope, with a median sampling rate of 1 day. The spectroscopic data were supplemented by photometric monitoring using smaller telescopes, including the 30-inch Katzman Automatic Imaging Telescope (KAIT), the 2-m Multicolor Active Galactic Nuclei Monitoring telescope, the Palomar 60-inch telescope, and the 32-inch Tenagra II telescope. A detailed description of the LAMP 2008 observing campaign and initial results are published in Walsh et al. (2009) and Bentz et al. (2009c).

3.3.1 Continuum light curves

For our analysis, we use Johnson B and V broad band continuum light curves from LAMP 2008. The bands were chosen to improve dynamical modelling results and resolve variability features. The fluxes are measured using standard aperture photometry (see Walsh et al. 2009 for a complete discussion). The light curves are the same as those used in dynamical modelling by Pancoast et al. (2014b). The B and V band light curves are very similar for all objects analysed (see Walsh et al., 2009), and the choice of continuum light should not significantly affect our results.

3.3.2 Emission line spectra and light curves

Emission-line light curves are generated from flux-calibrated spectra from the LAMP 2008 campaign. The Hβ emission line is isolated in all objects using spectral decomposition, by modelling all line and continuum components individually, and subtracting away everything but the emission line of interest (Park et al., 2012). We decide to keep the narrow component of Hβ to avoid introducing additional error at the centre of the line. This should not affect our results, as the narrow-line component is constant on the time-scale of the observing campaign (see Park et al., 2012), and because we only consider variations around the mean

[1]Data available at http://www.physics.uci.edu/~barth/lamp.html

flux in the line. In Arp 151 we also analyse the Hα and Hγ lines, where Hγ is isolated using spectral decomposition in a way similar to that for Hβ (Barth et al., 2011). Because no spectral decomposition is available for Hα we follow the procedure of Bentz et al. (2010a), isolating Hα by subtracting a straight line fit to two wavelength windows on either side of the line.

The resulting emission line spectra have the same spectral resolution as the original LAMP 2008 data. The spectral dispersions are provided in Bentz et al. (2009c) and range from $11.6 - 14.7$ Å (FWHM), corresponding to $5.9 - 7.5$ pixels per resolution element.

A few of the spectra in the LAMP 2008 dataset have been identified as unreliable due to low spectral quality or suspicious features above the noise (Park et al., 2012). We tested the effect of removing these spectra in the analysis and found that it made little difference to the overall results. Because of this, and to be able to compare directly with recent results from dynamical modelling (Pancoast et al., 2014b), we decided to include the unreliable spectra in the RLI analysis presented here. The emission line light curves for Hβ are thus identical to those used for the dynamical modelling analysis in Pancoast et al. (2014b).

3.4 Regularized linear inversion

Regularized linear inversion seeks to solve the transfer equation (Equation 3.2) for the transfer function $\Psi(\tau, \lambda)$ analytically and without any assumptions regarding its functional form (only that it is a bounded linear operator). This approach is potentially very powerful in that it relies solely on the data when deriving the transfer function. This in turn allows for very little freedom for the method to select a proper solution. In the presence of noise, or if the system deviates slightly from the linear assumption, this lack of freedom means that a solution cannot be found at all. Therefore, instead of looking for a unique solution that fits the data, the method determines the solution that minimizes the χ^2. A simple χ^2 minimization will generally over-fit the data and make the inversion unstable. This is overcome by a regularization in which the first-order derivative of the solution is to be minimized along with the χ^2, such that the solution is smoothed at the level of the noise (Phillips, 1962; Tikhonov, 1963). The result is comparable to maximizing the entropy under a χ^2 constraint as in the case of maximum entropy methods. RLI has several advantages over other methods, specifically it 1) makes no assumption about the shape or positivity of the transfer function, 2) can be solved analytically, and 3) has very few free parameters (the regularization scale as well as the transfer function window and resolution). Note that while RLI can in principle fit any shape of transfer function, in practice the result will be limited by the sampling and noise

in the data, which means that a minimum scale exists below which the response function will be unresolved.

By measuring the continuum (F_c) and emission line (F_l) light curves we can in principle solve the transfer equation (3.2) for $\Psi(t,\lambda)$. In reality, data is always discrete, so we rewrite the transfer equation as a linear matrix equation of the form

$$L_{\Delta\lambda} = \Psi_{\Delta\lambda}\mathbf{C}, \tag{3.3}$$

where $\mathbf{L}_{\Delta\lambda}$ is the emission line light curve integrated over the wavelength range (spectral bin) $\Delta\lambda$, $\mathbf{C}$ is a matrix of continuum light curves (see below), and $\Psi_{\Delta\lambda}$ is the transfer function corresponding to the given wavelength range. While we allow the transfer function to depend on wavelength, symmetries in the BLR as well as observational projections will tend to correlate transfer functions in the time and wavelength domains. The set of transfer equations over a range of frequencies across an emission-line we call the velocity–delay map for the given emission line (Welsh & Horne, 1991).

For perfect noise-free data solving the discrete transfer equation (3.3) would be a simple matter of inverting $\mathbf{C}$ to obtain the transfer function Ψ. Because of noise we cannot hope to find an exact solution to the linear inversion problem. Instead we seek a solution that minimizes the χ^2 together with a smoothing condition that ensures that we are not fitting the noise.

Interpreting the transfer function to make statements about the structure of the BLR relies on a number of assumptions. First, we assume that the variations in the AGN continuum bands are correlated with the AGN ionizing continuum (this is not necessarily true, see e.g. Collier et al. 1998; McHardy et al. 2014; Edelson et al. 2015 who find evidence for a time delay between the UV and optical continuum in NGC 7469 and NGC 5548). Second, we assume that the continuum emission originates from a region negligible in size compared to the BLR. Third, we assume that the continuum ionizing radiation is emitted isotropically. Last, we assume that the BLR structure is constant and the response linear for the duration of the campaign, such that a single linear transfer function can be calculated from the full light curves.

3.4.1 Solving for the response function

Rather than solving for the transfer function, which includes constant emissivity components of the BLR, we consider only variations about the mean of the light curves. By doing this, we are measuring the response of the line emission to a change in the continuum emission

that is ionizing the BLR gas. Hence the quantity we are solving for, $\Psi(\tau,\lambda)$, is the response function (Krolik et al., 1991; Goad et al., 1993).

Following the notation of Krolik & Done (1995), and considering only variation about the mean of the light curves, we write χ^2 as

$$\chi^2 = \sum_{i=M}^{N} \frac{1}{\sigma_l^2(t_i)} \left[\delta F_l(t_i) - \sum_{j=1}^{M} [F_c(t_i - \tau_j) - \langle F_c \rangle] \Psi(t_j) \right]^2, \tag{3.4}$$

where $F_c(t)$ is the continuum light curve, $F_l(t)$ is the emission line light curve, $\sigma_l^2(t_i)$ is the error on the emission line light curve, $\Psi(\tau)$ is the response function and τ is the time delay. Note that continuum light curve errors are not included in this expression (see Section 3.4.2). This expression can be recast to matrix notation,

$$\chi^2 = (\mathbf{L} - \mathbf{C}\Psi)^2, \tag{3.5}$$

where the light curves enter as

$$\mathbf{C}_{ij} = [F_c(t - \tau_j) - \langle F_c \rangle]/\sigma_l(t_i) \tag{3.6}$$

$$\mathbf{L} = \delta F_l(t_i)/\sigma_l(t_i), \tag{3.7}$$

and the variation about the mean in the emission-line light curve is defined as

$$\delta F_l(t_i) = F_l(t_i) - \langle F_l \rangle. \tag{3.8}$$

We choose a time delay resolution of 1 day, as this corresponds to the highest resolution of the data. By running the analysis with different resolutions we have confirmed that the choice of resolution, within reasonable values, does not change our results. Contrary to Krolik & Done (1995), we calculate a constant mean of the continuum light curve data points such that $\langle F_c \rangle$ is not a function of the time delay τ. This is done in order to allow meaningful comparisons between different continuum realizations (see Section 3.4.2). Minimizing χ^2 in Equation (3.5) leads to the linear equation

$$\mathbf{C}^{\mathbf{T}}\mathbf{C}\Psi = \mathbf{C}^{\mathbf{T}}\mathbf{L}. \tag{3.9}$$

Although this expression looks simple, it turns out to be ill-conditioned. To remedy this, we put an extra constraint on the problem, namely that the solution should be smooth at the scale of the noise (this effectively avoids fitting the noise). To guarantee smoothness of the solution, we introduce a differencing operator $\mathbf{H}$ acting on Ψ, and require that the first-order

difference (the discrete version of the first-order differential) be minimized together with the ordinary χ^2. To control the weights between the χ^2 and the first-order difference, a scaling parameter κ is introduced that sets the scale of the regularization. Thus, the expression to minimize becomes

$$(\mathbf{C^T C} + \kappa \mathbf{H^T H})\Psi = \mathbf{C^T L}. \tag{3.10}$$

This expression is more stable under inversion, while sacrificing detail by emphasizing smoothness of the solution. The question is then how to choose a suitable scale κ for the regularization.

The best choice of regularization scale depends on the signal-to-noise in the data, as well as the level of uncorrelated systematic uncertainties that result in deviations from the assumption of linear response. As a starting point for selecting a regularization scale κ, we follow the recommendation of Press (1992) in which $\kappa = \kappa_0$ is chosen to provide equal weights to the two left-hand-side terms in equation (3.10),

$$\kappa_0 = \frac{\mathrm{Tr}(\mathbf{C^T C})}{\mathrm{Tr}(\mathbf{H^T H})}. \tag{3.11}$$

Krolik & Done (1995) suggest using the largest value of κ which gives an acceptable χ^2, while Vio et al. (1994) suggest using a value of κ which provides the "best" trade-off between resolution and noise. We test the choice of $\kappa = \kappa_0$ by applying RLI to both simulated data (see Sec. 3.4.4) as well as data from LAMP 2008 (see Sec. 3.4.6), and find that good results are generally achieved for $\kappa = \kappa_0$. For this reason, and to reduce the number of free parameters in the method, we fix $\kappa = \kappa_0$ for all our analysis (see Section 3.4.6 for a test of the effect of changing the regularization scale).

We calculate all response functions in the time delay interval $0 - 30$ days. The lower bound is chosen to impose causality in the solution. The upper bound is chosen to be well beyond the time-scale where we expect a significant response based on previous measurements and expectations for Seyfert galaxies (Bentz et al., 2013). We tested the effect of changing the time delay windows and found that it had only minor effects on the results, as longs as the window is long enough to include the main response. When presenting the results, we show only the first part of the response function from $0 - 15$ days, as we found the significant response power to be located at these scales.

3.4.2 Continuum light curve errors

Continuum flux errors are not included explicitly in the RLI formalism presented above. Instead, we include continuum errors and interpolation by modelling the continuum light

curves using Gaussian processes (Pancoast et al., 2011). Studies of AGN variability, using sampling intervals of days, have suggested that AGN continuum variability is well modelled by a damped random walk or Ornstein–Uhlenbeck (O–U) process (Kelly et al., 2009; Kozłowski et al., 2010; MacLeod et al., 2010; Zu et al., 2013). Formally this is a CAR(1) or continuous-time first-order autoregressive process, which is a stationary Gaussian process with a power spectral density (PSD) slope of -2. The CAR(1) process is often used in reverberation mapping methods for modelling the continuum light curve and enable efficient interpolation and error estimation (e.g. Zu et al., 2011; Pancoast et al., 2011).

Recent high cadence observations of AGN using the *Kepler* spacecraft (Mushotzky et al., 2011; Carini & Ryle, 2012; Edelson et al., 2014; Kasliwal et al., 2015), have found steep PSD slopes (< -2) inconsistent with a CAR(1) process. The effect of having a steeper PSD slope is to suppress small scale variability in the light curves. Using a CAR(1) process for modelling the continuum light curves may therefore result in over-fitting spurious features, due to noise at short time scales. This introduces artificial structure at the level of the noise, that can lead to underestimated errors being propagated form the continuum model to other reverberation mapping parameters.

The magnitude of the error introduced by assuming the wrong continuum model depends on the sampling rate and errors in the data, as well as how it is implemented in the reverberation mapping method. Regularized linear inversion, as implemented here, mitigates the effects noise in the light curves by smoothing the solution at the shortest time scales. This results in a solution that is dominated by the longer multi-day variability features. For this reason, the response functions derived should not be affected by the details of the assumed continuum model, as long as multi-day time scale features are accurately reproduced. Even so, the shallower slope of the CAR(1) process, compared to *Kepler* AGN light curves, may still lead to underestimated errors.

To determine how the choice of continuum model PSD affects our results, we run RLI using a number of different continuum models with varying degrees of small scale structure, corresponding to varying PSD slopes. We do this by changing the power α in the covariance function for the Gaussian process. The covariance is given by (Pancoast et al., 2011)

$$C(t_1,t_2) = \sigma^2 \exp\left[-\left(\frac{|t_2-t_1|}{\tau}\right)^{\alpha}\right], \tag{3.12}$$

where σ is the long-term standard deviation, τ is the typical time scale of variations and the power α take on values in the interval $[1,2]$. A power of $\alpha = 1$ corresponds to the CAR(1) model, whereas $\alpha > 1$ produces smoother continuum models, with PSD slopes < -2. Using data from LAMP 2008 for Arp 151 (see results in section 3.5.2), we test four different

continuum models with $\alpha = 1.0$, 1.8, 1.9 and 2.0 respectively (see Fig. 3.1). We find that the emission line fits and response functions are not strongly affected by the assumed continuum model. For this reason, and to be consistent with other reverberation mapping methods such as JAVELIN and dynamical modelling, we choose to use a CAR(1) process as a prior for the Gaussian process continuum modelling. Future analyses of high-cadence reverberation mapping data should likewise be careful in considering the effects of the assumed continuum model.

The finite sampling and duration of the light curves hampers our ability to model structure on scales close to or below the sampling time scale, and on scales longer than the duration of the light curve. At short time scales the light curves will likely be dominated by observational errors due to the small fractional variability at these scales. Regularized linear inversion deals with this by smoothing the solution at the smallest time scales, resulting in a solution dominated by the longer multi-day variability features. For all the objects analysed, the time scale of interest (a few days) is well within the sampling rate of the data.

For each continuum light curve we find the best fit Gaussian process parameters using the DNEST3 Nested Sampling code by Brewer et al. (2010). The best-fit Gaussian process is used to interpolate the continuum light curve, which we need to calculate the response for arbitrary time delays.

In addition to interpolation, we use the statistical variability of the Gaussian process to generate a number of realizations of the continuum light curve that are used to estimate statistical errors on the calculated response functions. This allows us to include measurement errors in the continuum light curves that otherwise do not explicitly enter in the RLI formalism. For each continuum light curve, we generate 1000 realizations of the best-fit Gaussian process. This library of continuum realizations is used throughout the analysis to calculate response functions and response maps.

3.4.3 Emission-line light curve errors

Emission-line light curve errors $\sigma_l(t)$ are included explicitly in the RLI formalism in eqs. (3.6) and (3.7). We allow for the possibility of additional systematic errors in the emission line fluxes by bootstrap resampling of the emission line light curves in each inversion. Bootstrap resampling is done by re-sampling data points in the light curve, such that each point can be chosen zero or more times and the total number of data points is kept constant. If a point is chosen N times, its error is reduced accordingly by $\sqrt{N}$. We find that the results are only weakly affected by bootstrap resampling, indicating that systematic uncertainties affecting individual epochs in our data sample do not have strong influence on the results.

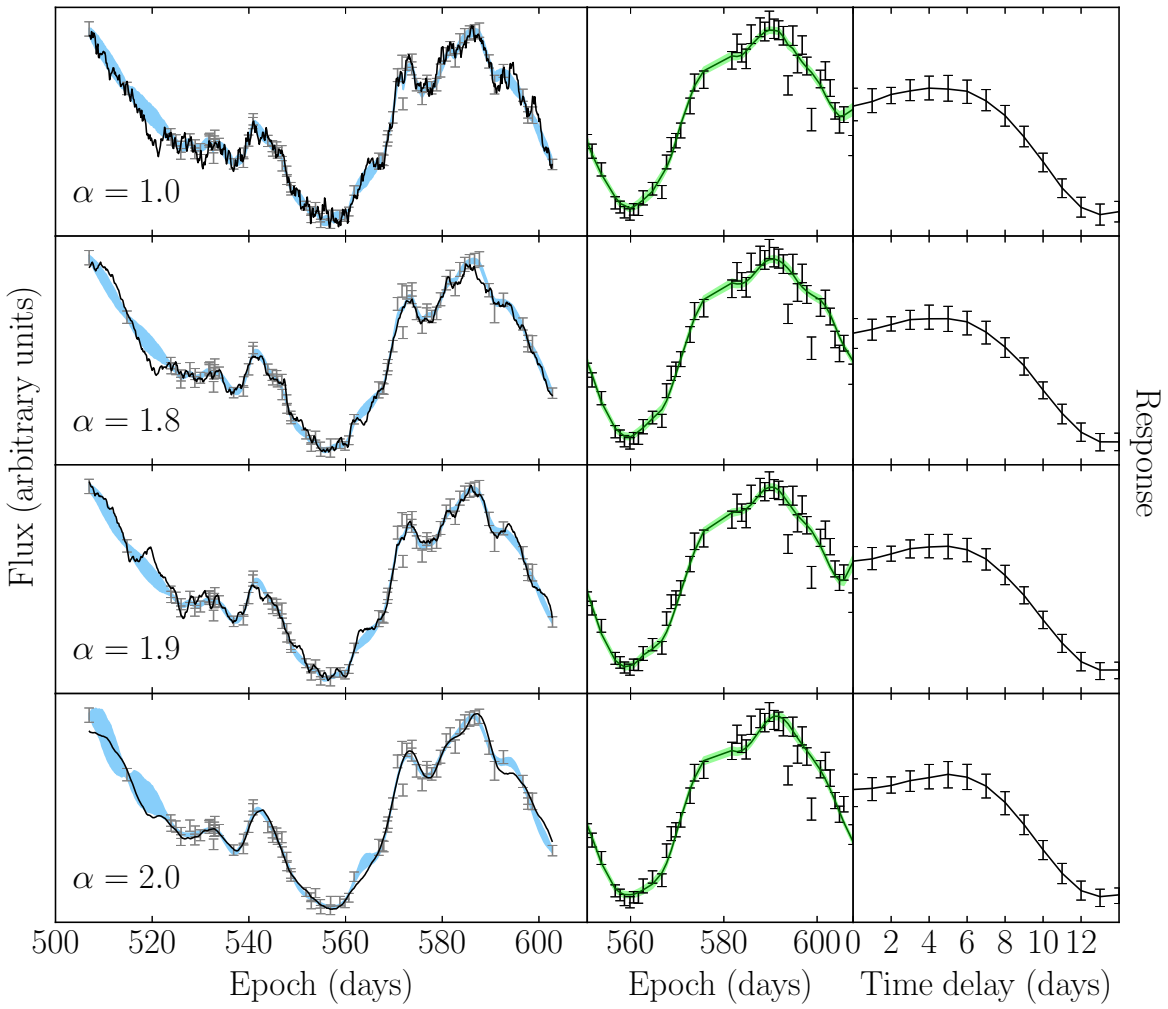

Fig. 3.1 The effect of using continuum models with varying levels of small scale structure. The upper panels show the CAR(1), $\alpha = 1.0$ in Equation (3.12), continuum model used for the results in this paper. The panels below show results for continuum models with increasing α, resulting in decreasing structure at short time scales, corresponding to progressively steeper, or more negative, power spectral density slopes. The left panels show the continuum light curve of Arp 151 from LAMP 2008 as grey error bars. In each case, the best fit (median and 1σ percentiles) continuum model is shown as a blue band and a single realization of the best fit continuum model is shown as a solid black line. The middle panels show the Arp 151 Hβ emission line light curve (black error bars) along with the fit from RLI (green line and band) using the corresponding continuum models on the left. The right panels show the resulting response functions from RLI. The excellent agreement between response functions derived using different continuum models leads us to conclude that the level of short time scale structure in the continuum model does not affect the RLI results derived from the LAMP 2008 dataset.

3.4.4 Testing on simulated data (1D)

We test our RLI method on simulated velocity-integrated (1D) light curves convolved with a selection of different response functions to produce a continuum-emission line light curve pair. To make the light curves as realistic as possible, the continuum light curve is simulated using a Gaussian process with a power spectral density similar to that found by recent Kepler observations (Edelson et al., 2014). The normalization of the simulated continuum light curve is chosen to match that of typical LAMP 2008 light curves (Bentz et al., 2009c), such that the simulated continuum has a fractional variability of $F_{\rm var} \sim 12$ per cent ($F_{\rm var}$; Vaughan et al., 2003) and a signal-to-noise ratio of SNR ~ 100. Emission line light curves are generated by convolving the simulated continuum light curve with the chosen response function (see Fig. 3.2). The simulated light curves are degraded and down-sampled to a level similar to the LAMP 2008 dataset (see section 3.3). We test our code on five different response functions: top-hat, multimodal top-hat, Gamma distribution, sinusoidal, and a delta function. The simulated light curves and response functions are shown together with the fits from RLI in Fig. 3.2. We further test our method by simulating continuum light curves using a damped random walk. Regularized inversion performs slightly better in this case, especially for small values of κ, due to the increased structure at short time scales, but the overall results are very similar to the simulated Kepler light curves shown in Fig. 3.2.

RLI is generally successful in recovering all simulated response functions, but like all reverberation mapping methods the overall performance depends on the number of strong variability features in the light curve sample. Because of the smoothing constraint and the finite sampling of the light curves, RLI cannot fit very sharp features in the simulated response functions. This is particularly evident in the case of the top-hat and delta function response functions. For the smooth Gamma and sinusoidal distributions, we find that RLI is able to match the full shape of the response function. To test the stability of these results we generated a number of light curves using the prescription described above, yielding a number of different realizations of the light curves in the left panels of Fig. 3.2. We found that the overall shapes of the recovered response functions were constant in the right panels of Fig. 3.2, but the small scale deviations were different. This indicates that the deviations in the response functions at particular time delays are driven by noise in the input data, and thus cannot be reduced without re-sampling, or extending, the light curve.

The smallest scale resolvable by RLI can be seen in the recovery of the delta-function in the bottom panel in Fig. 3.2. This smallest scale, or point spread distribution, comes from the incomplete sampling of the light curves as well as the smoothing imposed on the solution to avoid fitting noise in the input.

We test the effect of changing the regularization scale κ by one order of magnitude in each direction. The effect of increasing the regularization ($\kappa/\kappa_0 = 10$, dashed blue line in Fig. 3.2) is to smooth the response functions, thereby reducing some of the fluctuations in the wings, but also significantly increasing the width of the PSF (Fig. 3.2, lower right panel). In the same way, a reduction in regularization scale ($\kappa/\kappa_0 = 0.1$, dotted red line in Fig. 3.2) tends to amplify spurious features in the response functions while improving the PSF by decreasing its width. The best trade-off between high resolution and signal-driven results is a matter of preference. We find that $\kappa = \kappa_0$ provides a good balance between resolution and noise. For this reason, and for consistency, we fix the regularization scale to $\kappa = \kappa_0$ for all our analysis.

It is important to note that these simulations assume an exact linear relation between the continuum and emission line, Equation (3.2), including only random errors and sampling gaps. The simulations and the results from RLI presented in Fig. 3.2 thus represent an artificial best-case scenario. The main purpose of Fig. 3.2 is to illustrate the effect of changing the regularization scale κ, show the finite point spread distribution of the RLI method due to discrete sampling, and the ability of RLI to recover negative and multimodal response functions.

3.4.5 Testing on simulated data (2D)

In addition to testing one-dimensional response functions, we test our RLI implementation on data simulated using the geometric and dynamical model of the BLR used in dynamical modelling of reverberation mapping data (Pancoast et al., 2011; Brewer et al., 2011). The dynamical modelling method simulates the broad line region as a number of discrete point particles in a parametrized geometrical configuration. We test RLI on two different simulated BLR configurations, one in which the BLR particles are in near-circular orbits, and one with entirely inflowing orbits (see Pancoast et al. 2014a for details on the simulated datasets). The results are shown next to the true response maps in Fig. 3.3. We note that the data are simulated using a kinematic and geometric model for the BLR, and are not necessarily representative of true AGN response maps.

These simulations provide a qualitative indication of the 2D point-spread-function of the RLI method. Because the solution is forced to be smooth in the presence of noise, the resulting response maps will not reproduce the input maps exactly. Instead, we retrieve a smoothed version of the input response maps. The stripes in the RLI maps appear because we analyse each velocity bin individually. This means that the solution is not smoothed in the velocity (or wavelength) direction. We did this to simplify the calculations and to let any correlations between velocity bins be driven by the data only. This is contrary to maximum

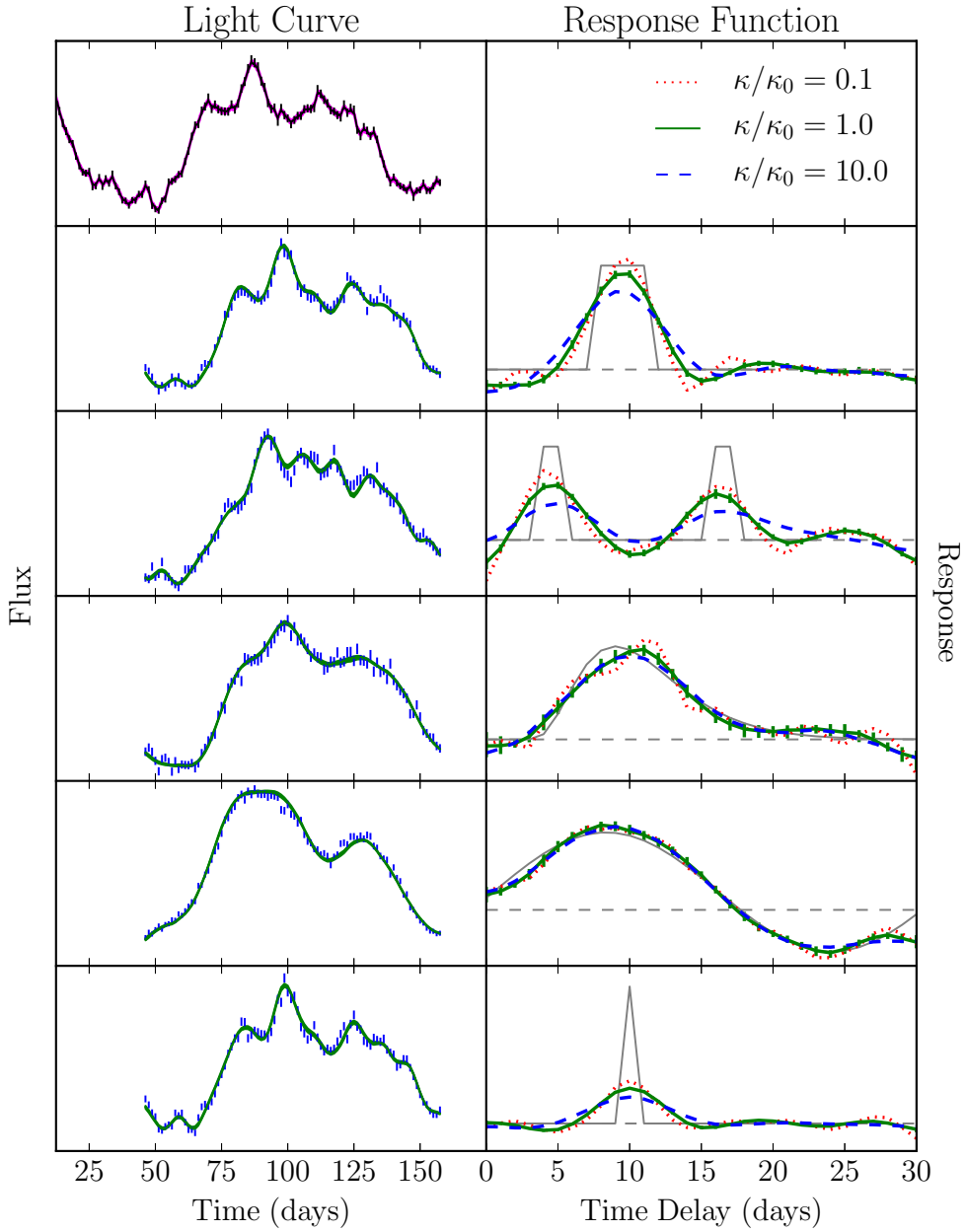

Fig. 3.2 Testing regularized linear inversion on simulated data by recovering response functions for simulated light curves. All vertical axes are linear. The top left panel shows the simulated continuum light curve, generated using a Gaussian process with a power spectral density similar to that found by recent Kepler observations (Edelson et al., 2014). The magenta band plotted on top of the continuum shows the standard deviation of the Gaussian process fit used in the analysis. The left panels, below the continuum, show the emission line light curves obtained by convolving the continuum with the corresponding response functions shown in the right panels. Before being analysed, the simulated light curves are degraded and down sampled to a level similar to the light curves of LAMP 2008. The response functions recovered from regularized linear inversion are plotted on top of the input response functions in the right panels. The thin black line is the input response function while the solid green (red dotted and blue dashed) lines shows the response functions calculated from regularized linear inversion with a regularization scale of $\kappa/\kappa_0 = 1$ ($\kappa/\kappa_0 = 0.1$ and $\kappa/\kappa_0 = 10$). The response functions are, from top to bottom: top-hat, multimodal top-hat, Gamma distribution, sinusoidal, and the delta function. The grey dashed horizontal lines indicate the level of zero response.

entropy, where the result is also smoothed (or regularized) in the velocity direction. If some velocity bins have exceptionally large errors, RLI might fail in that bin and produce a flat response.

Although the response maps from dynamical modelling and RLI look somewhat different, they share some of the same symmetries. The effect of in-fall in the upper panel in Fig. 3.3 is clearly recovered in the RLI map. Likewise, the lower panel in Fig. 3.3 shows that dynamical modelling and RLI both show a symmetric response on either side of the emission-line centre, suggesting a structure where the BLR clouds are on closed orbits around the central black hole.

It is unclear why the RLI method tends to prefer slight longer time delays in the lower panels in Fig. 3.3. It is important to note that the data used for this comparison were generated using a particular set of parameters in the geometrical model implemented by the dynamical modelling method. It is therefore reasonable to expect that dynamical modelling will do a better job at reconstructing the details of the 2D response maps, compared to RLI. Because RLI depends on a procedure where the input data is smoothed to reduce the effects of noise, its response reconstruction will perform better on smooth datasets where the response is continuously distributed over a larger area in the 2D response plane, than is the case for the simulated data used in Fig. 3.3.

3.4.6 Effect of changing the regularization scale κ

Fig. 3.4 shows the effect of changing the regularization scale κ using the Hβ data for Arp 151 as an example (see full results in Section 3.5.2). We find that, for low vales of κ (i.e. more weight on the χ^2-term), the solution is very unstable to perturbations in the input, and the error in the response function increases at all time delays. The reason that the error is not a function of time delay, is that the noise is not correlated with the signal in the light curve. Therefore, the response function can draw power at any time delay to fit the noise, so long as it draws similarly less power at other scales. Because the noise is random in each continuum realization, the time delays at which the response function draws its power will be evenly distributed in delay space, and the response function will fluctuate with more or less the same amplitude at all time delays. There will still on average be more power at scales correlated with the signal, thus the median shape of the response function peaks around the true delay, but the amplitude variations due to noise produce large error bars at all time delays. This behaviour is expected and illustrates the need for regularization to achieve stable solutions.

The solutions in Fig. 3.4 do not have similar chi^2 values. In fact, determining the optimal value of chi^2 in RLI is problematic for several reasons. Most importantly, the individual measurements in the light curves are significantly correlated, so the sum of the squared errors

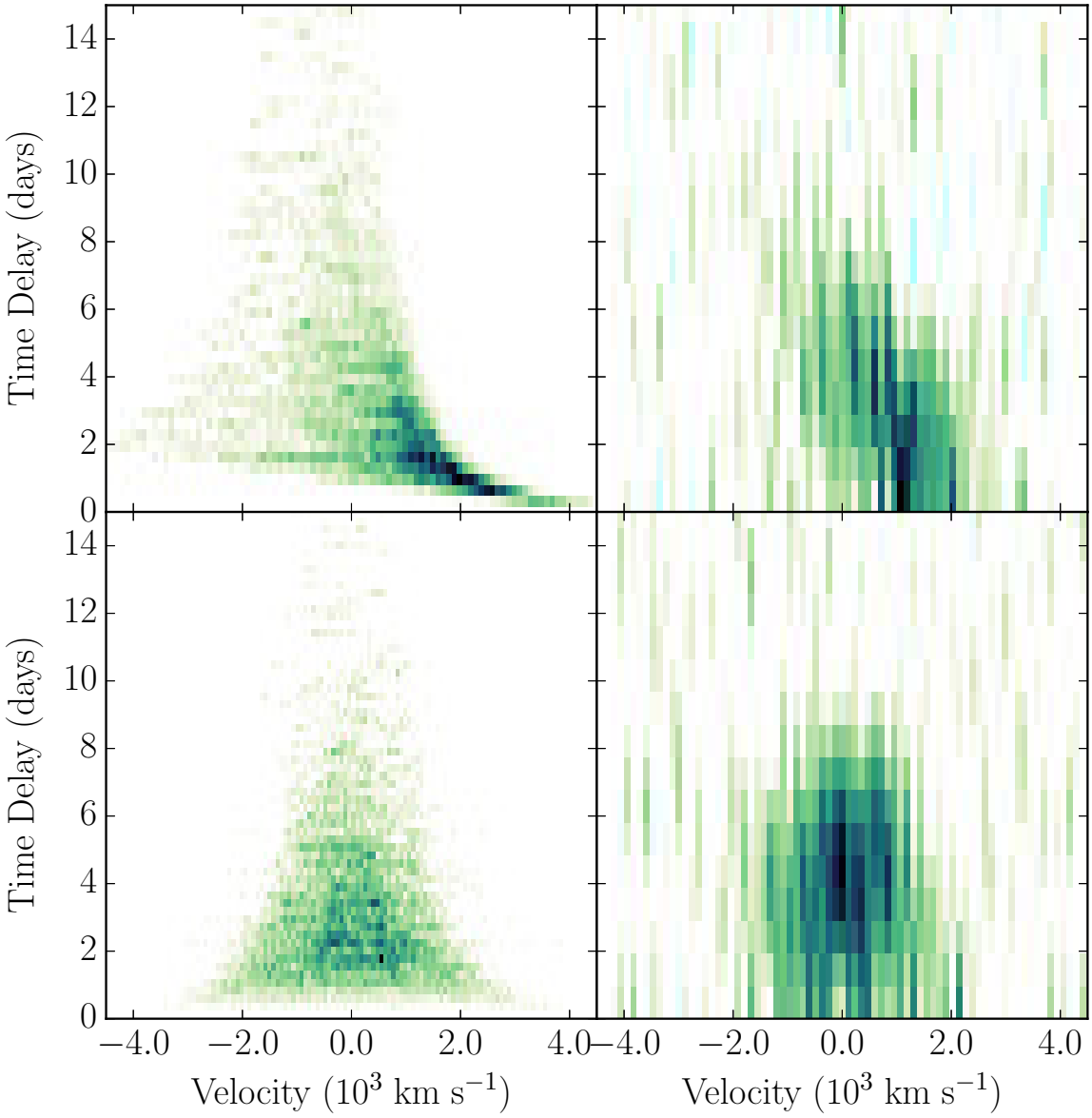

Fig. 3.3 Testing regularized linear inversion on simulated two-dimensional response maps (left column) generated using the dynamical modelling code of Pancoast et al. (2014a). The response functions are calculated for each velocity bin individually using RLI, and then plotted together to produce velocity–delay maps (right column).

is not well described by a chi^2 distribution. Determining the correct number of degrees of freedom, to estimate the expected chi^2 value, is problematic for the same reasons. As long as the systematic errors in the data are not exactly known, the choice of regularisation scale will have to be made using subjective criteria. We use the recommendation of Press (1992), and qualify this decision by test on simulated data (Fig. 3.4).

As the regularization scale is increased, more weight is put on the smoothness of the solution. This suppresses the effects of noise in the input and emphasizes the large scale behaviour of the light curves. Because of the smoothing introduced in the regularization, there will be a minimum resolvable scale, analogous to an extended point-spread-function (see Fig. 3.2). Any structure below the noise level will thus be smoothed out in RLI.

3.5 Results

Here we present results from regularized linear inversion of light curves of five local AGN from the LAMP 2008 dataset. Fig. 3.5 to 3.11 show results from regularized linear inversion of broad band photometric continuum light curves and Hβ light curves from spectral decomposition. We provide fits to the light curves as well as integrated response functions and velocity–delay maps for all object. Table 3.1 lists derived median time delays for the integrated light curves of all AGN analysed, as well as time delays from cross-correlation and JAVELIN for comparison.

3.5.1 Analysis

Light curves

The upper left panels in Fig. 3.5 to 3.11 show the observed light curves plotted as black points with error-bars. The blue band on top of the continuum light curve shows the median and 1σ percentiles of 1000 realizations of the Gaussian process best-fit model. This band indicates the range of continuum light curve realizations used together with bootstrap resampling to determine errors on the derived response functions (see Sections 3.4.2 and 3.4.3). The middle left panels show the integrated emission-line light-curves obtained by integrating the corresponding emission-line over the wavelength range listed in Table 3.1. The solid line and green band on top of the emission line light curves show the median and 1σ percentiles of the fits obtained from RLI when analysing all 1000 realizations of the continuum together with 100 bootstrap resamplings for each continuum realization.

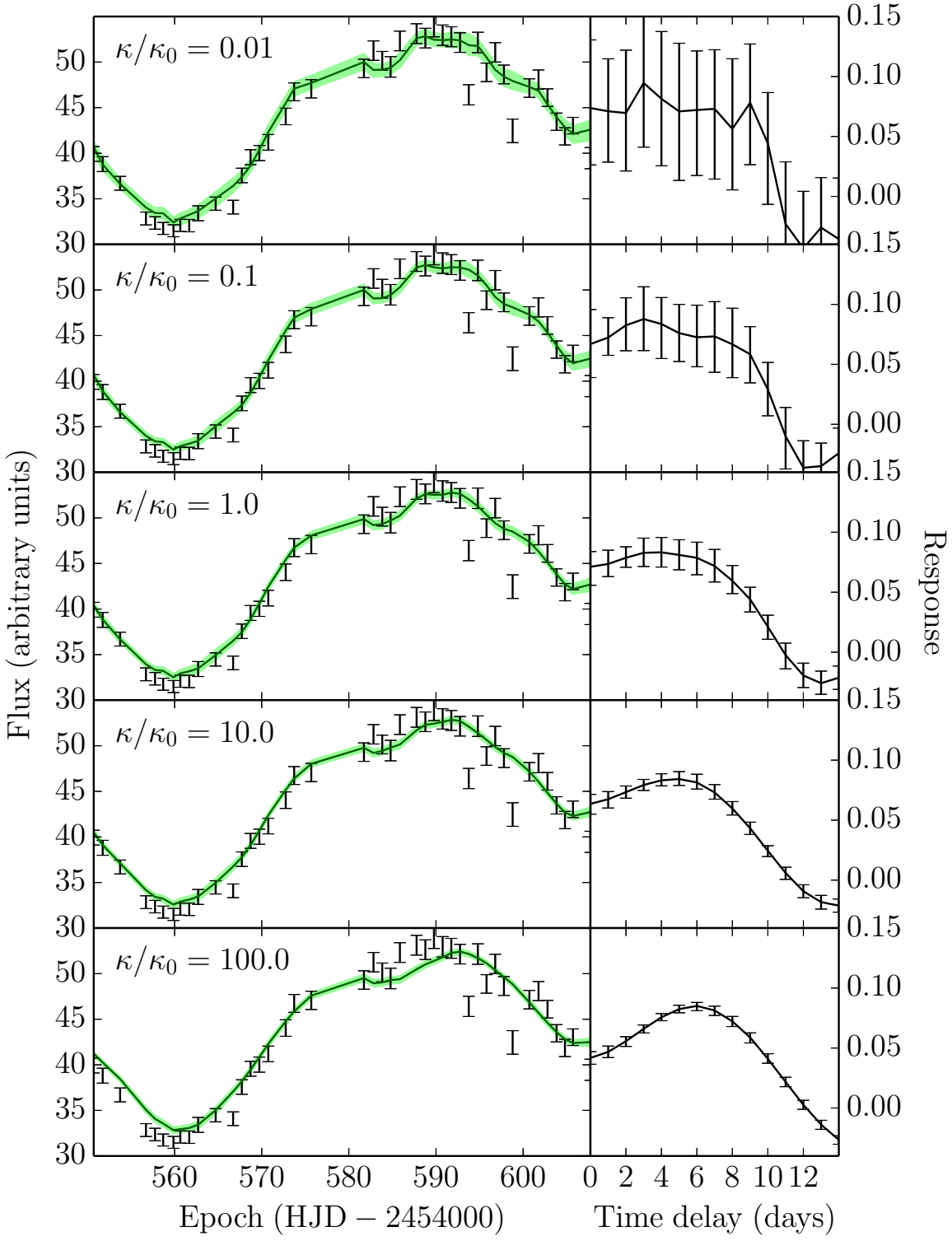

Fig. 3.4 Effect of changing the regularization scale κ, increasing the smoothness of the solution. Using Arp 151, Hβ as an example. The left panels show the Hβ light curve (black points with error bars) along with the fit from RLI (solid green line and band). The right panels show the corresponding response function found using RLI. The regularization scales affects all time scales in the response function equally, which is why the error bars are more of less constant as a function of time delay for each regularization scale κ.

Integrated response functions

The lower left panels of Fig. 3.5 to 3.11 show the best-fit integrated response functions under the smoothing constraint described in Section 3.4. The response function and the associated error-bars are calculated from the median and 1σ percentiles of RLI using 1000 iterations of continuum light curve interpolations as well as 100 bootstrap resamplings of the emission line light curve. Because we minimize not just the χ^2, but also the first derivative of the response function, the medians and error-bars of the response functions will be naturally correlated.

Velocity-resolved response functions

The upper right panels of Fig. 3.5 to 3.11 show the velocity–delay maps from regularized linear inversion of the spectra for all epochs in the data. Each spectral bin is treated individually, such that any correlations below the pixel resolution (see Section 3.3.2) are driven by the data. As in the case of the integrated analysis, we fix the regularization scale to $\kappa = \kappa_0$ for all velocity bins.

The velocity–delay maps show the response on a linear scale as a function of time delay and Doppler velocity with respect to the emission-line centre. White colour corresponds to zero response while black is maximum response (see the colour bars for each individual object). Below the response maps we plot the spectrum of the corresponding emission line. The black line is the mean spectrum across all epochs considered and the grey line is the root-mean-square variability (standard deviation about the mean) of the spectra, normalized to the same scale as the mean spectrum.

The lower right panels of Fig. 3.5 to 3.11 show a selection of response functions for three separate velocity-bins. The location of the bins are indicated by the vertical dashed lines in the response maps and spectra. The colours correspond to the relative wavelengths, such that the red response function is for the highest radial velocity bin (redshifted with respect to the line centre), the green response function is for the line centre at 0 km/s and the blue response function is for the lowest radial velocity bin (blueshifted with respect to the line centre).

The time delay

The scalar time delay from cross correlation methods, τ_{CCF}, is typically calculated as the centroid of the CCF above a threshold (usually 80 per cent of the maximum of the CCF). This effectively ignores any contributions from negative response. To compare our results to those from cross correlation, we calculate a RLI time delay, τ_{RLI}, as the median of the positive values of the response function. The time delays and error bars for each emission

line and object, quoted in Table 3.1 and in the text, are then estimated as the median and 1σ percentiles of all time delays determined from the response functions of all continuum realizations (see Sections 3.4.2 and 3.4.3). All time delays quoted in the text and in Table 3.1 are in the rest frame of the AGN. The time delay units on the axes of the figures are in the observed frame.

Comparing with other methods

We compare our results to those of other methods, including cross-correlation, JAVELIN, maximum entropy, and dynamical modelling.

The cross-correlation method calculates the cross-correlation function (CCF) between the continuum and emission line light curve to find the time delay, generally characterized by the centroid of the CCF, of the responding gas in the BLR. First applied by Gaskell & Sparke (1986), the method has since been substantially developed (e.g. Edelson & Krolik, 1988; White & Peterson, 1994; Peterson et al., 1998b). The CCF is related to the transfer function through the light curve auto-correlation function (Penston, 1991). This means that the width of the CCF depends on the variability characteristics of the AGN as well as the sampling of the data. For this reason, the CCF is rarely interpreted by itself, but is rather used as a tool to estimate the characteristic size of the BLR by calculating the time delay. Table 3.1 compares integrated time delays from RLI to time delays determined using cross correlation methods by Bentz et al. (2009c) for Hβ and Bentz et al. (2010a) for Hα and Hγ. Fig. 3.12 compares velocity-resolved time delays from RLI to velocity-resolved time delays from cross correlation of the Hβ line by Bentz et al. (2009c). The comparisons for each object are described in Section 3.5.2. See the previous section for a description of how the RLI time delays are estimated from the response functions.

JAVELIN finds the time delay by using a top hat model for the transfer function (Zu et al., 2011). Light curve variability is modelled using a CAR(1) process, which is the same process used to model the continuum variability in our RLI method. Like the cross-correlation method, JAVELIN provides only a scalar time delay as a measure of the BLR structure. Grier et al. (2013a) determined time delays using JAVELIN on the LAMP 2008 dataset. We list time delays from Grier et al. (2013a) in Table 3.1 alongside results from cross-correlation and RLI for comparison. All JAVELIN time delays τ_{JAVELIN} quoted in the text are also from Grier et al. (2013a).

The dynamical modelling method (Pancoast et al., 2011, 2014a) implements a full three-dimensional model of the BLR. The BLR emission is modelled as coming from a number of point particles that are drawn from a parametrized phase space distribution and linearly reprocess radiation from a central source. All measured parameters have a direct physical

interpretation, which means that the black hole mass $M_{\rm BH}$ and the virial factor f can be determined directly. Dynamical modelling results include fully velocity-resolved transfer functions. Because the method is based on a physical model of the BLR, the response will be correlated across velocity bins. This is contrary to our implementation of regularized linear inversion, where each velocity bin is analysed individually.

Another important difference between dynamical modelling and RLI is that, because dynamical modelling traces photons through the BLR to the observer, the resulting velocity–delay maps are transfer functions representing the absolute reprocessed emission. This is contrary to RLI which subtracts the mean component of the light curves to only calculate the response in the emission-line to variations in the continuum, thus measuring response (rather than transfer) functions. However, in the current implementation of dynamical modelling by Pancoast et al. (2011), the responsivity of the BLR gas is assumed to be constant throughout the BLR. In other words, the response of the BLR is correlated one-to-one with the emissivity distribution, regardless of the level of ionizing continuum. Because of this, the transfer functions and response functions will be directly proportional, and we can compare response maps from RLI to the velocity-resolved transfer functions of dynamical modelling directly.

Maximum entropy methods (Skilling & Bryan, 1984; Krolik et al., 1991; Horne et al., 1991; Horne, 1994) work by selecting solutions to the convolution problem (Equation 3.2) that simultaneously provide a good fit to the data while being as simple (smooth) as possible. The transfer functions are proposed based on a number of assumptions about the form of the solutions. This means that, like the dynamical modelling method, the derived response values will be dependent across velocity bins and the selection of the solution with the maximum entropy tends to result in very smooth velocity–delay maps. This is similar to RLI except that we impose no correlations between velocity bins, so any correlations between bins will be driven purely by the data. We compare our results to the response map for Hβ in Arp 151 from maximum entropy (Bentz et al., 2010b) and dynamical modelling (Pancoast et al., 2014b) in Fig. 3.13. The comparisons are described in Section 3.5.2.

3.5.2 Results for each AGN

Arp 151

Results for Arp 151 are presented in Fig. 3.5 for Hβ and Fig. 3.6 and 3.7 for Hα and Hγ respectively. Light curves for Arp 151 are the most variable and highest quality of the LAMP 2008 dataset, which is why we include only Hα and Hγ for this object. RLI provides decent fits to the Arp 151 light curves, with some notable outliers at later epochs (e.g. Hβ, Fig. 3.5). Because of the smoothing constraint imposed on the solution we do not expect our code to fit

Object	Continuum Band	Emission Line	Wavelength Range (Å)	Time delay (days)		
				$\tau_{\rm CCF}$	$\tau_{\rm JAVELIN}$	$\tau_{\rm RLI}$
Arp 151	*B*	Hα	6575 - 6825	$7.8^{+1.0}_{-1.0}$		$6.8^{+0.9}_{-1.4}$
Arp 151	*B*	Hβ	4792 - 4934	$4.0^{+0.5}_{-0.7}$	$3.6^{+0.7}_{-0.2}$	$4.0^{+0.7}_{-0.8}$
Arp 151	*B*	Hγ	4310 - 4393	$1.4^{+0.8}_{-0.7}$		$3.0^{+0.8}_{-0.8}$
Mrk 1310	*B*	Hβ	4815 - 4914	$3.7^{+0.6}_{-0.6}$	$4.2^{+0.9}_{-0.1}$	$2.7^{+0.3}_{-0.3}$
NGC 5548	*V*	Hβ	4706 - 5041	$4.2^{+0.9}_{-1.3}$	$5.5^{+0.6}_{-0.7}$	$4.7^{+1.8}_{-1.8}$
NGC 6814	*V*	Hβ	4776 - 4936	$6.5^{+0.9}_{-1.0}$	$7.4^{+0.1}_{-0.1}$	$7.3^{+1.2}_{-1.0}$
SBS 1116+583A	*B*	Hβ	4797 - 4926	$2.3^{+0.6}_{-0.5}$	$2.4^{+0.9}_{-0.9}$	$2.0^{+1.1}_{-0.6}$

Table 3.1 Time delays from cross-correlation ($\tau_{\rm CCF}$) are reproduced from Bentz et al. (2010a). Time delays from JAVELIN ($\tau_{\rm JAVELIN}$) are reproduced from Grier et al. (2013a). All time delays are given in the rest frame.

these points. This is similar to what is found in other analyses of the same data (Bentz et al., 2010b; Pancoast et al., 2014b). Such strong variability on short time-scales is in any case not consistent with models where the BLR has only extended emission (see discussion in Section 3.6.1).

The integrated response function for Hβ (Fig. 3.5) has a plateau from 0 days out to about 7 days where it starts to decrease. The shape of the response function is broader than what is found by maximum entropy methods (Bentz et al., 2010b). We find a median Hβ time delay of $\tau_{\rm RLI} = 4.0^{+0.7}_{-0.8}$ days, consistent with results from cross-correlation ($\tau_{\rm CCF} = 4.0^{+0.5}_{-0.7}$ days) and JAVELIN ($\tau_{\rm JAVELIN} = 3.6^{+0.7}_{-0.2}$ days). The integrated response function for Hα (Fig. 3.6) has a flat low response out to about 6 days after which is rises to a peak response at a time delay of around 8 days, and then drops to slightly negative response after 10 days. The time delay for Hα ($\tau_{\rm RLI} = 6.8^{+0.9}_{-1.4}$) is consistent with that from cross correlation ($\tau_{\rm CCF} = 7.8^{+1.0}_{-1.0}$). The integrated response function for Hγ (Fig. 3.7) shows significant response at zero delay with a slight rise to a peak at 3 days after which the response drops to zero beyond 8 days. The time delay from RLI ($\tau_{\rm RLI} = 3.0^{+0.8}_{-0.8}$) is somewhat larger, but consistent with, the result from cross correlation ($\tau_{\rm CCF} = 1.4^{+0.8}_{-0.7}$).

The velocity–delay map for Hβ (Fig. 3.5) shows that the bulk of the response is centred on the emission line with a time delay of about 5 days, similar to the median delay calculated from the integrated response. There seems to be an area of increased response redward of the line centre from $0-1000\,{\rm km/s}$. The velocity–delay map for Hα (Fig. 3.6) shows a strong response around 10 days centred on the emission line and extending to lower time delays. The origin of the prompt response redward of the line centre is unclear. It may be a spurious

feature due to numerical effects, a poorly subtracted continuum (the continuum for Hα was subtracted using a linear fit rather than spectral decomposition as for Hβ, see Section 3.3.2), or perhaps due to residual contamination from [NII], λ6586 Å. We do not find evidence for a blueward plume from 15 to 20 days (not shown) as seen in the maximum entropy maps in Bentz et al. (2010b). The asymmetric shape of the velocity delay map for Hα means that the integrated response function looks rather different from the velocity resolved response functions shown in the right panel in Fig. 3.6. The velocity–delay map for Hγ (Fig. 3.7) shows a broad response with the longest delays at the centre of the line, and progressively decreasing time delays in the wings. We find additional prompt response at the centre of Hγ.

The decrease of the median time delay in Arp 151 from Hα to Hβ and Hγ has been previously observed (Bentz et al. 2010b, see Gaskell 2009 for a review), and may be an effect of the varying optical depth for the Balmer lines. Because the optical depth is larger for the transitions between lower excitation states, Hα photons will have a harder time escaping the BLR without being absorbed. This results in the Hα emission being predominantly directed back towards the ionizing source at the centre, whereas the lines formed by the higher excitation states, Hβ and Hγ, are progressively more isotropic. That is one possible mechanism by which the median time delay can decline in higher excitation emission lines, while all the Balmer lines originate from hydrogen gas located at similar distances from the ionizing source.

Fig. 3.12 shows a comparison between RLI and velocity-resolved cross-correlation time delays by Bentz et al. (2009c) for a number of velocity bins across the Hβ emission line. We find excellent agreement with cross-correlation for all velocity bins and confirm the signature of prompt response redward of the Hβ line centre, while the bulk of the response is at the centre of the emission line at a time delay of around 5 days.

Fig. 3.13 shows velocity–delay maps for Hβ from dynamical modelling, maximum entropy, and RLI. All methods find prompt response in the red wing of the Hβ emission line. This is a characteristic feature of BLR models with free-falling gas or a disk of gas containing a hot spot (see Welsh & Horne, 1991; Bentz et al., 2010b). Some models also produce prompt red-side response for outflowing gas at particular observed orientations (Bottorff et al., 1997). The result from RLI has a stronger response at the line centre, and a weaker prompt response in the red wing compared to dynamical modelling and maximum entropy. In addition RLI finds prompt response at the line centre, which is not seen in the maximum entropy maps. The general resemblance between the velocity–delay maps from RLI and maximum entropy is owing to the fact that the two methods have a common heritage in inversion methods, and both assume some level of smooth response.

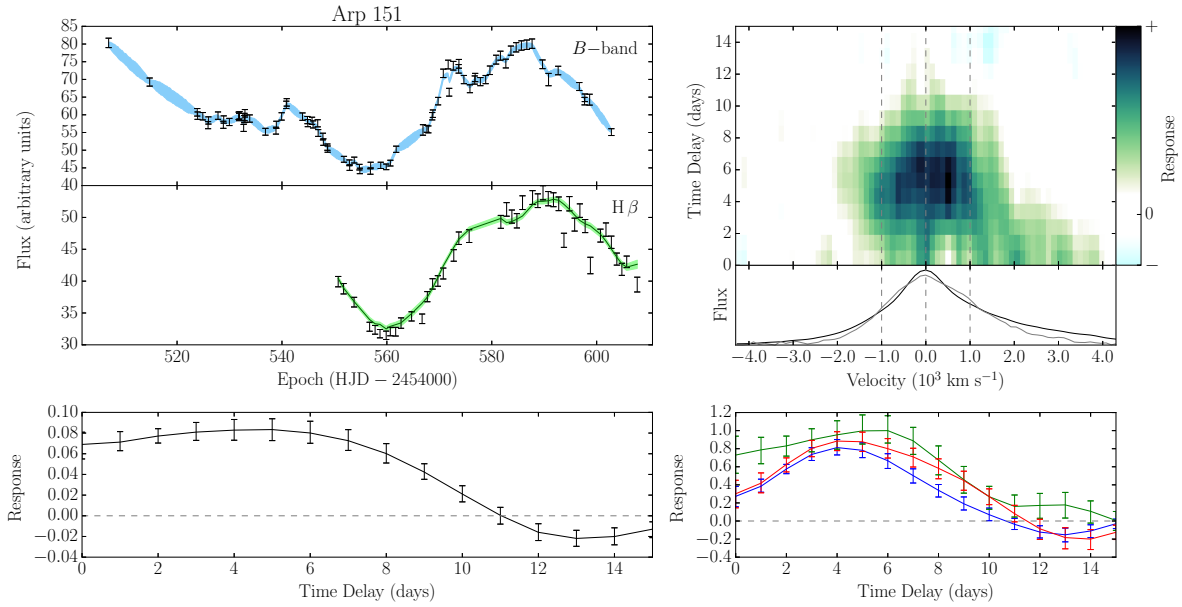

Fig. 3.5 Results from regularized linear inversion of light curves from LAMP 2008 of the Arp 151 Hβ emission line. The left panel shows the continuum (upper left panel, black points) and integrated emission-line light curves (middle left panel, black points) along with the integrated response function (lower left panel, black points). The blue shaded region on top of the continuum light curve shows the median and 1σ percentiles from the Gaussian process realizations used to model the uncertainty in the data. The green line on top of the emission line light curve shows the best fitting result from RLI, with the green shaded band indicating the 1σ percentiles. The horizontal grey dashed line in the lower left panel indicates the location of zero response. The right panel shows the velocity–delay map (upper right panel) calculated by regularized linear inversion of light curves for each wavelength bin individually. Below the velocity–delay map, the mean (black line) and RMS (grey line) spectrum is shown as a function of velocity with respect to the Hβ emission line centre (middle-right panel). Normalized response functions for three velocity bins are shown below the velocity–delay map (lower right panel) with the bins indicated by dashed vertical lines in the velocity–delay map. The colours (blue, green, red) correspond to the Doppler shift with respect to the observer, with blue being negative velocity, green is the central velocity, and red is positive velocity. All time delays in the results figures are in the observed frame.

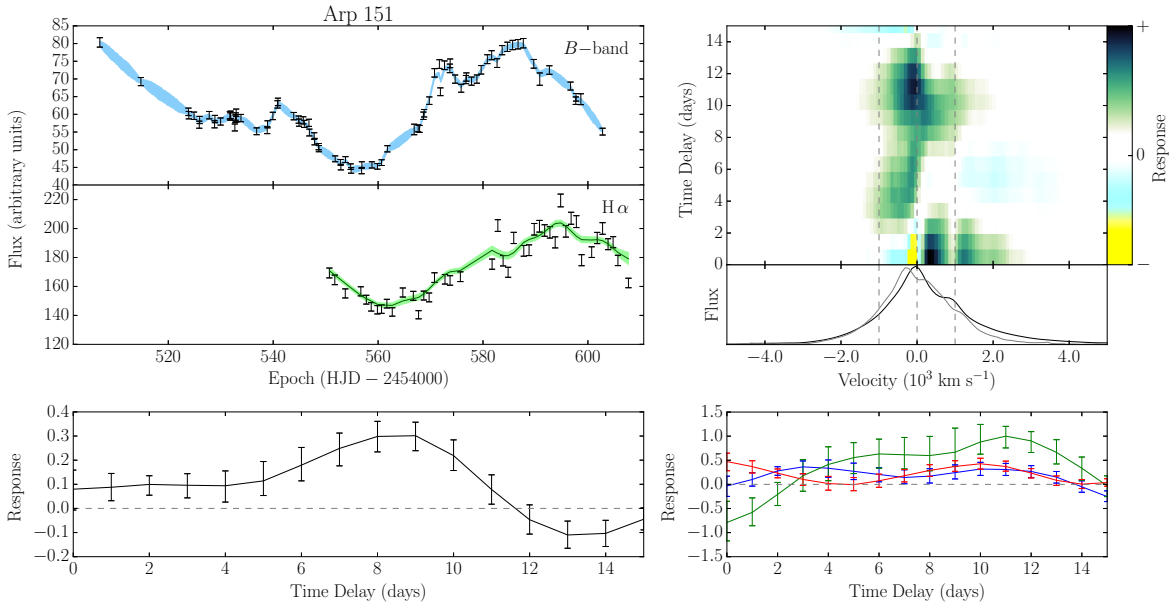

Fig. 3.6 Same as Fig. 3.5 but for Arp 151, Hα.

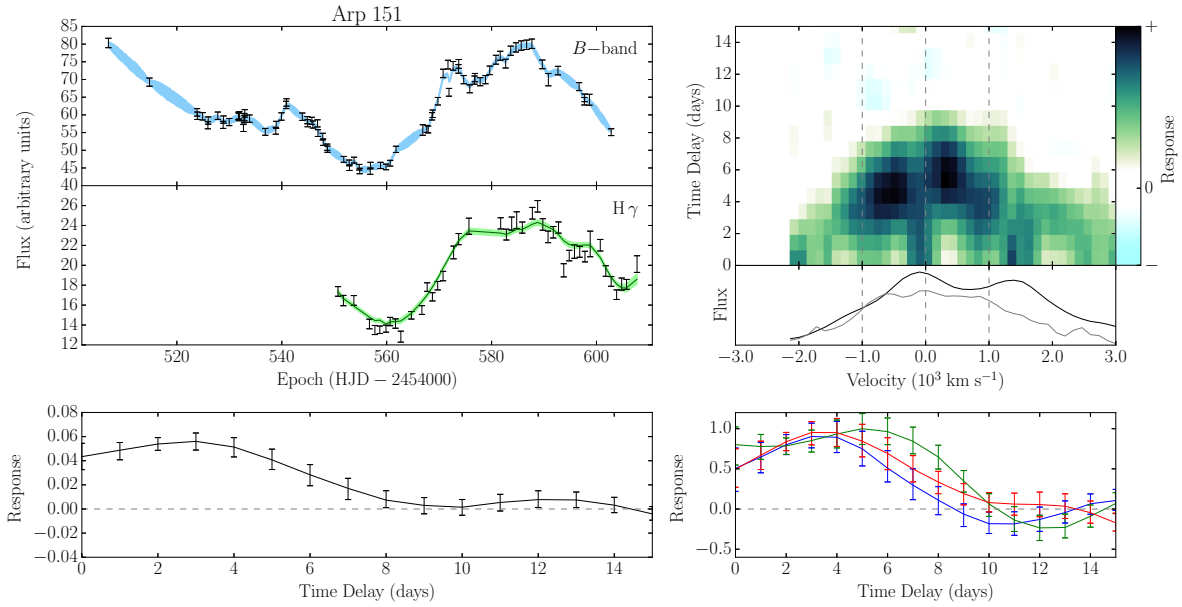

Fig. 3.7 Same as Fig. 3.5 but for Arp 151, Hγ.

Mrk 1310

Results for Mrk 1310 are presented in Fig. 3.8. There is more scatter in the light curves of Mrk 1310 compared to Arp 151. Because of the smoothing constraint, RLI is not able to fit the emission line light curve exactly. This is to be expected, as the method mainly picks up large scale variability to avoid problems with noise on shorter time-scales. The scatter in the Hβ light curve towards the end of the campaign is in any case difficult to reconcile with a simple linear response to the continuum light curve variations near the same epochs.

The integrated response function for Hβ is more peaked than that of Arp 151. The scatter in the derived response functions from our error analysis is also smaller, indicating that the inversion is stable under perturbations in the input light curves. The median time delay of the response function is $\tau_{\rm RLI} = 2.7^{+0.3}_{-0.3}$ days. This delay is slightly shorter than, but consistent with, the cross-correlation result ($\tau_{\rm CCF} = 3.7^{+0.6}_{-0.6}$ days), while the result from JAVELIN ($\tau_{\rm JAVELIN} = 4.2^{+0.9}_{-0.1}$ days) is longer by 1 day compared to the time delay from RLI. The integrated response function dips slightly below zero at longer time delays, which could indicate a negative response in the emission-line, although we do not find this to be significant (see discussion in Section 3.6.4).

The velocity-resolved response map shows a strong response at the line centre with a time delay around 3 days, similar to the integrated time delay. The width of the response is about $\pm 1000\,{\rm km\,s^{-1}}$, similar to Arp 151. The delay is fairly constant across the Hβ line. This result agrees well with velocity-resolved cross-correlation that shows a nearly flat response as a function of velocity, with slightly shorter delays in the wings at $\pm 1000\,{\rm km\,s^{-1}}$ (Fig. 3.12). It is also consistent with dynamical modelling results, with a peak response centred on the emission line at fairly short time delays (Fig. 3.13, middle left panel).

NGC 5548

Results for NGC 5548 are presented in Fig. 3.9. The Hβ light curve of NGC 5548 has more scatter relative to variability amplitude compared to Arp 151 and Mrk 1310. Consequently, RLI has a more difficult time fitting this object.

The integrated response function increases from zero delay up to around 3 days and then has a slowly decreasing plateau out to about 8 days after which it drops off. This yields a median time delay of $\tau_{\rm RLI} = 4.7^{+1.8}_{-1.8}$ days, consistent within 1σ with cross-correlation ($\tau_{\rm CCF} = 4.2^{+0.9}_{-1.3}$ days) and JAVELIN ($\tau_{\rm JAVELIN} = 5.5^{+0.6}_{-0.7}$ days).

The Hβ emission line in NGC 5548 is significantly broader compared to the other objects analysed and the variability across the line shows more irregular structure, as is seen in the velocity-resolved response map in the upper right panel of Fig. 3.9. We find a somewhat

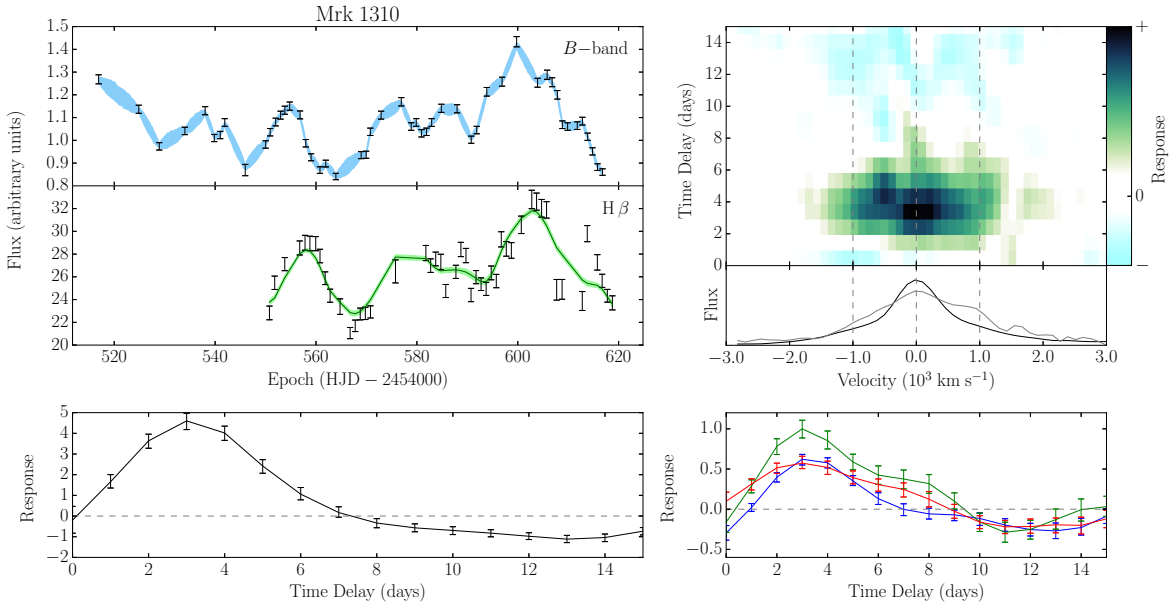

Fig. 3.8 Same as Fig. 3.5 but for Mrk 1310, Hβ.

weak response at the line centre, which peaks at around 5 days. On either side of the line centre at $\pm 5000\,\mathrm{km\,s^{-1}}$ we find stronger isolated response features with peak time delays around 8 days. The velocity-resolved time delays agree well with cross-correlation (Fig. 3.12). Dynamical modelling and RLI both show a level of prompt response in the red wing of Hβ, while the rest of the maps show little similarity (Fig. 3.13).

NGC 6814

Results for NGC 6814 are presented in Fig. 3.10. The light curves of NGC 6814 show an appreciable amount of variability. The continuum V-band light curve has a clear broad peak at HJD $-$ 2454000 $=$ 560 days after which it drops off to a slowly rising plateau that extends to shortly after HJD $-$ 2454000 $=$ 600 days. The emission line light curve has the same over-all trend as the continuum, but instead of having a plateau after the initial peak, it rises to almost the same level as the initial peak. Because of this, RLI has a difficult time matching the first and second peaks in the emission line light curve, explaining why the fit is underestimated for the second peak.

The integrated response function peaks around 8 days and has broad flat wings to either side (Fig. 3.10, lower left panel). The median time delay of $\tau_{\mathrm{RLI}} = 7.3^{+1.2}_{-1.0}$ days is consistent with results from cross-correlation ($\tau_{\mathrm{CCF}} = 6.5^{+0.9}_{-1.0}$ days) and JAVELIN ($\tau_{\mathrm{JAVELIN}} = 7.4^{+0.1}_{-0.1}$ days).

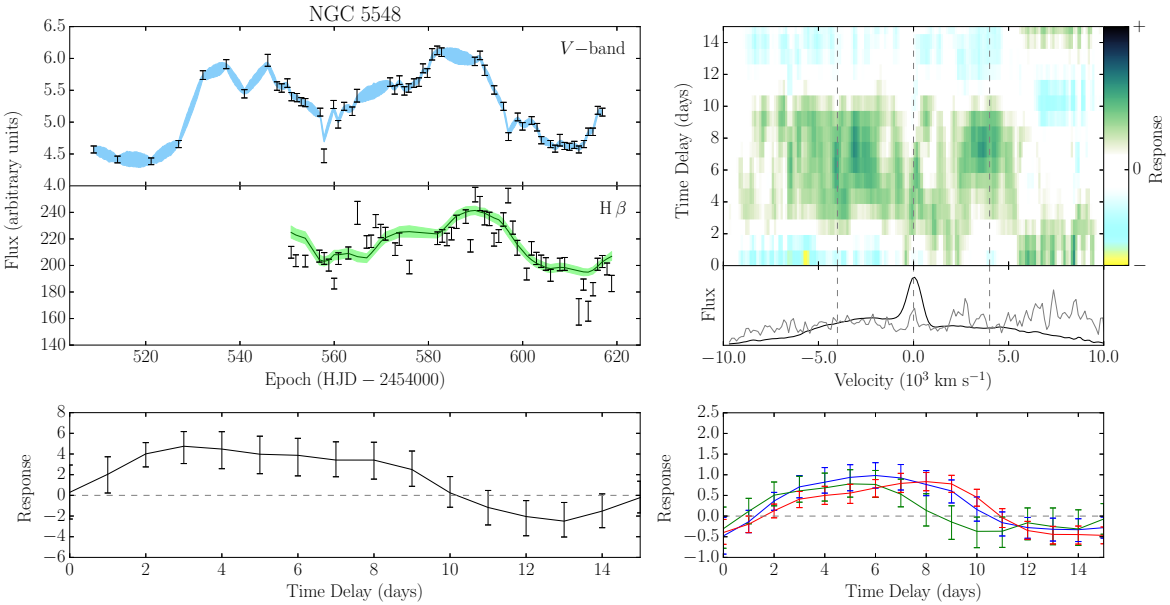

Fig. 3.9 Same as Fig. 3.5 but for NGC 5548, Hβ.

The velocity-resolved response map for NGC 6814 shows a clear isolated response peak centred on the Hβ emission line (Fig. 3.10, upper right panel). There is a somewhat peculiar dip in the response map just blueward ($\sim -100\,\mathrm{km\,s^{-1}}$) of the line centre. Further away at around $\pm 500\,\mathrm{km\,s^{-1}}$ the response peaks on either side of the line centre and then drops off to zero beyond $\pm 1500\,\mathrm{km\,s^{-1}}$. The velocity-resolved time delays agree well with cross-correlation at centre of the Hβ line (Fig. 3.12). At lower velocities we find a slightly longer time delay compared to the cross-correlation result. At higher velocities, blueward of the line, RLI was unable to recover a time delay due to a lack of emission line response. Looking at the fully resolved response map from RLI in Fig. 3.10 we see that RLI calculates little response in the wings beyond $\pm 1500\,\mathrm{km\,s^{-1}}$, which might explain the discrepancy with the cross-correlation results. Dynamical modelling of NGC 6814 tends to prefer shorter time delays than what is found using other methods (see Fig. 3.13). The highest velocity bin failed to produce a time delay estimate due to a noisy response function.

SBS 1116+583A

Results for SBS 1116+583A are presented in Fig. 3.11. The emission line light curve of SBS 1116+583A lacks significant features above the noise level. As a result the RLI fit does not match the emission line light curve well. The results for this object, including the velocity–delay map, should thus be interpreted with caution.

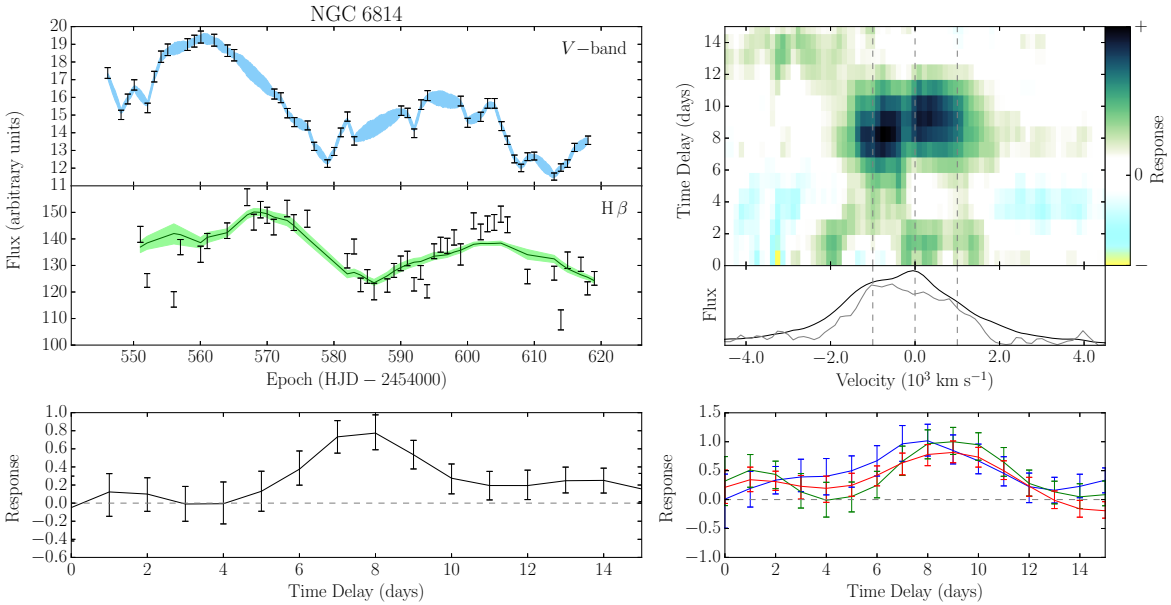

Fig. 3.10 Same as Fig. 3.5 but for NGC 6814, Hβ.

The integrated response function prefers a relatively short time delay of $\tau_{\rm RLI} = 2.0^{+1.1}_{-0.6}$ days, which is slightly shorter, but fully consistent with cross-correlation ($\tau_{\rm CCF} = 2.3^{+0.6}_{-0.5}$ days) and JAVELIN ($\tau_{\rm JAVELIN} = 2.4^{+0.9}_{-0.9}$ days).

The velocity-resolved response map for SBS 1116+583A (Fig. 3.11) shows a multimodal response map with a broad response component at short time delays, around 2 days, and an additional isolated response at 10 days at the centre of the Hβ line. This is a good example of the flexibility of RLI to reconstruct complicated velocity–delay maps. The velocity–delay map shows some resemblance to models in which the BLR is confined to an isotropically illuminated disk (see Fig. 5 in Bentz et al., 2010b).

It is not very meaningful to calculate a single time delay from a multimodal response function, even so we apply the same procedure for determining the time delay as for the previous objects (see Section 3.5.1). The resulting velocity-resolved time delays agree well with cross-correlation, showing longer time delays at the centre of the emission line and shorter time delays in the wings (Fig. 3.12). We note that the time delay calculated close to the Hβ line centre fall between the two modes in the response map, and is thus not well constrained. We include these time delays for comparison with the velocity-resolved cross-correlation, but they should be interpreted with caution, as suggested by the large error-bars. The lowest velocity bin failed to produce a time delay estimate due to a noisy response function.

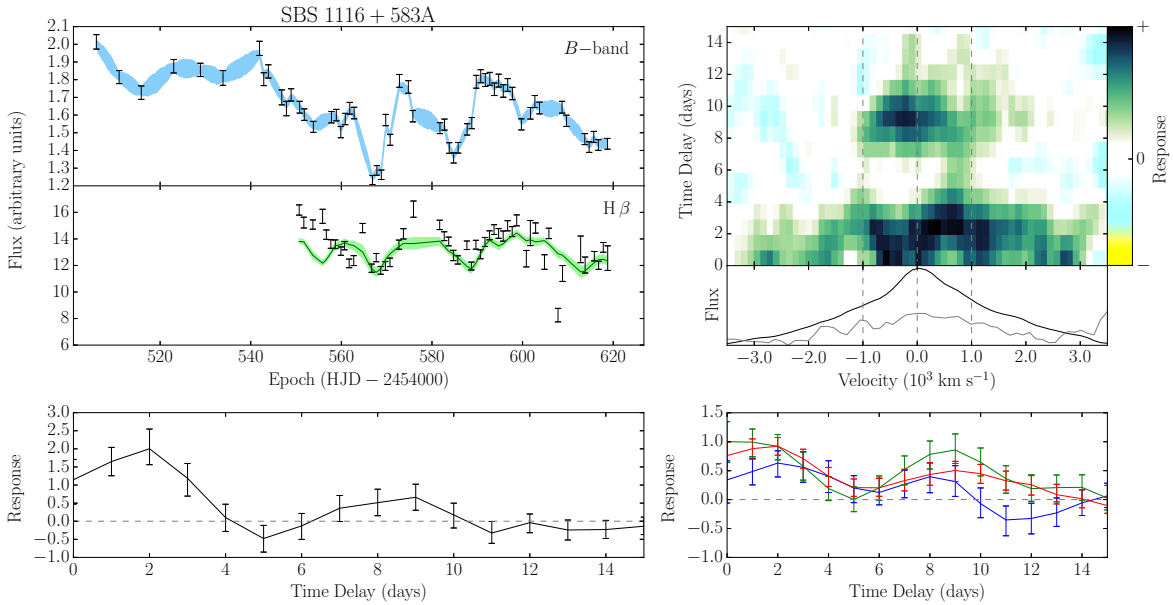

Fig. 3.11 Same as Fig. 3.5 but for SBS 1116+583A, Hβ.

The results for SBS 1116+583A from RLI are in general agreement with dynamical modelling, although dynamical modelling does not reproduce the same strong response at $\tau = 10$ days and generally prefers shorter time delays at the line centre (see Fig. 3.13).

3.6 Discussion

3.6.1 Assumption of a constant linear response

Long temporal baseline multi-epoch observations of AGN reveal significant changes in the broad emission line equivalent widths (e.g. Kinney et al., 1990; Pogge & Peterson, 1992; Gilbert & Peterson, 2003; Goad et al., 2004) and line profiles (e.g. Wanders & Peterson, 1996; Sergeev et al., 2001, 2007) on time-scales of months to years. These effects could possibly account for some of the discrepancies found when matching longer time-scale variability patterns using linear reverberation mapping, such as the inability of RLI to match the second peak in the emission line light curve in NGC 6814 (Fig. 3.10).

In addition to long time-scale non-linearities, some light curves of the LAMP 2008 dataset show high-variability features (e.g. late epochs in Mrk 1310, Fig. 3.8). If these features are associated with the BLR, they are inconsistent with models in which the BLR emission comes from an extended region. This remains true even after exclusion of potentially unreliable spectra in the LAMP 2008 dataset, as described in section 3.3.2. Whether these outliers are

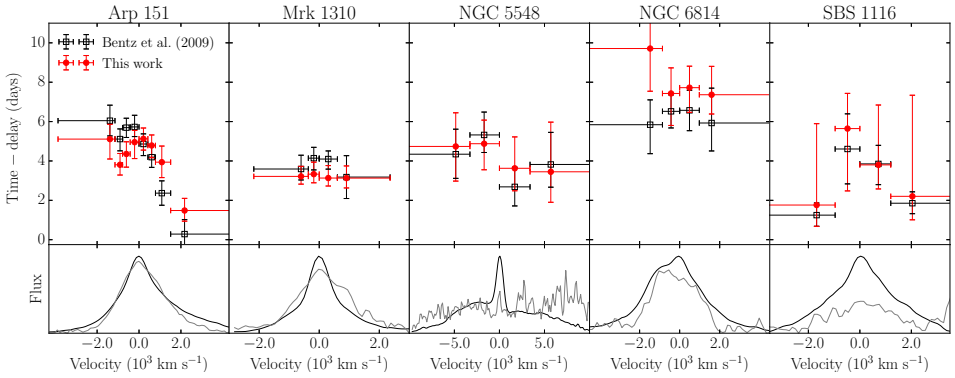

Fig. 3.12 Comparison of Hβ time delays from regularized linear inversion with cross-correlation results from Bentz et al. (2009c). The upper panels show time delays as a function of velocity with respect to the Hβ emission line centre. Red filled circles with error bars show time delays from this paper. Black open squares with error bars are from Bentz et al. (2009c). Light curves are obtained by integrating the emission in each velocity bin indicated by the horizontal error-bars. The time delays from RLI are calculated as the median of the positive part of the response (see Section 3.5.1). The lower panels show the mean (black) and RMS (grey) spectra. All time delays in this figure are in the observed frame.

due to systematic measurement uncertainties affecting individual epochs, an indication of unknown processes in the BLR, or a combination of these, is unclear.

Whatever the origin of non-linear features in the emission line light curves, current reverberation mapping techniques, such as cross-correlation, maximum entropy, and RLI, will be insufficient to describe them. Even so these methods remain valuable tools for testing models of the BLR and investigate departures from linearity in AGN light curves. Implementation of photoionization physics into dynamical modelling codes may be a way to probe non-linear processes in the BLR.

3.6.2 Ionizing versus observed continuum

Studies suggest a non-negligible time delay between the ionizing UV continuum and the optical continuum on the order of 1 day in NGC 7469 and NGC 5548 (e.g. Collier et al., 1998; McHardy et al., 2014; Edelson et al., 2015). This means that the V and B band continuum light curves originate from a region comparable in size to some of the shorter time delays found for Balmer emission lines. This extended continuum emission region will introduce geometric smoothing in the optical continuum light curves used for reverberation mapping. If the delay between the ionizing continuum and the measured optical continuum is constant on time-scales of reverberation mapping campaigns, linear reverberation methods can still be applied, but the interpretation of the response functions will have to be revised to include

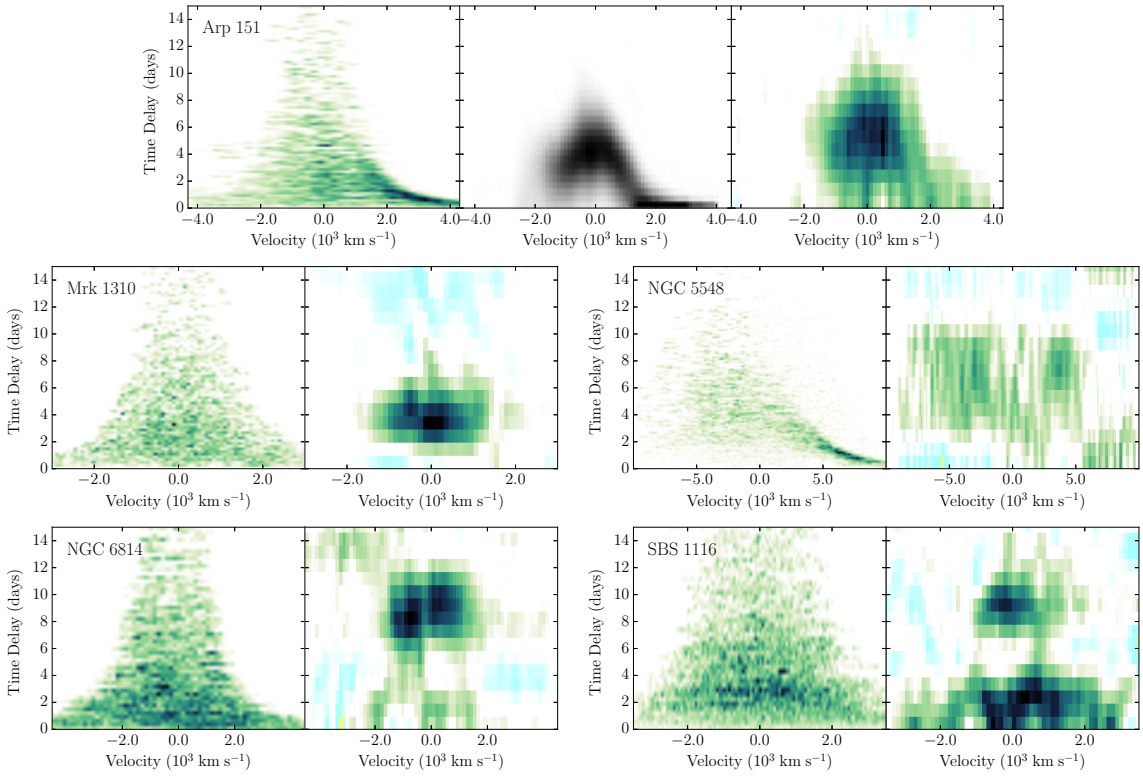

Fig. 3.13 Comparison of velocity–delay maps from regularized linear inversion (left panels for each object) to results from dynamical modelling (right panels for each object) for all objects (Pancoast et al., 2014b). For Arp 151 we additionally include results from the maximum entropy method (middle panel for Arp 151), which only has results for this object (Bentz et al., 2010b). All three methods used the same dataset from LAMP 2008 (see Section 3.3). Regularized linear inversion and dynamical modelling used spectral decomposition for continuum subtraction, while the maximum likelihood analysis used a linear fit to remove the continuum level below the line.

not just the geometry of the BLR, but also the geometry of the extended optical continuum emission region. It will be interesting to extend this analysis in the future by performing RLI of optical emission line variability as driven by UV continuum to assess the magnitude of these systematic effects.

3.6.3 Response function errors

The smoothing condition used to regularize the inversion problem introduces correlations in the response functions by linking nearby points through the first-order derivative. This correlation is an implicit assumption of the method and it reflects our belief that the emission line light curve is produced by a superposition of photons emitted from a fairly homogeneous distribution of gas in the BLR. The error bars on the response functions should thus not be interpreted as errors on the individual points of the response function, but rather as an indication of the range of solutions we get by re-interpolating the continuum light curve and re-sampling the emission line light curve.

In our current implementation of RLI no correlation in response is imposed between response velocity bins. This can be witnessed by the vertical streaks in the presented response maps. Not imposing a correlation has the advantage that any correlation between velocity-bins in the final response maps must be driven by the data, or at least systematic effects correlated with the emission lines. It seems natural to assume that the BLR emissivity is correlated in position as well as velocity space, motivating a smoothing constraint in the velocity domain, as is also assumed in dynamical modelling and maximum entropy methods. Because we found the velocity-bins to be naturally correlated in the response maps, and in order to keep the method fast and simple, we decided not to impose any smoothing in the velocity-domain.

3.6.4 Negative response values

Some models suggest that negative values occur naturally in AGN response functions (Sparke, 1993; Goad et al., 1993; Goad & Korista, 2014), and negative response values have recently been observed in X-rays (McHardy et al., 2007; Fabian et al., 2009). Negative response can arise in different ways, such as if an increase in ionizing flux causes part of the responding gas to become fully ionized, or if the BLR structure changes on a dynamical time-scale, such as if the continuum decreases while new material falls into the BLR. Note that in both of these examples the BLR structure changes on time-scales of the same order as the time delay. This means that the assumption of a constant linear response breaks down and more general

methods, such as dynamical modelling, are required to account for the time varying part of the response.

An advantage of RLI over other reverberation mapping methods, is that it does not require the response function to be everywhere positive. We find some preference for negative response in some of the objects analysed (e.g. Mrk 1310, Fig. 3.8). While none of the response functions show strong evidence for negative response these results may be an indication that more complicated processes are taking place in the BLR, than what can be contained in a simple constant linear response model. However, negative values occur naturally as artefacts when linear inversion methods are applied to discrete and noisy data, even if the true response is everywhere positive. This is somewhat in analogy to aliasing distortions when dealing with discrete Fourier transforms. These artefacts are seen as ringing effects, such as observed in the inversion of the simulated 1D data (see Fig. 3.2). It is not possible to impose positivity while keeping an analytical expression for the response function (Vio et al., 1994), and since simplicity and flexibility were the main motivations for using RLI, we leave the positivity constraint to other methods such as maximum entropy and dynamical modelling. With these considerations in mind we emphasize that all the negative response values found in our analysis of the LAMP 2008 data are of low statistical significance. In particular, the integrals of the response functions are positive for all objects analysed.

3.7 Summary and conclusion

Building on previous work by Krolik & Done (1995), we develop a new method for reverberation mapping based on regularized linear inversion that includes statistical modelling of the AGN continuum light curves. In this implementation, response function errors are evaluated using a combination of Gaussian process fitting of the continuum light curves as well as bootstrap resampling of the emission line light curves. Regularized linear inversion has the advantage over other reverberation mapping methods that it makes few assumptions about the shape of the response function, and it allows for negative values in the response function. In addition, because the method is based on an analytical solution to the transfer equation, it is very computationally efficient. The scale of regularization is a function of the data only, such that no user-input is required, except for the time baseline of the analysis. This means that flexible response functions can be calculated quickly and consistently.

We test the method on simulated data and show that it is able to recover unimodal and multimodal response functions as well as response functions with negative values (see Fig.

3.2). We further test the method on data simulated using dynamical modelling and show that it is able to recover 2-dimensional velocity–delay maps (see Fig. 3.3).

We apply RLI to light curves of five nearby Seyfert 1 galaxies, taken by the LAMP 2008 collaboration, and present time delays, integrated response functions and velocity–delay maps for the Hβ line in all objects, as well as Hα and Hγ for Arp 151. This is the first time a reverberation mapping method allowing for negative response has been applied to a large dataset. Our results are in good agreement with previous studies based on cross-correlation and dynamical modelling, offering a powerful corroboration of the assumptions underlying these reverberation mapping methods.

The main physical results of this work can be summarized as follows:

1. Despite using a very different method for calculating time delays we find that our results are in good agreement with results from cross correlation.

2. We find asymmetric response of the Hβ emission line in Arp 151, with prompt response in the red wing of the emission line, consistent with models that include bulk gas flows in the BLR.

3. We confirm previous studies finding that lines originating from high excitation states, such as Hγ, have shorter time delays compared to lines originating from lower excitation states, such as Hα and Hβ.

4. While some objects, such as Arp 151 and Mrk 1310, show a degree of negative response at longer time delays, we find no conclusive evidence for negative response values in any of the objects.

5. The absence of strong response at zero delay for Hβ in all objects except NGC 5548, suggests a lack of broad line emission along the line of sight. This could be explained by anisotropic line emission (Ferland et al., 1992), or by confinement of the BLR gas in a disk-like structure observed face-on.

This work demonstrates that regularized linear inversion is a valuable tool for reverberation mapping and a worthwhile complementary method for analysing high quality reverberation mapping datasets. The recent multi-wavelength reverberation mapping campaign of NGC 5548 (De Rosa et al., 2015; Edelson et al., 2015), including simultaneous ground-based monitoring in the optical and spectroscopy in the ultraviolet with the Cosmic Origins Spectrograph on the *Hubble Space Telescope*, will provide exceptionally high quality data and thereby a great opportunity to test the RLI method and its underlying assumptions.

3.8 Acknowledgements

We thank the referee, Rick Edelson, for comments and suggestions that led to substantial improvements of the manuscript. We are grateful to Julian Krolik, Mike Goad, Kirk Korista and Brendon Brewer for enlightening input, as well as Anthea King and Darach Watson for discussions leading to the improvement of this work. The Dark Cosmology Centre (DARK) is funded by the Danish National Research Foundation. AP acknowledges support from the NSF through the Graduate Research Fellowship Program and from the University of California Santa Barbara through a Dean's Fellowship. TT acknowledges support from the Packard foundation in the form of a Packard Fellowship. TT thanks the American Academy in Rome and the Observatory of Monteporzio Catone for their kind hospitality during the writing of this manuscript. Research by TT is supported by NSF grant AST-1412693 (New Frontiers in Reverberation Mapping). DP acknowledges support through the EACOA Fellowship from The East Asian Core Observatories Association, which consists of the National Astronomical Observatories, Chinese Academy of Science (NAOC), the National Astronomical Observatory of Japan (NAOJ), Korean Astronomy and Space Science Institute (KASI), and Academia Sinica Institute of Astronomy and Astrophysics (ASIAA). Research by AJB is supported by NSF grants AST-1108835 and AST-1412693. Research by MCB is supported by NSF CAREER grant AST-1253702. This work makes use of the Lick AGN Monitoring Project 2008 dataset supported by NSF grants AST-0548198 (UC Irvine), AST-0607485 and AST-0908886 (UC Berkeley), AST-0642621 (UC Santa Barbara), and AST-0507450 (UC Riverside). This work makes use of the EIGEN header library (Guennebaud et al., 2010). All figures are produced in MATPLOTLIB (Hunter, 2007).

Chapter 4

Photometric reverberation mapping

This chapter contains the paper:

"Narrow band photometric reverberation mapping of three nearby active galactic nuclei: NGC 3227, NGC 4051 and NGC 4151"

Skielboe, A., Watson, D., Krogager, JK., et al. 2016, to be submitted

4.1 Abstract

Reverberation mapping of active galactic nuclei (AGN) enables estimates of the sizes of the broad emission line regions (BLR), by determining the time delay between broad emission line flux and continuum flux variations. Photometric reverberation mapping achieves this uses only imaging, which is generally cheaper than spectroscopic monitoring. To assess the feasibility of obtaining accurate time delays by purely photometric means, we observe three nearby AGN in the V, B and *hbw* bands, and derive photometric time delays using the JAVELIN reverberation mapping code. We present photometric light curves and narrowband photometric reverberation mapping results for three nearby AGN: NGC 3227, NGC 4051 and NGC 4151, and determine their broad Hβ line time-delays compared to the V band continuum. We find time-delays of $5.9^{+2.0}_{-1.9}$ days for NGC 3227, $6.0^{+4.6}_{-3.6}$ days for NGC 4051, and $11.7^{+2.7}_{-3.0}$ days for NGC 4151. We also measure the absolute luminosities for these AGN and add these new measurements to the Hβ radius-luminosity relation for AGN. The results are in good agreement with previous studies, and suggest that AGN broad emission line time delays can be obtained using narrowband photometry and short exposures on smaller telescopes.

4.2 Introduction

Active galactic nuclei (AGN) are the most persistently luminous objects in the universe, with bolometric energy outputs of the order 10^{45} erg s^{-1}, spanning the entire electromagnetic spectrum (Kormendy & Richstone, 1995; Vanden Berk et al., 2001; Woo & Urry, 2002; Ferrarese & Ford, 2005). Properties of AGN have been found to correlate with large scale properties of their host galaxies, indicating a link between AGN activity and galaxy evolution (for reviews see Fabian, 2012; Kormendy & Ho, 2013; Heckman & Best, 2014). The luminosities of AGN also make them ideal objects for studying the early universe (e.g. Jiang et al., 2007; Scoville et al., 2007; Erb, 2015), and probing supermassive black hole evolution (Kelly & Merloni, 2012). To better understand the origin of AGN scaling relations it is helpful to study the structure and emission mechanism of AGN themselves.

Reverberation mapping constrains the structure of the broad emission line region (BLR) in AGN by measuring the light travel time between variations in the continuum flux and flux in the broad emission lines. The light travel time, or time delay, can be interpreted as a measure of the physical size of the BLR. Assuming that the BLR emitters are virialized (Peterson & Wandel, 2000; Onken et al., 2004; Nelson et al., 2004), the size of the BLR, together with the velocity of the broad line region gas, can be combined to constrain the supermassive black hole mass (Peterson et al., 1998a; Kaspi et al., 2000). Locally measured scaling relations based on black hole mass can then be used to constrain AGN demographics to high redshifts (Vestergaard, 2011). Velocity resolved reverberation mapping, that measures time delays as a function of wavelength across the emission line, provides constraints on the geometrical and kinematic structure of the BLR (Welsh & Horne, 1991; Bentz et al., 2010b; Grier et al., 2013b; Pancoast et al., 2014b; Skielboe et al., 2015). Reverberation mapping of different continuum bands can furthermore put constraints on the accretion disk (Edelson et al., 2015).

The kinematics of the BLR can be used to measure the mass of the supermassive black hole, which yields insights into large scale structure formation and galaxy evolution (for a review see Kormendy & Ho, 2013). The BLR radius in itself can also be combined with photoionization models (Horne et al., 2003), to determine independent and absolute distances to AGN (Hönig et al., 2014, use reverberation mapping of the dust torus together with an interferometric size measurement to determine absolute distances), providing a single step directly into the Hubble flow, avoiding the need for the distance ladder for cosmology. In addition, relative methods based on the correlation between the BLR time delay and the intrinsic UV/optical luminosity of the AGN (Kaspi et al., 2000, 2005; Bentz et al., 2009a, 2013) may have the potential to provide competitive cosmological model constraints (Watson et al., 2011).

To study the evolution of supermassive black hole masses over cosmic time, observations outside the local universe are required. Traditional reverberation mapping at high redshift is unfeasible due to the expensive observation campaigns required for single slit spectroscopy of a large number of AGN. Instead, scaling relations can be used to relate properties of the AGN to determine black hole masses from single epoch spectra (Wandel et al., 1999; McLure & Jarvis, 2002; Vestergaard, 2002; Vestergaard & Peterson, 2006). This work has lead to a significant improvements in our understanding of AGN demographics over cosmological distances (e.g. Vestergaard, 2004; Shen et al., 2011), but depend on our understanding of the systematic uncertainties in the scaling relations applied (Kilerci Eser et al., 2015).

To complement single epoch measurements, new reverberation mapping surveys have been proposed. These surveys attempt to study large samples of AGN, at a range of redshifts, to measure their properties, constrain scaling relations, and relate them to AGN galaxy evolution (King et al., 2014, 2015; Shen et al., 2015). Additionally, these and future AGN surveys that measure the radius of the BLR, can be used to extend the radius luminosity relation to higher redshift, and by doing so open the possibility of probing cosmological models using only AGN measurements. A downside of these surveys are that they rely on multi-object spectroscopy, to separate the continuum and line emissions for high-precision reverberation mapping. Multi object spectroscopy complicates flux calibration and lowers the photon efficiency, making these types of campaigns rather expensive in terms of observation time.

Another possibility for high efficiency reverberation mapping is to use photometric observations to measure an average time delay for a given emission line. This has the advantage that observations can be done faster and without spectral flux and wavelength calibrations. In addition, just as the more advanced multi object spectrographs, photometric reverberation mapping allows several AGN to be observed simultaneously, thereby reducing the required observing time significantly. Photometric reverberation mapping has been used to successfully measure time delays in AGN using broad band (Chelouche & Daniel, 2012; Chelouche et al., 2012; Edri et al., 2012) and narrow band (Haas et al., 2011; Pozo Nuñez et al., 2012, 2013, 2015) photometric observations.

Photometric reverberation mapping has yet to be proven as a viable alternative to spectroscopic reverberation mapping. In order to assess the feasibility of using purely, or mostly, photometric observations to derive accurate time delays for a large number of AGN, the method must be tested under varying observational conditions, for a number of different objects. Combined with previous results from spectroscopic campaigns, this will help inform us whether the method is a viable technique for measuring BLR time delays.

Here we report results from a 3.5 month photometric reverberation mapping campaign using the *STELLA* Robotic Observatory on Tenerife (Strassmeier et al., 2001, 2004). We observed three nearby Seyfert 1 galaxies, NGC 3227, NGC 4051 and NGC 4151 in three bands: Johnson-Cousins V, B and Hβ wide (hbw) (FWHM 13 nm). We estimate the Hβ BLR time delays in each object using the JAVELIN method for narrow band photometric reverberation mapping (Zu et al., 2011, 2016). We estimate intrinsic AGN luminosities and add the objects to the radius luminosity relation (Bentz et al., 2013) for AGN.

All errors listed in tables and shown in figures are $1-\sigma$ (~ 68 %) percentile uncertainties. To calculate intrinsic luminosities, we use a flat ΛCDM cosmological model with $\Omega_\Lambda = 67.7$.

4.3 Data

4.3.1 Imaging

We monitored NGC 3227, NGC 4051 and NGC 4151 every few nights over 3.5 months using the Wide-Field STELLA Imaging Photometer (WiFSIP) on the 1.2 m *STELLA* Robotic Observatory on Tenerife (Strassmeier et al., 2001, 2004). The final dataset includes 79 epochs for NGC 4051 and NGC 4151 and 68 epochs for NGC 3227. Each epoch includes imaging in three bands: Johnson-Cousins V and B, as well as Hβ wide (hbw, FWHM 13 nm). Because of technical issues we did not obtain the scheduled number of B band images required for reverberation mapping. For this reason, we were able to get results only using the V band and *hbw* band. The images have been automatically reduced using the *STELLA* data reduction pipeline, including bias subtraction and flat-fielding (see Strassmeier et al. (2004)).

Figure 4.1 shows single-epoch V band image cutouts of the three objects. About 10 % of the observations had to be discarded due to bad weather, and a further ~ 10 % were discarded due to asymmetric point spread functions (PSFs) because of high winds at the observatory site (see Section 4.3.2 below).

4.3.2 PSF asymmetries

Most of the images obtained in our campaign have symmetric PSFs, but a number of epochs were affected by high winds and significant cloud cover at the observing site. The affected epochs show significantly blurred or asymmetric point spread functions (see Fig. 4.2 for examples). These asymmetric PSFs were not due inherent issues with the telescope optics, or bad seeing, but rather due to the small size of the telescope enclosure, which makes it susceptible to wind shake. During the observing campaign unusually high wind speeds, in

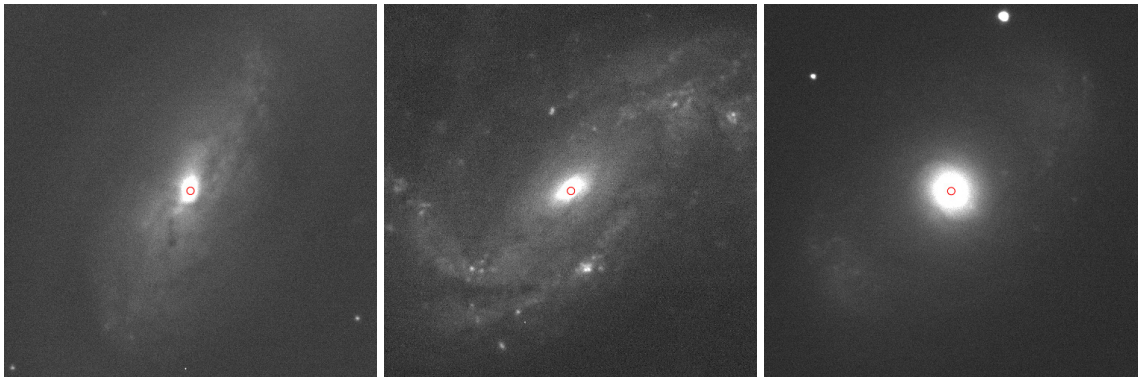

(a) NGC 3227 (b) NGC 4051 (c) NGC 4151

Fig. 4.1 Single-epoch *V* band image cutouts of the three AGN targets. The red circles indicate the aperture of 5 pixels used for photometry.

excess of 20 m/s, were measured at the site[1], resulting in some of the highly asymmetric PSFs seen in Fig. 4.2.

The effects of asymmetric PSFs on the estimated flux are somewhat mitigated by the kernel convolution procedure described in Section 4.3.4. For images with large visible PSF asymmetries, the kernel convolution often fails and instead produces visible artifacts on the convolved images. All convolved images were manually inspected (see Fig. 4.2 for examples), and any image with asymmetric PSFs or other artifacts were excluded from the photometric light curves.

4.3.3 Spectra

In addition to imaging, we obtained spectra from the ALFOSC spectrograph at the Nordic Optical Telescope during a number of epochs distributed over the monitoring campaign. The spectra were observed with grism 7, which covers wavelengths from 3850 to 6850 Å with a resolution of about $R = 100$. The observations were carried out using a 10-arcsec wide slit and integration times of 60 seconds. The wide slit was chosen to ensure high signal-to-noise even under poor seeing conditions. The spectra were processed using standard IRAF[2] routines for long-slit spectroscopy. The flux calibration was performed using a spectro-photometric standard star (HD 93521) observed during the same night as the science exposures, and

[1] See *STELLA* environmental status and historical data at http://stella.aip.de/stella/status/status.php.

[2] IRAF is distributed by the National Optical Astronomy Observatory, which is operated by the Association of Universities for Research in Astronomy (AURA) under cooperative agreement with the National Science Foundation.

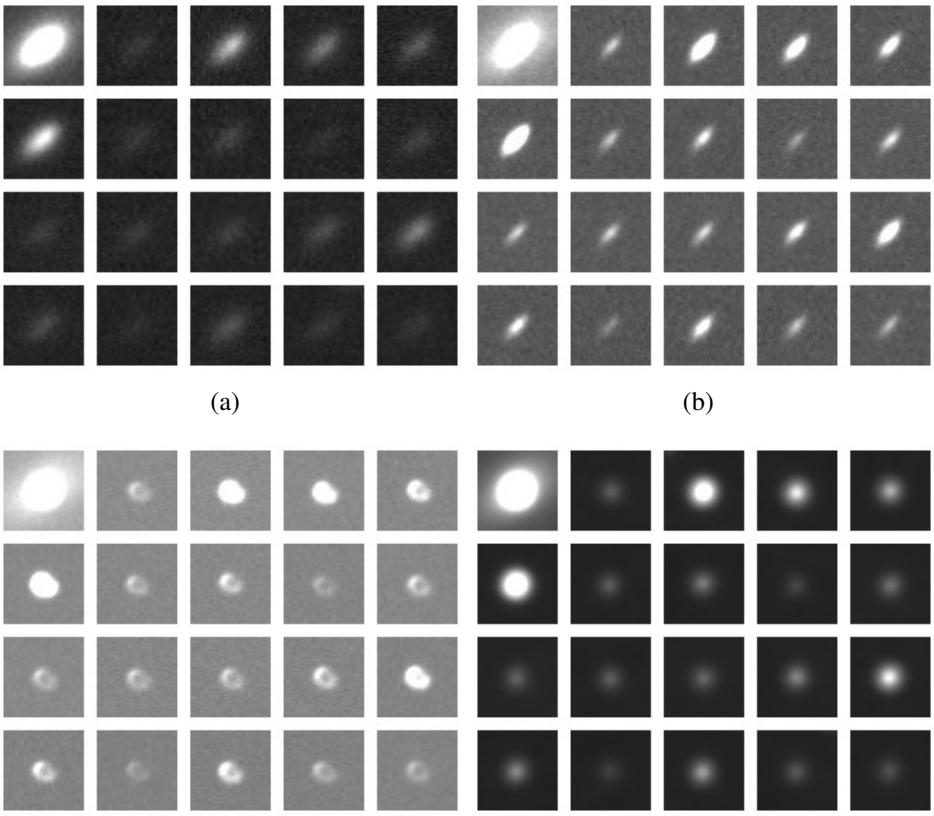

Fig. 4.2 Single-epoch *V* band image cutouts of the nucleus (top left cutout in each panel) of NGC 4051 and stars in the field (all other cutouts). The figure illustrates the range of PSF shapes encountered in the *STELLA* observing campaign. Panel a and b showns asymmetric PSFs due to high winds at the observing site (see Section 4.3.2). Panel c shows an example where the PSF convolution has failed. Panel d shows a circular symmetric PSF which indicates a successful convolution. Of the four epochs shown here only the last epoch (panel d) was included in the final analysis.

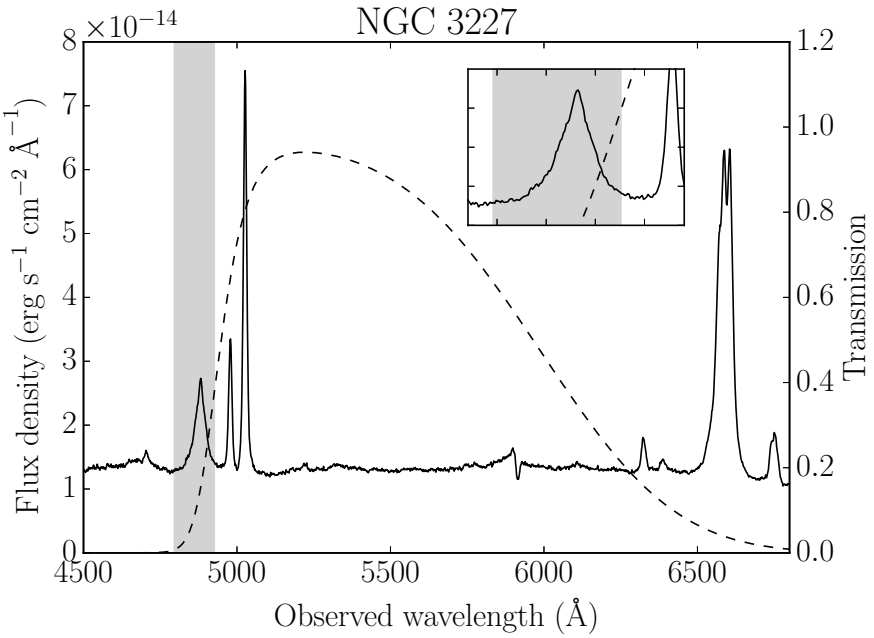

Fig. 4.3 Spectrum of NGC 3227. The solid band indicates the location of the *hbw* band, while the *V* band filter transmission curve is plotted as a dashed line. The inset shows a zoom-in at the location of the Hβ line.

corrected for differences in airmass. The extracted 1-dimensional spectra were subsequently corrected for galactic extinction using the maps of Schlafly & Finkbeiner (2011).

The spectra allow us to evaluate the filter coverage in relation to the Hβ line shape. The spectra and filter coverages are shown in Fig. 4.3 to 4.5. In all objects the *hbw* band filter covers the bulk of the Hβ emission line. The *V* band includes mainly continuum emission, as well as a contribution from constant [OIII] narrow lines and a small percentage of Hβ variable emission.

4.3.4 Light curves

We construct photometric light curves in all bands using aperture photometry. The variation in seeing is eliminated by convolving all images using a point spread function (PSF) fit to the image that has the largest seeing, such that all the images have the same approximate PSF. This controlled degradation of the images ensures accurate relative fluxes derived from aperture photometry. The resulting images are manually inspected and any image showing asymmetric PSFs or other artifacts are discarded before further analysis (see Fig. 4.2). We apply standard aperture photometry on the remaining images, using a fixed aperture of 5

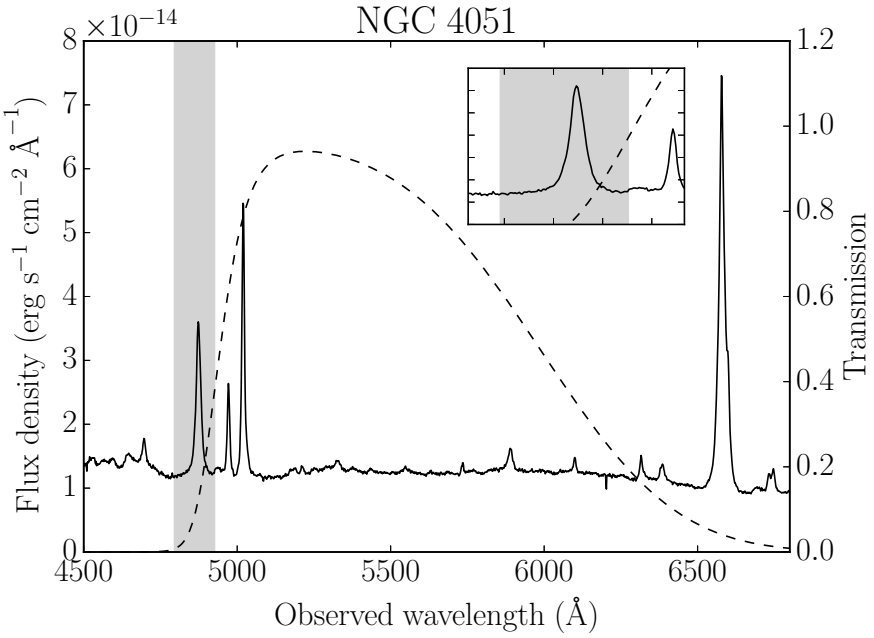

Fig. 4.4 Same as figure 4.3 but for NGC 4051.

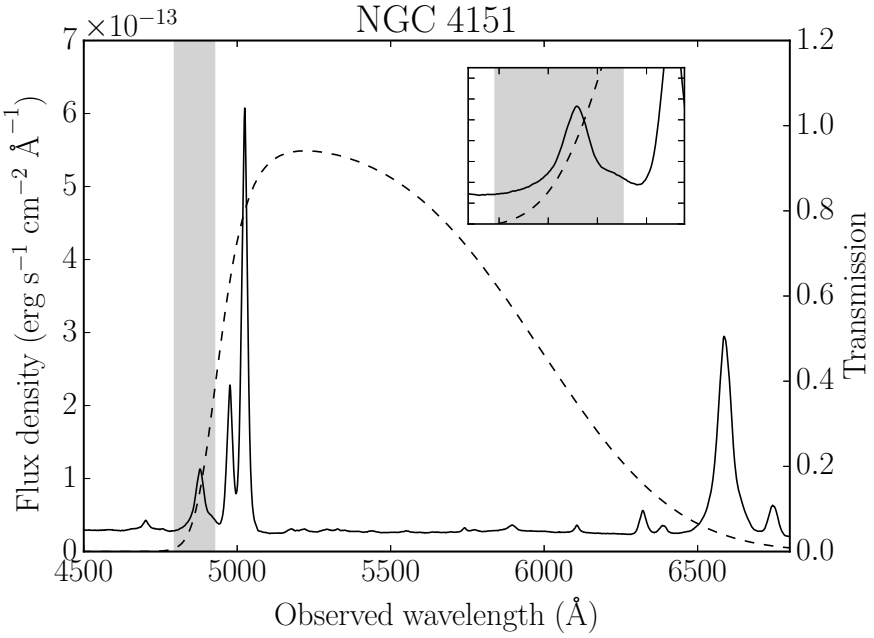

Fig. 4.5 Same as figure 4.3 but for NGC 4151.

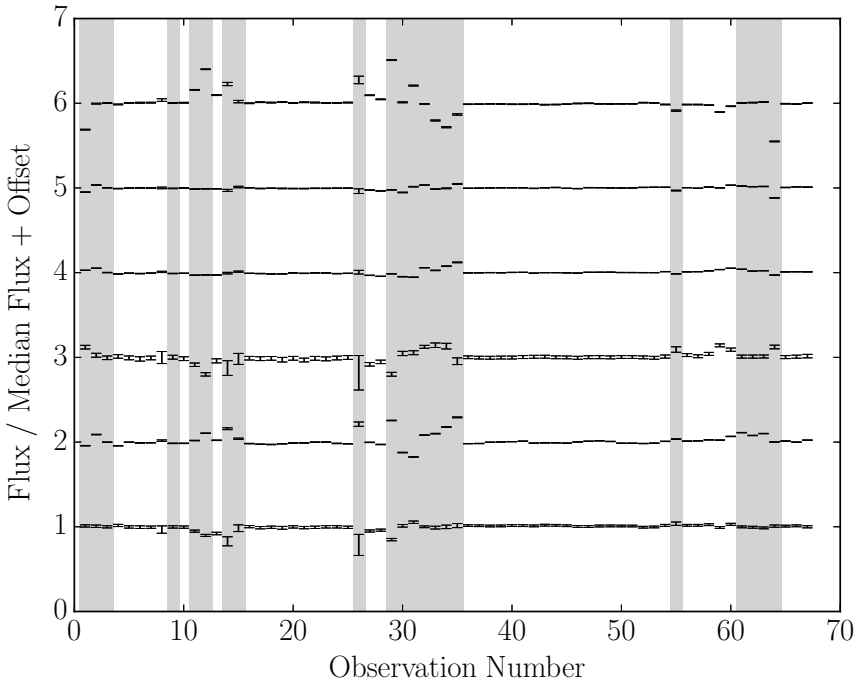

Fig. 4.6 Calibrated and normalized standard star fluxes at each epoch in the campaign. The standard star fluxes are measured using aperture photometry from the flux calibrated images, and then normalized to the median flux for all the stars at the given epoch. The lines with error bars show the normalized flux for each star. The vertical grey bands indicate the epochs that have been eliminated from the analysis due to bad PSFs or large standard star flux deviations.

pixels, to avoid as much contribution from the host galaxy as possible. We checked the effect of increasing the aperture to 10 pixels, and it did not significantly affect the light curves. Standard stars in the field are used to calculate relative fluxes between epochs. The standard stars are selected to be non-variable and away from the edge of the field and any bad pixels on the CCD. For each epoch we calculate the median ratio of the standard star fluxes with respect to a reference epoch, to allow for good inter-night flux calibration. The stabilities of the standard stars are checked by comparing the normalized calibrated fluxes for each star at every epoch (see Fig. 4.6 to 4.8). Any epoch that has star deviations above 10 % for two or more stars, is excluded from further analysis. The final number of epochs used in the light curves are listed in Table 4.1. We do not correct for any constant flux components, including contributions from the host galaxy as well as constant narrow emission lines in the AGN spectrum, as any constant emission component in the light curves is removed in the analysis by JAVELIN.

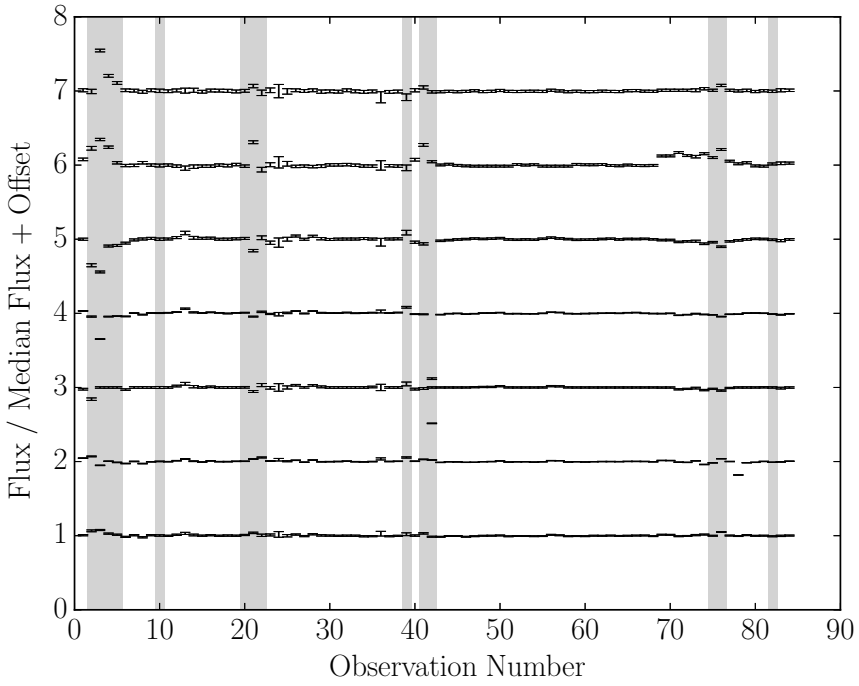

Fig. 4.7 Same as Fig. 4.6 but for NGC 4051.

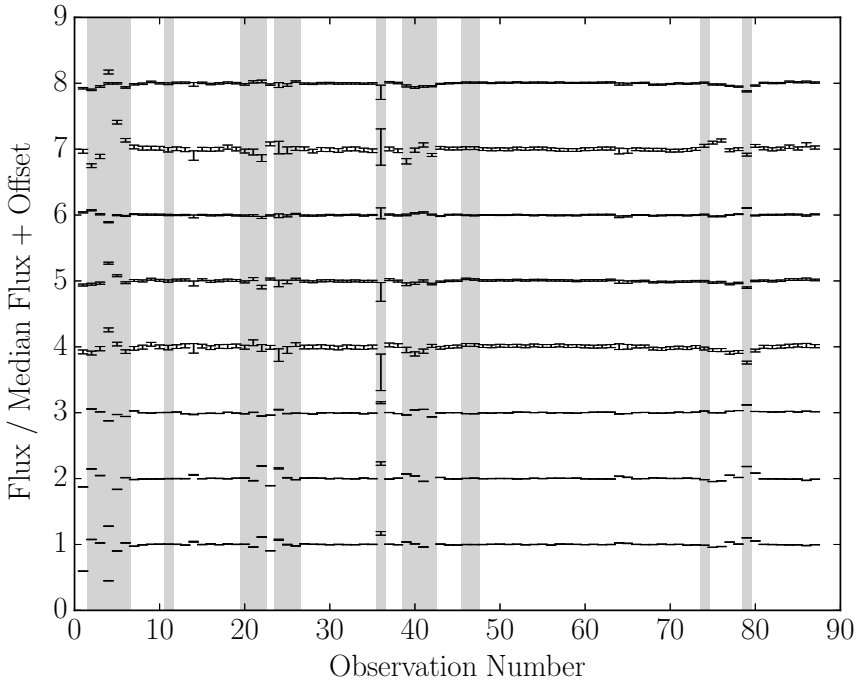

Fig. 4.8 Same as Fig. 4.6 but for NGC 4151.

4.3.5 AGN luminosities

To be able to compare our results with the radius-luminosity relation we estimate the intrinsic AGN continuum luminosity at 5100 Å, λL_λ (5100 Å), using aperture photometry. To derive the intrinsic luminosity, the images are first flux calibrated using standard stars from the Hubble Guide Star Catalog (GSC 2.3; Jenkner et al., 1990). The standard star fluxes are measured in the *V* band on background subtracted images using an aperture of 15 pixels. We tested that the precise choice of aperture has no significant effect on the derived luminosities. To test the stability of the standard photometric stars we compare the variance in calibrated flux for each star in all images from our campaign, to ensure that no star deviates significantly from the median calibrated flux for that star.

We apply standard A_V extinction corrections and use spectra from the NOT (Fig. 4.3 to 4.5) to calculate conversion factors from *V* band flux to monochromatic flux at 5100 Å for each AGN. The monochromatic flux obtained by this procedure includes a significant ($\sim 50\%$; Bentz et al., 2013) contribution from the AGN host galaxy. Bentz et al. (2013) used *Hubble Space Telescope* (HST) images and galaxy surface brightness modeling to calculate absolute host galaxy and AGN fluxes in rectangular apertures. By using the same apertures, we subtract the absolute host galaxy contribution as measured by Bentz et al. (2013), to obtain intrinsic monochromatic AGN luminosities.

To calculate the final averaged intrinsic luminosities for each AGN, we combine distances from the literature with average fluxes determined in our campaign. The literature distances used are 24 ± 3 Mpc for NGC 3227 (Tonry et al., 2001), 12.2 ± 2.4 Mpc for NGC 4051 (Tully et al., 2009) and 19 ± 2.5 Mpc for NGC 4151 (Hönig et al., 2014). The average AGN fluxes are measured by selecting a number of images with good seeing at different epochs throughout the campaign, and calculate the final flux as the median and $1-\sigma$ percentiles of the individual fluxes for each image. Because the luminosity depends on squared distance to the AGN, the error on the luminosity scales as $\delta L/L \propto 2\delta d/d$ (Taylor, 1982). The uncertainties on the distances to the AGN translates into an uncertainty on the intrinsic luminosity of $\sim 25\,\%$. This is larger than the error introduced by the standard deviation of the variation in continuum emission between epochs in the campaign, which is only of the order $\sim 5\,\%$. This means that the main uncertainty on the intrinsic luminosity comes from the measured distance to the AGN, and that estimated luminosity is not strongly affected by the specific choice of epochs. The luminosities quoted here are calculated as an average of the luminosities derived from the selected epochs across the campaign, for each object.

4.4 Photometric reverberation mapping

Reverberation mapping of AGN exploits the time delay τ between variations in the continuum emission flux to variations in the broad emission line flux. The time delay is usually interpreted as a geometrical light travel time due to an extended BLR, which is related simply to the characteristic radius of the BLR through the speed of light, $R_{\rm BLR} = c\tau$ (Couderc, 1939; Bahcall et al., 1972). In the simplest interpretation the broad emission line flux is simply continuum emission being reprocessed by gas in the broad line region (Bahcall & Kozlovsky, 1969; Davidson, 1972). The spatial and kinematic distribution of gas in the BLR means that the light curve of the BLR emission will be a smoothed version of the continuum light curve. We relate the broad emission line light curve to the continuum light curve through a transfer equation,

$$L(t) = \int \Psi(\tau) C(t-\tau) d\tau, \tag{4.1}$$

where L is the emission line light curve, C is the continuum light curve and Ψ is the transfer function for the given set of light curves. The shape of the transfer function $\Psi(\tau)$ provides information about the structure of the BLR. Determining $\Psi(\tau)$ from measurements of $L(t)$ and $C(t)$ should in principle be straight forward, but is severely complicated by the presence of noise and the recognition that the BLR emission does not always follow the continuum emission in a strictly linear fashion (Pogge & Peterson, 1992; O'Brien et al., 1995). The strategy for constraining $\Psi(\tau)$, without spatially resolving the BLR in our telescopes, is thus to make observations that approximate the ionizing continuum $C(t)$ and emission line $L(t)$ light curves in Equation 4.1.

Even if a simple time delay measurement provides less information about the structure of the AGN, compared to the full velocity resolved transfer function, it is still very useful in constraining AGN properties, such as black hole mass and intrinsic luminosity (see Section 4.2). The time delay is typically measured using cross correlation methods, which provides an estimate of the median time delay as the peak of the cross correlation function (CCF) between the continuum and emission line light curves (Gaskell & Sparke, 1986; Edelson & Krolik, 1988; White & Peterson, 1994; Peterson et al., 1998a).

Another way to measure $R_{\rm BLR}$ is to assume a parametric form for Ψ and determine the best fit parameters by convolving the continuum light curve with the transfer function to obtain a model emission line light curve that can then be compared to the data. If a transfer function is selected that is unimodal and symmetric, its position, defined as the median of the distribution, should be a good estimate for the median time delay, also found in CFF methods. Because this method provides a complete, albeit simple, model for the reverberation mapping problem, it has the benefit of providing well defined error estimates for the model parameters.

This is the strategy of the JAVELIN reverberation mapping code, which uses a top-hat model for the transfer function and includes modeling of the continuum light curve to determine a likelihood distribution for the time delay (Zu et al., 2011). This technique has already been applied in large reverberation campaigns (e.g. Grier et al., 2012).

We note that even if the true transfer function is asymmetric, using a top hat transfer function for measuring the time delay, as JAVELIN does, yields a result which is consistent with the mean time delay derived from CCF methods (Zu et al., 2011). In any situation where the transfer function is significantly asymmetric, the first moment (or the mean) will not provide a good constraint on the underlying time delay distribution (Robinson & Perez, 1990; Penston, 1991; Koratkar & Gaskell, 1991; Peterson et al., 1998b). For an example of theoretical BLR geometries leading to asymmetric time delay distributions, and the associated mean time delays, see Pancoast et al. (2014a).

JAVELIN includes a photometric reverberation mapping mode which, instead of independent continuum and emission line light curves, models photometric light curves in two different bands, one covering the broad emission line of interest, and another acting as the continuum band (Zu et al., 2016). In this model, the broad band continuum light curve is given by

$$F_c(t) = C(t) + n_c, \tag{4.2}$$

where $F_c(t)$ is the observed continuum band flux as a function of time, $C(t)$ is the intrinsic continuum light curve and n_c is the noise in the continuum band. Note that we assume that the continuum flux contains random noise, but no contribution from emission lines.

This is contrary to the narrow-band emission line light curve, which is a combination of line emission and continuum,

$$F_l(t) = \alpha C(t) + L(t) + n_l, \tag{4.3}$$

where $F_l(t)$ is the observed narrow-band flux as a function of time, $L(t)$ is the intrinsic, uncontaminated and noise free emission line light curve, n_l is the noise in the narrow band and α controls the contribution of continuum emission to the observed narrow-band flux.

The continuum light curve is modeled using a Gaussian process with a power spectral density (PSD) power law slope of -2, which is equivalent to a damped random walk (see Sec. 4.4.3). The Gaussian process takes into account uncertainties in the continuum light curve and allows for easy interpolation, needed when calculating the likelihood for time delayed light curves. We use JAVELIN to calculate likelihood distributions for the time delay between the *V* band and *hbw* band light curves for all AGN in the range $0-25$ days. The final estimate

of the BLR time-delay is calculated by marginalizing over all other parameters in the model, including the continuum contamination to the narrow band α, and the Gaussian process variability parameters. The time delay should not be degenerate with any other parameters in the model, because of the way it enters into the problem, as a linear transformation of the time coordinate. It is worth noting that the model used by JAVELIN is a phenomenological, rather than physical, model. This means that the JAVELIN time delay is difficult to interpret outside of the context of the method used to derive it (as is the case for CCF time delays). As is common in reverberation mapping studies using JAVELIN (e.g. Grier et al., 2012; Pei et al., 2014), we will provide time delay likelihood distributions along with median time delays and 1-σ percentiles in the results section.

4.4.1 The ionizing continuum

A challenge in observing $C(t)$ is that the continuum photons ionizing the BLR, to drive variations in the optical broad emission lines, are above the Lyman limit $h\nu \leq 13.6\,\mathrm{eV}$, making them very difficult to observe due to absorption. A common assumption in reverberation mapping studies is thus that the ionizing continuum is well correlated with the optical continuum observed near the emission line. In theories of AGN continuum emission mechanisms, it is proposed that the continuum originates in thermal emission from an accretion disk surrounding the black hole (e.g. Haardt & Maraschi, 1991). If the accretion disk temperature decreases monotonically with increasing radius, the disk continuum emission will likewise decrease in energy to produce longer wavelength photons further out in the disk. If in addition, the continuum variability is seeded in the inner turbulent regions of the disk or a hot corona (Ulrich et al., 1997), the variability patterns will propagate outwards to larger radii, and variations in the longer wavelength continuum will be observable at later times than the higher energy continuum originating at smaller radii.

Evidence for this continuum stratification has recently been observed in NGC 5548 using the Hubble Space Telescope combined with Swift monitoring (Edelson et al., 2015). These observations show a clear time delay of ~ 1 day between the UV continuum at 1367 Å and the optical continuum near Hβ. This means that the measured reverberation mapping time delay will not correspond to the full light travel time from the central black hole to the broad line region R_{BLR}. Instead what we measure will be the light travel time from the region of the accretion disk emitting optical continuum to the broad emission line region $R_{\mathrm{RM}} = R_{\mathrm{BLR}} - R_{\mathrm{continuum}}$. If this is a common feature of AGN variability, the measure of the time delay will be biased towards smaller BLR radii. This is important to keep in mind when interpreting any reverberation mapping campaign that measures the time delay between optical continuum and emission line variations to determine the BLR radius.

4.4.2 Emission line contamination

The JAVELIN method for photometric reverberation mapping assumes that the continuum light curve is uncontaminated by variable broad line flux (see Equation 4.2). Because we use the *V* band as the continuum light curve and the *hbw* band as the emission line light curve for Hβ, the continuum light curve will include a $\lesssim 3\%$ contamination from total Hβ (see Fig. 4.3 to 4.5). The contribution of emission line flux in the continuum band is not modeled by JAVELIN, and will make a time delay detection more difficult.

Note that if the emission line light curve has a significant fraction of continuum emission, JAVELIN should be able to model this and provide an estimate of the time delay, and the continuum fraction in the emission line band α. If the two light curves are very similar, it should of course always be considered whether the data warrants the added model complexity of an additional parameter, such as the time delay.

4.4.3 Variability model assumption

On short timescales AGN light curves are well described by a stationary random process, where the strength of the correlation between two points in the light curve is proportional to the distance between the points in the time domain. The correlation between any two points $(f_1, f_2) = (L(t_1), L(t_2))$ is encoded in the covariance function $K(t_1, t_2)$ for the random process, and the fluxes f are associated with a normally distributed (Gaussian) random variable. These types of random processes are called Gaussian processes (Kelly et al., 2009). Studies of large samples of light curves in SDSS have revealed that AGN light curves are well approximated by a Gaussian process with a particular type of covariance function called Ornstein–Uhlenbeck (OU; Gillespie, 1996; MacLeod et al., 2010; Zu et al., 2013). A Gaussian process with an OU covariance function is also known as a damped random walk (DRW). The DRW has the advantage that it is easy to calculate, and allows for fast generation of a large number of light curve realizations, required in Monte Carlo sampling procedures when fitting light curve models (Kelly et al., 2014).

JAVELIN uses a DRW for modeling the continuum light curve. This choice of model makes generating continuum light curves very efficient, and allows for quick Monte Carlo sampling of the model parameter distributions. Despite its effectiveness, there are issues related to using the simple DRW for modeling AGN light curves: The light curves generated by a DRW has a power spectral density (PSD) function with a constant slope of -2. The negative slope implies that large amplitude variations in AGN light curves happen on longer time scales, but the low PSD steepness of -2 still leaves significant power at short time scales. This means that the DRW model can fit very short time scale variations < 1 day. At

the same time, the small amplitude of short time scale variability means that variability on this scale is often dominated by measurement errors. If the measurement errors are for some reason underestimated, the residual noise will be (over) fitted by the DRW fitting procedure.

Recent studies using high signal-to-noise and high-cadence observations from *Kepler* have indeed found evidence for a steeper PSD power-law slope of up to -4.51, at time scales shorter than a few days (Mushotzky et al., 2011; Edelson et al., 2014). A steeper PSD slope means that the light curve has less structure on small scales, compared to what is predicted by the DRW model. While the results *Kepler* from cannot be immediately generalized to all AGN light curves, the results are nonetheless a strong indication that one should be careful when interpreting small time scale AGN variability using DRW models (Kasliwal et al., 2015). Small scale structure fitted by a DRW could simply be noise in the light curves, that is not accounted for by the estimated measurement errors.

The result of modeling noisy light curves using a DRW, may be that the light curves are overfitted. Overfitting the continuum light curve can have several consequences, depending on the nature of the noise. These effects include:

1. If the additional noise is due to flux calibration issues affecting both the continuum and emission line light curves in a single epoch, overfitting the light curves can introduce excess power in the time delay distribution at $\tau = 0$ (e.g. Gaskell & Peterson, 1987; Edelson & Krolik, 1988).

2. If the noise is independent between the two light curves, overfitting the continuum may still produce accurate time delay measurements, but the error on the time delay will be underestimated. This is due high frequency noise being propagated to the likelihood distribution, resulting in error estimation being done on small scale noise, rather than on the underlying likelihood signal.

To make sure that the choice of Gaussian process model for the continuum does not affect our results we ran the analysis using inflated error bars on both the continuum and the emission line light curve. The error bars were inflated by multiplying each error by a constant value of 2.0 (not shown in the figures). The precise value of the constant is not important, as long as it is chosen to be large enough that the error bars dominate over the variability on the smallest scales in the light curves. This effectively removes the effect of high frequency noise and makes the likelihood distribution smoother. For all objects analyzed, we found that even though the likelihood distributions were more smooth, the estimates of the time-delay were consistent within the errors with the results from the original (non-smoothed) likelihood distributions. This supports the picture in which overfitting the light curves produces noise in

the likelihood distribution only at smaller scales, while preserving the large-scale behavior, and thus the estimate of the time delay.

4.4.4 Stability tests of the solutions

The uncertainties on the emission line light curve, enters in the solution through the likelihood in the Markov Chain Monte Carlo (MCMC) sampling. To allow for additional systematic uncertainties, not included in the error-bars, we resample the emission line light curve 1000 times and add the time delay likelihood distributions for all samples. We tested different numbers of samples, and found that the likelihood distributions converged fairly quickly after about 100 samples. After this the results changed very little, and always within the errors. In any case, to be on the safe side, we ran the simulation 10 times longer than that to a total of 1000 samples. Resampling has the effect of broadening the likelihood distributions, and provides a conservative estimate of the total statistical and systematic uncertainty on the time delay for each object. Resampling of the light curve error bars, as is typically done in cross correlation methods (Peterson et al., 1998b) is not required, as the error bars in the light curves are already taken into account by JAVELIN.

4.5 Results

Figure 4.9 to 4.11 show results from photometric reverberation mapping of NGC 3227, NGC 4051 and NGC 4151. The *V* band and *hbw* band photometric light curves are plotted as black points with error bars and the best fit model from JAVELIN is plotted as a solid line with the error on the best fit model shown as a translucent band. For each object we also plot the likelihood distribution of time delays from the photometric mode of JAVELIN, obtained by resampling of the *hbw* band light curve (see Section 4.4.4 above). We describe the results for each object in detail below.

Deriving a time delay by cross correlating the continuum and emission line light curves, as is typically done in reverberation mapping studies (Peterson, 1993), is made difficult by the fact that the narrow band (emission line) light curves are significantly contaminated by the underlying continuum. We therefore apply the photometric mode of JAVELIN to model the continuum contamination, and estimate the emission line time delay simultaneously. Because of the continuum contamination, the standard cross correlation method will be much less sensitive to the time delay, and will instead mainly pick up the strong correlation of the two light curves at 0 days.

All luminosities are provided logarithmically as $\log \lambda L_\lambda\,(5100\,\text{Å})/\text{erg}\,\text{s}^{-1}$.

Object	Band	Epochs	F_{var}	R_{max}	Band	Epochs	F_{var}	R_{max}
NGC 3227	*V*	57	0.031	1.14 ± 0.04	*hbw*	36	0.050	1.20 ± 0.03
NGC 4051	*V*	70	0.037	1.19 ± 0.04	*hbw*	44	0.062	1.34 ± 0.05
NGC 4151	*V*	71	0.039	1.19 ± 0.02	*hbw*	54	0.047	1.21 ± 0.02

Table 4.1 Photometric light curve statistics. F_{var} is the fractional root mean square variability amplitude (see Vaughan et al., 2003) and R_{max} is the ratio between the maximum and the minimum flux in the light curve.

Object	Spectral SNR	Hβ equivalent width (Å)	$\log \lambda L_\lambda$ (5100 Å) / erg s^{-1}	Hβ time delay
NGC 3227	42	46	42.60 ± 0.12	$5.9^{+2.0}_{-1.9}$ days †
NGC 4051	37	47	41.90 ± 0.22	$6.0^{+4.6}_{-3.6}$ days
NGC 4151	112	148	42.75 ± 0.13	$11.7^{+2.7}_{-3.0}$ days

Table 4.2 Spectral statistics and photometric reverberation mapping results. Time delays are in the rest frame. † The time delay for NGC3227 is based on a strong prior from the radius-luminosity relationship (see Section 4.5.1).

4.5.1 NGC 3227

The spectrum of NGC 3227 (Fig. 4.3) shows that the *hbw* band and the Hβ emission line are well aligned. The spectral signal to noise ratio (SNR) is ~ 42 and the equivalent width of Hβ is ~ 46 Å.

The *V* band and *hbw* band light curves for NGC 3227 (Fig. 4.9, *left*) start out fairly flat but then show a distinct decrease in flux lasting about 30 days after which the light curves increase to recover the flux levels of the beginning of the campaign. Towards the end of the campaign, a significant number of epochs had to be discarded because of asymmetric PSFs or bad convolutions. The final light curves include 57 epochs in the *V* band and 36 epochs in the *hbw* band.

The time delay distribution for NGC 3227 has a clear peak close to 0 days (Fig. 4.9, *right*). This may be explained by correlated errors due to systematic flux calibration errors in the light curves, as well as the poor sampling of the NGC 3227 light curves compared to the other objects. We determine the luminosity of NGC 3227 to be $\log \lambda L_\lambda\,(5100\,\text{Å})/\text{erg}\,\text{s}^{-1} = 42.6$. Using the radius-luminosity relation from Bentz et al. (2013) we estimate the expected time delay for NGC 3227 to be 6.0 days. The time delay distribution does seem to have a secondary peak around 6 days. If this is the true delay then the preference for a 0 day delay could be an indication of uncertainties shared between the *V* band and *hbw* band light curves, as described in Section 4.4.3).

By adding a strong prior from the radius luminosity relation on the time delay of NGC 3227 (of 6 ± 3 days, indicated by the vertical dotted lines in Fig. 4.9), we recover a time delay for NGC 3227 of $5.9^{+2.0}_{-1.9}$. This result is obviously highly biased towards the delay predicted by the radius luminosity relation, and should not be regarded as an independent measurement. Although the fact that we observe a bump in the likelihood distribution at ~ 6 days, is consistent with the expectation.

NGC 3227 was monitored for five months in 1990, with the results reported in (Salamanca et al., 1994). Using cross correlation methods they found a time delay for the Hα-line of 18 ± 7 days. While our results cannot be immediately compared due to the intrinsic radius luminosity relation, the Hα time delay from 1990 is nonetheless compatible without value of $5.9^{+2.0}_{-1.9}$ days, provided one assumes a scaling ratio between the time delays of Hα and Hβ of ~ 1.5 (Bentz et al., 2010a).

4.5.2 NGC 4051

The spectrum of NGC 4051 (Fig. 4.4) is of similar quality to that of NGC 3227 with a SNR of ~ 37 and Hβ equivalent width of ~ 46. The Hβ line is well covered by the *hbw* band.

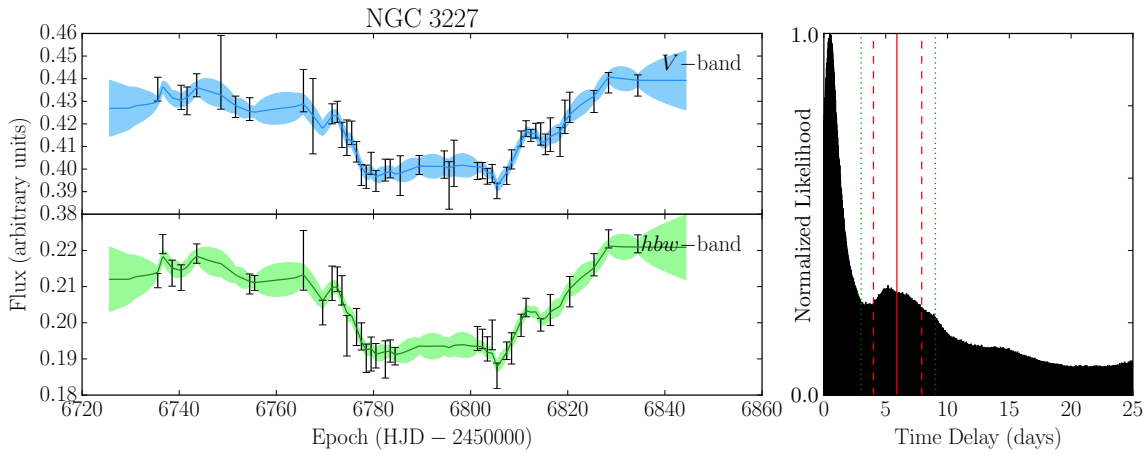

Fig. 4.9 Results from photometric reverberation mapping of NGC 3227. The left panels show photometric light curves in the *V* band (upper-left) and *hbw* band (lower-left) as black points with error bars. The best fit light curves from JAVELIN are shown as a solid line and 1σ error band on top of the two light curves. The right panel shows the likelihood distribution of the observed-frame time delay model parameter from JAVELIN. The likelihood distribution is a sum of distributions from the analysis of 1000 re-samples of both light curves. The median time delay is indicated by a solid vertical red line on top of the likelihood distribution, and the lower and upper 1σ percentiles are indicated by dashed vertical lines. The vertical green dotted lines indicate the region of the uniform prior used to calculate the time delay for NGC 3227. The results are described in Section 4.5.1.

The light curves for NGC 4051 (Fig. 4.10, *left*) have a slight rise in the beginning of the campaign up to a maximum at about 6740 days after which it drops off for 40 days and shows only minor variability features for the rest of the campaign.

The time delay distribution from JAVELIN (Fig. 4.10, *right*) shows a small peak at 0 days, which may be due to correlated errors in the light curves because of bad flux calibrations affecting some epochs. Even though the peak at $\tau \sim 0$ days is approximately the same height as the peak at $\tau \sim 5$ days, the second peak is significantly broader, and dominates the estimate of the median time delay. Note that because the likelihood distribution has non-negligible power at the boundaries (0 and 25 days), the exact position of the prior becomes important. We tested the effect of increasing the boundaries of the prior by ~ 10 days at either end of the distribution (which in this case includes negative time delays), and found that the results were not strongly affected. For this reason, we keep the prior on the time delay the same as for the other objects. Using the full likelihood distribution from 0 days to 25 days, we recover a time delay for NGC 4051 of $6.0^{+4.6}_{-3.6}$ days.

4.5.3 NGC 4151

The spectrum for NGC 4151 (Fig. 4.5) is the best quality of the three AGN analyzed, with a spectral SNR of ~ 112 and Hβ equivalent width of ~ 148. As for the other objects, the low redshift of the AGN results in the Hβ broad line being completely covered by the *hbw* band.

The NGC 4151 photometric light curves (Fig. 4.11, *left*) have the most epochs and highest SNR of the sample. The light curves show significant variability during the observed period, with a maximum early in the campaign around $JD = 6740$ and then a gradual decrease in luminosity with clearly resolved smaller scale variability.

The likelihood for NGC 4151 from our bootstrap analysis shows a clear peak around a time delay of 10 days with the likelihood dropping to zero on either side (Fig. 4.11, *right*). This is indicative of a clear signal in the data, and is likely due to the high signal to noise of the light curves, and a low degree of correlated errors. From the likelihood distribution we recover a time delay for NGC 4151 of $11.7^{+2.7}_{-3.0}$ days.

4.5.4 Radius Luminosity Relation

We add our new reverberation mapping results to the Hβ radius luminosity relation using the mean luminosities measured for our campaign. This is shown in Fig. 4.12. For comparison we show the best fit relation and spectroscopic data points from Bentz et al. (2013) as well as recent photometric reverberation mapping results by Haas et al. (2011) and Pozo Nuñez et al. (2012). The results from photometric reverberation mapping are in good agreement with the

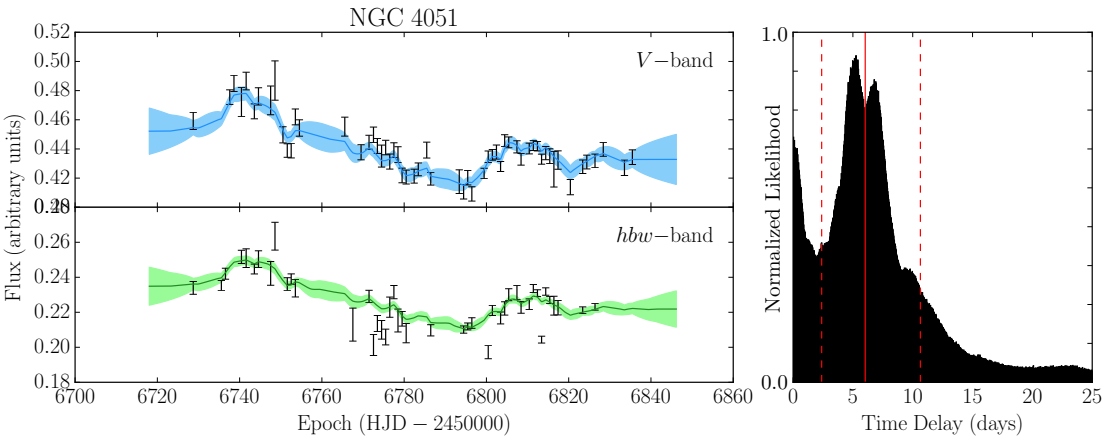

Fig. 4.10 Same as Fig. 4.9 but for NGC 4051. The results are described in Section 4.5.2.

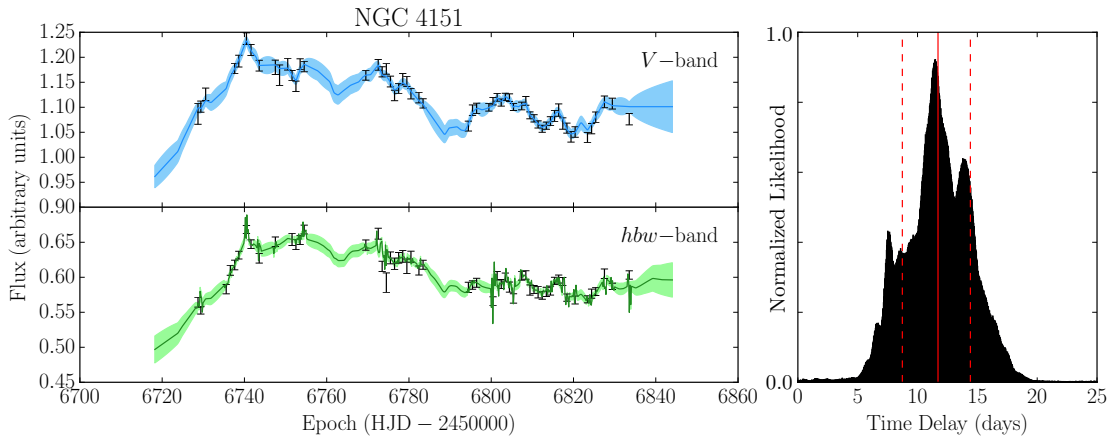

Fig. 4.11 Same as Fig. 4.9 but for NGC 4151. The results are described in Section 4.5.3.

spectroscopic radius luminosity relation. Our results support the notion that individual AGN follow the R-L relation during normal variability, as observed previously, in the case of NGC 5548 by (Cackett & Horne, 2006).

The luminosity ($\log \lambda L_\lambda\,(5100\,\text{Å})/\text{erg}\,\text{s}^{-1}$) of NGC 3227 has increased from 42.24 ± 0.11 measured by Bentz et al. (2013) to our value of 42.60 ± 0.12.

The time delay distribution for NGC 3227 made it impossible to determine an independent time delay for this object (see Section 4.5.1). Instead, the quoted time delay is calculated using a narrow uniform prior with a width of 6 days, centered on the expected value from the radius luminosity relation (see Fig. 4.5.1). The results for NGC 3227 should therefore not be regarded as an independent measurement.

The luminosity of NGC 4051 in our survey is consistent with previous results. The time delay is somewhat larger, at $6.0^{+4.6}_{-3.6}$ days compared to $1.87^{+0.54}_{-0.50}$ from Bentz et al. (2013), but again, largely consistent given the uncertainties.

Both the luminosity and time delay of NGC 4151 are significantly larger than the results from Bentz et al. (2013). The luminosity has increased by a factor of 4.6 from a log luminosity of 42.09 ± 0.22 to 42.75 ± 0.13, while the time delay has increased by from $6.58^{+1.12}_{-0.76}$ days to $11.7^{+2.7}_{-3.0}$ days. This change is in good agreement with the general trend of the radius luminosity relation.

4.6 Discussion

4.6.1 Assessing systematics

The results obtained agree well with previous studies, including the radius luminosity relation Bentz et al. (2013). This is encouraging, but given the small sample size, and the fact that we failed to recover a robust time delay in one of the objects (NGC 3227), one should be careful in forming strong conclusions regarding the efficacy of photometric reverberation mapping. The failure to obtain an independent measurement for NGC 3227 may be due to a significant contribution of continuum emission in the *hbw* band, likely compounded by the fact that we obtained only 57 epochs of measurements for this object.

The results from this work can be regarded as a successful attempt at measuring AGN time delays using small (1.2 m) remotely controlled telescopes under average to poor observing conditions. A possible next step is to organize a campaign with simultaneous spectroscopic monitoring to enable direct comparison with established spectroscopic reverberation mapping methods. Another possibility is to obtain photometric time delays for a large number of AGN,

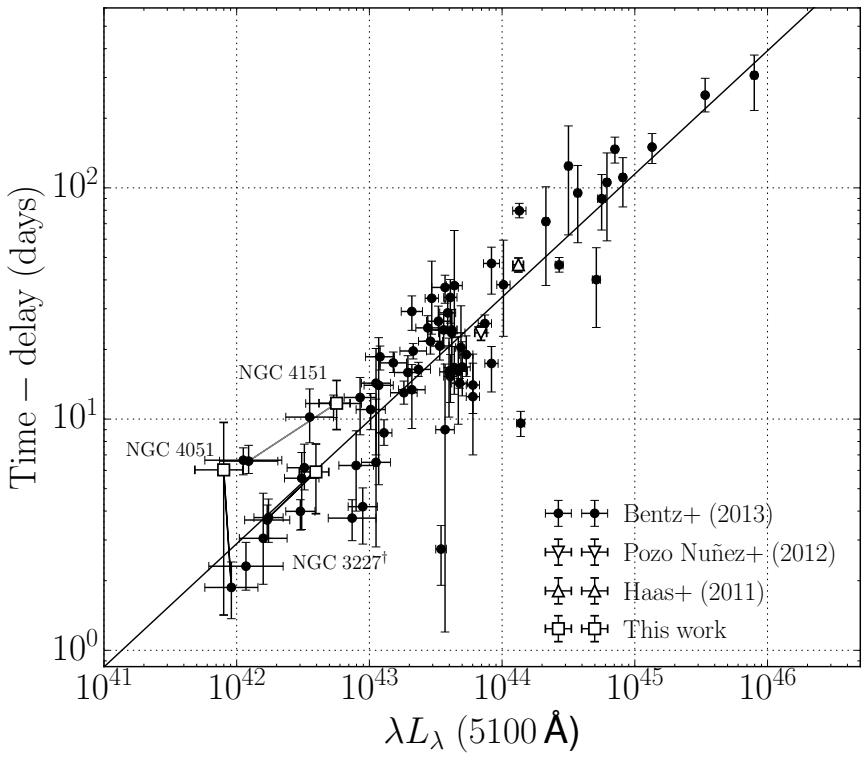

Fig. 4.12 Radius luminosity relation for AGN. Solid circles are data from Bentz et al. (2013). The triangle pointing down is from photometric reverberation mapping by Pozo Nuñez et al. (2012). The open triangle pointing down is from photometric reverberation mapping by Haas et al. (2011). The open squares are data from this work. The solid lines indicate the positions of AGN in the relation determined by Bentz et al. (2013) for the objects analyzed in this work. † The plotted time delay for NGC 3227 was obtained using a strong prior from the radius luminosity relation, and should not be regarded as an independent measurement.

to probe existing scaling relations using only photometric reverberation mapping. These relations could then be used to assess possible systematics inherent to this method.

Another class of useful tests would include comparing emission line diagnostics, such as broad emission line equivalent widths, for a number of epochs which have both spectroscopic as well as photometric observations. If the shape of the broad lines changes, or if the lines are significantly blended, this may introduce errors in narrow band flux monitoring because the fraction of line emission falling inside the band changes as a function of time. This would require spectral decompositions at several epochs throughout the campaign of the emission lines in question.

4.6.2 AGN luminosities at high redshift

Probing the radius luminosity relation at high redshift requires accurate AGN luminosities. The method applied here, where high-resolution HST images are modeled to isolate the AGN component, is simply not feasible at higher redshifts. A possible solution is to obtain spectra and model the AGN and host galaxy spectral components to determine the host galaxy contribution in the photometric bands. Another possibility is to use the flux variation gradient method devised by Choloniewski (1981), see also Winkler (1997). This method uses the difference in spectral slopes between the AGN and the host galaxy to isolate the AGN luminosity by comparing the variation in flux between different photometric bands. The method has been successfully applied in recent narrow band reverberation mapping campaigns (Haas et al., 2011; Pozo Nuñez et al., 2012, 2013, 2015), and could potentially allow accurate photometric host galaxy subtraction at high redshift.

Despite the issues of acquiring accurate intrinsic AGN luminosities at high redshift, it is worth noting that host galaxy contamination becomes less important with increasing redshifts. This is partly due to the fact that high redshift AGN are observed at rest-frame UV wavelengths, where the host galaxy is less dominant, and because at higher redshifts we typically observe higher luminosity AGN (Cowie et al., 2003; Ueda et al., 2003; Hasinger et al., 2005; Silverman et al., 2008), mitigating the need for high precision host galaxy subtraction when observing AGN outside the local universe.

4.6.3 Narrow band photometry at high redshift

Using narrow band photometry to separate the continuum and line emission works well at low redshift, because we have standard narrow photometric bands covering the emission lines of interest. At higher redshifts the broad emission lines used for reverberation mapping are redshifted out of the commercial narrow band filters. This poses practical limitations

on the feasibility of photometric narrow-band reverberation mapping at high redshift, that can only be overcome by the development of new filters or new techniques for high redshift narrow band photometric reverberation mapping.

An alternative approach is to use broad band filters at high redshift. Broad band photometric reverberation mapping has been successfully applied to low ($z < 0.1$) and intermediate ($0.1 < z < 0.4$) redshift AGN (e.g. Chelouche & Daniel, 2012; Chelouche et al., 2012; Edri et al., 2012). Broad band reverberation mapping techniques may be extendable to high redshift, but presents challenges in controlling emission line contamination in the broad band filters.

4.7 Summary and conclusion

Using the 1.2 m *STELLA* Robotic Observatory we obtained photometric broad *V* band and narrow *hbw* band light curves for three nearby AGN (NGC 4151 NGC 4051 and NGC 3227). For each object we measured the Hβ broad emission line time delay by photometric reverberation mapping, and the intrinsic AGN luminosity using aperture photometry and host galaxy subtraction. All measured time delays were in good agreement with previous spectroscopic reverberation mapping results, and consistent with the radius luminosity relation for AGN. By comparing with previous measurements we found good agreement with a picture in which individual AGN follow the radius luminosity during normal variability.

The work presented here is part of an effort to develop and test methods for AGN reverberation mapping using narrow band photometry. Similar methods have already proven successful in recovering AGN time delays in a number of objects (Haas et al., 2011; Chelouche & Daniel, 2012; Edri et al., 2012; Pozo Nuñez et al., 2013, 2015; Jiang et al., 2016). The results presented here suggest that photometric reverberation mapping is a viable addition to spectroscopic reverberation mapping, that can be applied independently to estimate AGN broad emission line time delays. This is important because photometric surveys are typically significantly less expensive than similar spectroscopic reverberation mapping campaigns, and allow for more accurate flux calibrations. In addition, our work is evidence that photometric reverberation mapping can be feasible even under difficult observing conditions, using modest (1.2 m) telescopes and short exposures.

These results present an attempt at photometric reverberation mapping of low redshift AGN under suboptimal observing conditions. To assess whether photometric reverberation mapping is a feasible tool for studying general properties of AGN, additional photometric campaigns are required. These campaigns should study both single nearby objects with existing spectroscopic reverberation mapping results, to examine possible systematic differ-

ences between the two methods, as well as larger samples of AGN, to explore the range of conditions under which photometric reverberation mapping can meaningfully contribute to the progression of the field of AGN research.

If photometric reverberation mapping turns out to be a robust and viable method, it will significantly expand options for future AGN reverberation mapping campaigns, by allowing more and fainter AGN to be observed and analyzed. New surveys such as the Large Synoptic Survey Telescope (LSST, LSST Science Collaboration et al. 2009) will provide broadband photometric monitoring in a number of bands across a large area of the sky (Hönig, 2014). The possibility of recovering reverberation mapping time delays for a large number of AGN opens new opportunities for studying and understand the structure and evolution of AGN, as well as pushing forward the possibility of using AGN as standard candles for cosmology.

Acknowledgments

This work is based on observations made with the Nordic Optical Telescope, operated on the island of La Palma jointly by Denmark, Finland, Iceland, Norway, and Sweden, in the Spanish Observatorio del Roque de los Muchachos of the Instituto de Astrofísica de Canarias. The data presented here were obtained in part with ALFOSC, which is provided by the Instituto de Astrofísica de Andalucia (IAA) under a joint agreement with the University of Copenhagen and NOTSA. Dark Cosmology Centre is funded by the Danish National Research Foundation. All figures are produced in MATPLOTLIB (Hunter, 2007).

Chapter 5

Conclusion & outlook

The past 100 years of astronomy and astrophysics have brought unimaginable revolutions in our understanding of the universe and our place in it. Those revolutions were made possible by the unrelenting strive to explore, and the unwavering power of imagination possessed by current and past generations of scientists and curious laypeople alike. Each time we explore a new place, nature reveals to us stunning complexity. If we can find and explore the principles that govern the beauty and simplicity of nature's inner workings, we will be in a position to better understand our place on Earth, and in the universe. To this end I have explored the structure of some of nature's most formidable creations; clusters of galaxies and supermassive black hole.

In Chapter 2 I present the first ever measurement of anisotropic kinematics of members in clusters of galaxies (Skielboe et al., 2012). This measurement was done by showing that clusters members lying along the major axis of galaxy clusters have, on average, larger velocities compared to those lying closer to the minor axis. This result is consistent with numerical simulations (e.g. Cole & Lacey, 1996) and supports the picture in which cluster haloes are aligned with the large-scale filaments (Joachimi et al., 2015), with galaxies fall into clusters primarily along the filaments, resulting in larger velocity dispersions in the direction of infall. In addition, it shows clearly that clusters of galaxies are aspherical objects, and that special care has to be taken when calculating cluster mass functions, as to not bias the results (e.g. Piffaretti & Valdarnini, 2008; Saro et al., 2013).

The recent *Hubble Space Telescope* (HST) Frontier Fields observing program has provided unparalleled deep observations of a number of galaxy clusters (Lotz et al., 2014). The high-resolution imaging of HST allows calculation of highly precise mass distributions using gravitational lensing analyses. This has led to three-fold improvements in cluster mass estimates (Jauzac et al., 2014), and provided unprecedented insights into the dynamics of

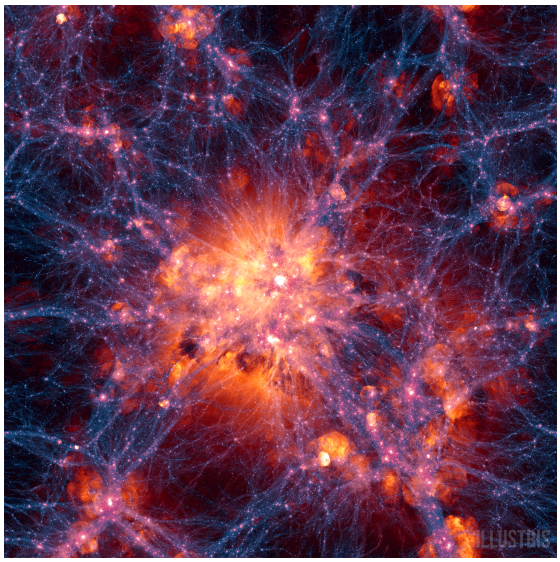

Fig. 5.1 Snapshot of the Illustris simulation using the AREPO moving mesh code (Vogelsberger et al., 2014).

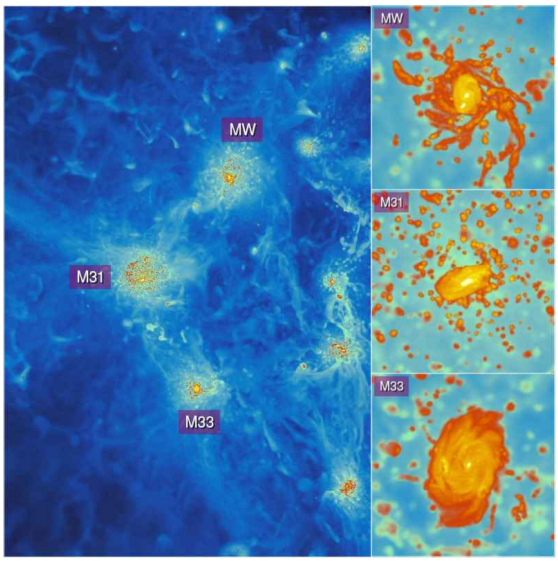

Fig. 5.2 Snapshot of the CLUES simulation of the local group of galaxies (Gottloeber et al., 2010).

clusters and large-scale structure filaments by the study of cluster mergers (Jauzac et al., 2015).

Advances in cosmological simulations have likewise provided new tools by which we can study the evolution of large-scale structure, formation of galaxies and the connection to the local universe (Nelson et al., 2015). These new generation of simulations provide more accurate hydrodynamic calculations, altering the way in which gas accretes onto dark matter haloes (see Fig. 5.1). Previous N-body simulations showed a significant fraction of cold gas falling deep into the halos (e.g. van de Voort et al., 2011), while new simulations show that a much larger fraction of the gas is heated in the infall, reducing the degree of collimation in large scale filament flows (Nelson et al., 2013). These results fundamentally change the way we view the formation and evolution of galaxy clusters in the universe. At the same time, simulations of the local group of galaxies (Gottloeber et al., 2010), including the Milky Way and the Andromeda Galaxy, are providing new insights into the distribution and kinematics of matter in the very local universe (see Fig. 5.2). The results show a high degree of alignment extending all the way from sub-galactic scales to the local large-scale structure, strengthening the case for collimated anisotropic accretion as a fundamental mode of structure formation (Libeskind et al., 2011). The coming years will only provide more insights into structure and evolution of the universe, with observatories such as Euclid coming online (Amendola et al., 2013).

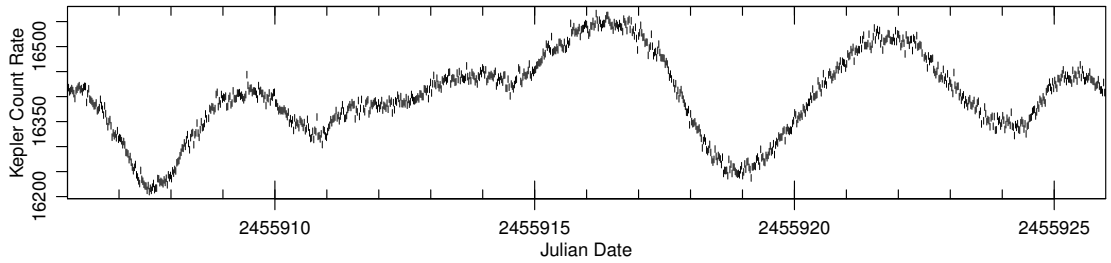

Fig. 5.3 High-resolution light curve of the AGN Zw 229-15, observed using the *Kepler* spacecraft (Edelson et al., 2014).

In Chapter 3 I probe the structure of five nearby active galactic nuclei (AGN), by studying the light echoes in the broad emission lines. This was accomplished by developing a new method for reverberation mapping based on regularized linear inversion (Krolik & Done, 1995). The method is an analytical solution to the reverberation mapping problem combined with statistical modeling of AGN light curve errors. This provide conservative and robust estimates of the broad emission line response to incoming ionizing radiation, as a function of wavelength, and yields fully velocity resolved response maps. These velocity-delay maps provide new insights into the sub-parsec structure of AGN, and enable broad line region and AGN unification model constraints. The results from regularized linear inversion are validated by comparing the integrated time-delays to previous results obtained using alternative methods.

Recent and upcoming reverberation mapping campaigns are pushing the limits of classical linear reverberation mapping techniques. Results from the *Kepler* spacecraft (e.g. Edelson et al., 2014) are providing exceedingly high resolution broad band photometric light curves of nearby AGN (see Fig. 5.3). These results present new challenges in modeling AGN light curves, and prompt us to look beyond simple random walk variability models. In addition, space based spectroscopic reverberation mapping campaigns, such as AGN STORM (De Rosa et al., 2015; Edelson et al., 2015), has recently provided the highest quality spectroscopic reverberation mapping dataset to date. Like the high cadence data from Kepler, these datasets are helping us explore the limits of reverberation mapping, and expand our understanding of AGN physics. The field of high-resolution reverberation mapping is still in its infancy, and new observing strategies, reverberation mapping methods and theoretical models will all have to be evolved to accommodate the influx of new AGN data.

Chapter 4 takes a different approach to reverberation mapping, by aiming to measure integrated time delays using only photometric observations. This work suggests that it may be feasible to measure time delays using inexpensive photometric monitoring on a large number of AGN, required to accurately constraining AGN scaling relations at high redshift.

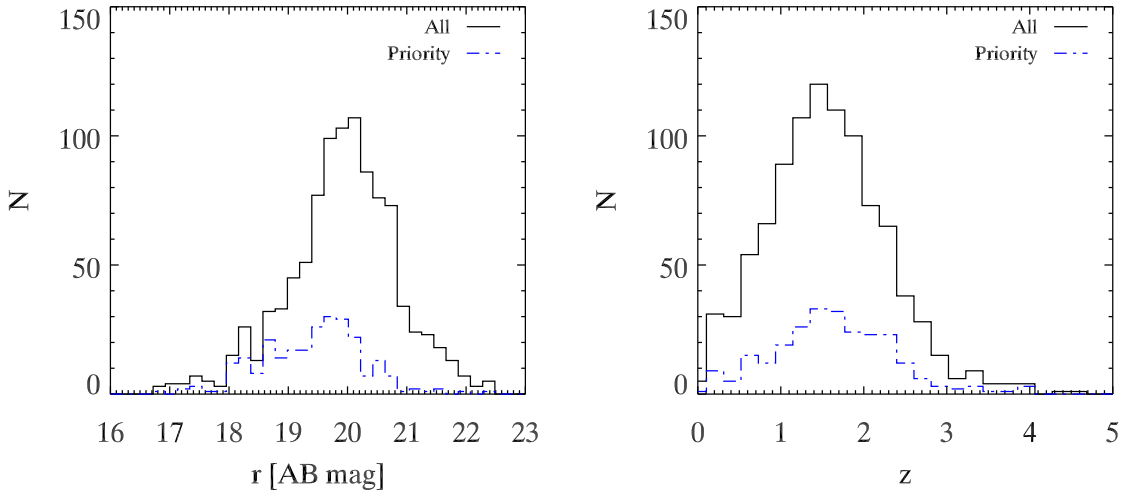

Fig. 5.4 Simulations of the OzDES AGN Reverberation Mapping Project showing the AGN target sample distributions in AB magnitude (left) and redshift (right). Measuring reverberation mapping parameters for AGN at high redshift opens up a whole new field of studying AGN demographics across cosmic time. Reproduced from King et al. (2015).

How photometric reverberation mapping will perform in a large scale monitoring campaign is yet to be tested.

A number of large scale reverberation mapping surveys have recently been designed to measure properties of large samples of AGN (Shen et al., 2015; King et al., 2015). If successful, these surveys will extend our knowledge of AGN properties at a range of redshifts and luminosities, and if they can overcome the challenges of reverberation mapping at high redshift, may greatly benefit the study of AGN demographics and scaling relations across cosmic time. Long baseline reverberation mapping surveys on dedicated telescopes may provide the observing times required to do reverberation mapping at high redshift (see Fig. 5.4), moving us closer to using AGN variability to derive independent complementary constraints on cosmological models (e.g. Watson et al., 2011; King et al., 2014).

Apart from dedicated reverberation mapping surveys, future all-sky surveys such as that conducted using the Large Synoptic Survey Telescope (LSST Science Collaboration et al., 2009), will provide new data on billions of galaxies, enabling high precision studies of galaxy clusters as well as constraints on AGN ensemble variability. Finally, new developments in numerical simulations allows new tests of theories of structure formation and dynamics, as well as testing theories of the co-evolution of AGN and host galaxies, as well as AGN feedback in clusters of galaxies (e.g. Vogelsberger et al., 2014; Sijacki et al., 2015; Haider et al., 2015).

The past 100 years' discoveries in physics and astronomy have brought fundamental changes in our view of the cosmos and our place in it. Today, every day, thousands of people from all over the world contribute and collaborate to continuously expand our knowledge of the universe. It is my hope that the methods and results presented in this thesis will provide inspiration, as well as concrete tools, for the exploration of future observations, theories and numerical simulations. The quest for uncovering the mysteries of the universe is far from over. In a way it has only just begun. I am honored and humbled to be part of this scientific endeavor, and wish that future generations will be equally swept away by the wonders of the universe, and also that they will see the value in preserving our habitat for thousands of future generations of inquisitive beings.

Resumé på Dansk

Siden Newton formulerede sin teori om universel gravitation, har tyngdekraften spillet en afgørende rolle i udforskningen af universet. Fordi tyngdekraften er den eneste fundamentale naturkraft, der er relevant på stor skala, er det også tyngdekraften der afgør universet udvikling og skæbne. Einsteins generelle relativitetsteori, udviklet i starten af det 20. århundrede, var startskuddet til moderne fysisk kosmologi. I dag beskriver vi universets udvikling ved hjælp af kosmologiske modeller, der bygger på generel relativitetsteori. Som i alle fysiske modeller, afgrænses parametre i modellen ved at sammenligne modelforudsigelser med observationer. I kosmologi er dette observationer af strukturen i universet på stor skala.

De største gravitationelt bundne objekter i universet er hobe af galakser. Galaksehobe består af mellem 10 og op til flere end 1000 galakser, som er bundet af det gravitationelle potentiale af hoben. Målinger af galaksehobes masser giver et mål for fordelingen af struktur i universet, som blandt andet kan benyttes til at teste kosmologiske modeller for universet. Vejning af galaksehobe afslører også tilstedeværelsen af en meget stor mængde af ekstra tyngdekraft, som ikke kan forklares ved nogen kendt type af stof. Denne ekstra tyngdekraft beskrives i stedet som "mørkt stof", en slags stof som kun reagerer med tyngdekraften, og som derved ikke udsender nogen form for lys. Mængden af mørkt stof i galaksehobe kan være helt op til 90 % af hobens masse og har derfor helt afgørende betydning for dannelsen og udviklingen af struktur i universet på stor skala. En metode til at bestemme massen af galaksehobe, og at undersøge storskalastrukturen omkring hobene, er at måle hastighederne af galakser i hoben. I disse målinger antages det typisk, at hoben er sfærisk symmetrisk. Flere observationer tyder dog på, at dette ikke er tilfældet.

I kapitel 2 præsenteres den første måling nogensinde foretaget af ikke-isotropisk kinematik i galaksehobe. Kinematikken af galakser i hobe afgøres af formen af tyngdepotentialet af hoben. Derudover påvirkes hastighedsfeltet af galakserne af retningerne, langs hvilke galakser falder ind i hoben fra den omkringliggende storskalastruktur. Måling af ikke-isotropisk kinematik er derfor en vigtig milepæl i udforskningen af dannelsen, fordelingen og udviklingen af storskalastrukturen i universet. Disse resultater kan derfor også have konsekvenser for efterforskningen af kosmologiske modeller.

Hvor galaksehobe er de største gravitationelt bundne objekter i universet, er sorte huller de mest kompakte. Supermassive sorte huller i midten af galakser, er de største sorte huller vi har kendskab til. Når gas og støv kommer tæt på det sorte hul bliver det accelereret af det enorme tyngdefelt, som varmer gassen op og får den til at udsende store mængder stråling ved alle bølgelængder. I nogle tilfælde vil gassen blive i en stabil skive omkring det sorte hul, og derved konstant udsende lys fra midten af galaksen, hvor det supermassive sorte hul befinder sig. Når det sker kaldes galaksen for en aktiv galakse, og det supermassive sorte hul samt strukturen af støv og gas omkring det kaldes for en aktiv galaksekerne (active galactic nucleus, AGN).

I kapitel 3 præsenterer jeg en ny metode til at bestemme den tredimensionelle struktur af gassen i aktive galaksekerner. Metoden bygger videre på tidligere metoder og er baseret på "reverberation mapping" ved hjælp af lineær inversion, sammen med en statistisk modellering af lyskurver fra aktive galaksekerner. Jeg fremlægger nye resultater fra analyse af data fra fem nærliggende aktive galakser. Disse resultater kan bruges til at teste fysiske modeller for strukturen af aktive galaksekerner og kan give et indblik i hvilken betydning aktive galaksekerner har for udviklingen af galakser generelt. Den antagede fysiske struktur af aktive galaksekerne har blandt andet afgørende betydning for nøjagtigheden af massemålinger af de sorter huller.

Kapitel 4 omhandler en anden metode til strukturbestemmelse af aktive galaksekerner, baseret på fotometri i stedet for spektre. Denne metode er relativt ny og tillader målinger af masser af og afstande til aktive galaksekerner, som er langt billigere i observationstid, og lettere at foretage, end metoder baseret på spektral data. Jeg præsenterer resultater fra tre nærliggende aktive kvasarer og diskuterer anvendeligheden af metoden ved høj rødforskydning, som er nødvendig for at kunne bruge aktive galakser til at teste kosmologiske modeller.

List of publications

Measuring the Three-dimensional Shape of X-Ray Clusters
*Samsing, J., **Skielboe, A.**, and Hansen, S. H. (2012). ApJ, 748:21.*

Spatial Anisotropy of Galaxy Kinematics in Sloan Digital Sky Survey Galaxy Clusters
***Skielboe, A.**, Wojtak, R., Pedersen, K., Rozo, E., and Rykoff, E. S. (2012). ApJ, 758:L16.*

Simulations of the OzDES AGN reverberation mapping project
*King, A. L., Martini, P., Davis, T. M., Denney, K. D., Kochanek, C. S., Peterson, B. M., **Skielboe, A.**, Vestergaard, M., Huff, E., Watson, D., Banerji, M., McMahon, R., Sharp, R., and Lidman, C. (2015). MNRAS, 453:1701–1726.*

Constraints on the broad line region from regularized linear inversion: velocity-delay maps for five nearby active galactic nuclei
***Skielboe, A.**, Pancoast, A., Treu, T., Park, D., Barth, A. J., and Bentz, M. C. (2015). MNRAS, 454:144–160.*

Space Telescope and Optical Reverberation Mapping Project. IV. Anomalous Behavior of the Broad Ultraviolet Emission Lines in NGC 5548
*Goad, M. R.; Korista, K. T.; De Rosa, G.; Kriss, G. A.; Edelson, R.; Barth, A. J.; Ferland, G. J.; Kochanek, C. S.; Netzer, H.; Peterson, B. M.; Bentz, M. C.; Bisogni, S.; Crenshaw, D. M.; Denney, K. D.; Ely, J.; Fausnaugh, M. M.; Grier, C. J.; Gupta, A.; Horne, K. D.; Kaastra, J.; Pancoast, A.; Pei, L.; Pogge, R. W.; **Skielboe, A.**; Starkey, D.; Vestergaard, M.; Zu, Y.; Anderson, M. D.; Arévalo, P.; Bazhaw, C.; Borman, G. A.; Boroson, T. A.; Bottorff, M. C.; Brandt, W. N.; Breeveld, A. A.; Brewer, B. J.; Cackett, E. M.; Carini, M. T.; Croxall,*

K. V.; Dalla Bontà, E.; De Lorenzo-Cáceres, A.; Dietrich, M.; Efimova, N. V.; Evans, P. A.; Filippenko, A. V.; Flatland, K.; Gehrels, N.; Geier, S.; Gelbord, J. M.; Gonzalez, L.; Gorjian, V.; Grupe, D.; Hall, P. B.; Hicks, S.; Horenstein, D.; Hutchison, T.; Im, M.; Jensen, J. J.; Joner, M. D.; Jones, J.; Kaspi, S.; Kelly, B. C.; Kennea, J. A.; Kim, M.; Kim, S. C.; Klimanov, S. A.; Lee, J. C.; Leonard, D. C.; Lira, P.; MacInnis, F.; Manne-Nicholas, E. R.; Mathur, S.; McHardy, I. M.; Montouri, C.; Musso, R.; Nazarov, S. V.; Norris, R. P.; Nousek, J. A.; Okhmat, D. N.; Papadakis, I.; Parks, J. R.; Pott, J.-U.; Rafter, S. E.; Rix, H.-W.; Saylor, D. A.; Schimoia, J. S.; Schnülle, K.; Sergeev, S. G.; Siegel, M.; Spencer, M.; Sung, H.-I.; Teems, K. G.; Treu, T.; Turner, C. S.; Uttley, P.; Villforth, C.; Weiss, Y.; Woo, J.-H.; Yan, H.; Young, S.; Zheng, W.-K.

Photometric reverberation mapping of three nearby AGN
***Skielboe, A.**; Watson, D.; Krogager, J.-K. (2016). To be submitted.*

References

Abadi, M. G., Moore, B., & Bower, R. G. 1999, MNRAS, 308, 947

Abell, G. O. 1958, ApJ, 3, 211

Abell, G. O. 1962, in IAU Symposium, Vol. 15, Problems of Extra-Galactic Research, ed. G. C. McVittie, 213

Aihara, H., Allende Prieto, C., An, D., et al. 2011, ApJ, 193, 29

Alam, S., Ata, M., Bailey, S., et al. 2016, ArXiv e-prints, arXiv:1607.03155

Allen, S. W., Mantz, A. B., Morris, R. G., et al. 2013, ArXiv e-prints, arXiv:1307.8152

Altay, G., Colberg, J. M., & Croft, R. A. C. 2006, MNRAS, 370, 1422

Amendola, L., Appleby, S., Bacon, D., et al. 2013, Living Reviews in Relativity, 16, 6

Anderson, K. S. 1970, ApJ, 162, 743

Antonucci, R. 1993, ARA&A, 31, 473

Bahcall, J. N., & Kozlovsky, B.-Z. 1969, ApJ, 155, 1077

Bahcall, J. N., Kozlovsky, B.-Z., & Salpeter, E. E. 1972, ApJ, 171, 467

Bailin, J., & Steinmetz, M. 2005, ApJ, 627, 647

Baldi, A., Ettori, S., Mazzotta, P., Tozzi, P., & Borgani, S. 2007, ApJ, 666, 835

Baldwin, J., Ferland, G., Korista, K., & Verner, D. 1995, ApJ, 455, L119

Balogh, M. L., Navarro, J. F., & Morris, S. L. 2000, ApJ, 540, 113

Barth, A. J., Sarzi, M., Rix, H.-W., et al. 2001, ApJ, 555, 685

Barth, A. J., Pancoast, A., Thorman, S. J., et al. 2011, ApJ, 743, L4

Becker, M. R., & Kravtsov, A. V. 2011, ApJ, 740, 25

Beckmann, V., & Shrader, C. 2012, in An INTEGRAL view of the high-energy sky (the first 10 years), 69

Begelman, M. C., Blandford, R. D., & Rees, M. J. 1984, Reviews of Modern Physics, 56, 255

Begelman, M. C., Volonteri, M., & Rees, M. J. 2006, MNRAS, 370, 289

Bentz, M. C. 2015, ArXiv e-prints, arXiv:1505.04805

Bentz, M. C., Peterson, B. M., Netzer, H., Pogge, R. W., & Vestergaard, M. 2009a, ApJ, 697, 160

Bentz, M. C., Peterson, B. M., Pogge, R. W., & Vestergaard, M. 2009b, ApJ, 694, L166

Bentz, M. C., Walsh, J. L., Barth, A. J., et al. 2008, ApJ, 689, L21

—. 2009c, ApJ, 705, 199

—. 2010a, ApJ, 716, 993

Bentz, M. C., Horne, K., Barth, A. J., et al. 2010b, ApJ, 720, L46

Bentz, M. C., Denney, K. D., Grier, C. J., et al. 2013, ApJ, 767, 149

Bertone, G., Hooper, D., & Silk, J. 2005, Physics Reports, 405, 279

Bian, W., & Gu, Q. 2007, ApJ, 657, 159

Binggeli, B. 1982, Astronomy and Astrophysics, 107, 338

Biviano, A. 2000, in Constructing the Universe with Clusters of Galaxies

Blaes, O. 2014, Space Science Reviews, 183, 21

Blandford, R. D., & McKee, C. F. 1982, ApJ, 255, 419

Blandford, R. D., & Payne, D. G. 1982, MNRAS, 199, 883

Blanton, M. R., & Moustakas, J. 2009, ARA&A, 47, 159

Boselli, A., & Gavazzi, G. 2006, PASP, 118, 517

Bottorff, M., Korista, K. T., Shlosman, I., & Blandford, R. D. 1997, ApJ, 479, 200

Bradač, M., Allen, S. W., Treu, T., et al. 2008, ApJ, 687, 959

Brewer, B. J., Pártay, L. B., & Csányi, G. 2010, DNEST: Diffusive Nested Sampling, Astrophysics Source Code Library, arXiv:0912.2380

Brewer, B. J., Treu, T., Pancoast, A., et al. 2011, ApJ, 733, L33

Brunino, R., Trujillo, I., Pearce, F. R., & Thomas, P. A. 2007, MNRAS, 375, 184

Bruno, G. 1584, On the Infinite Universe and Worlds (1584), ed. D. Goldsmith, 5

Bunn, E. F., & Hogg, D. W. 2009, American Journal of Physics, 77, 688

Byrd, G., & Valtonen, M. 1990, ApJ, 350, 89

Cackett, E. M., & Horne, K. 2006, MNRAS, 365, 1180

Capozziello, S., & de Laurentis, M. 2011, Physics Reports, 509, 167

Carini, M. T., & Ryle, W. T. 2012, ApJ, 749, 70

Carroll, S. M. 2004, Spacetime and geometry: An introduction to general relativity

Cavaliere, A. G., Gursky, H., & Tucker, W. H. 1971, Nature, 231, 437

Chelouche, D., & Daniel, E. 2012, ApJ, 747, 62

Chelouche, D., Daniel, E., & Kaspi, S. 2012, ApJ, 750, L43

Cherepashchuk, A. M., & Lyutyi, V. M. 1973, Astrophysical Letters, 13, 165

Chiang, J., & Murray, N. 1996, ApJ, 466, 704

Chodorowski, M. J. 2011, MNRAS, 413, 585

Choi, J.-H., Shlosman, I., & Begelman, M. C. 2013, ApJ, 774, 149

Choloniewski, J. 1981, Acta Astronomica, 31, 293

Clowe, D., Bradač, M., Gonzalez, A. H., et al. 2006, ApJ, 648, L109

Clowe, D., Gonzalez, A., & Markevitch, M. 2004, ApJ, 604, 596

Colberg, J. M., White, S. D. M., Jenkins, A., & Pearce, F. R. 1999, MNRAS, 308, 593

Cole, S., & Lacey, C. 1996, MNRAS, 281, 716

Colless, M., & Dunn, A. M. 1996, ApJ, 458, 435

Collier, S. J., Horne, K., Kaspi, S., et al. 1998, ApJ, 500, 162

Collin, S., Kawaguchi, T., Peterson, B. M., & Vestergaard, M. 2006, Astronomy and Astrophysics, 456, 75

Copeland, E. J., Sami, M., & Tsujikawa, S. 2006, International Journal of Modern Physics D, 15, 1753

Corless, V. L., & King, L. J. 2009, MNRAS, 396, 315

Cortese, L., Gavazzi, G., Boselli, A., et al. 2006, Astronomy and Astrophysics, 453, 847

Couderc, P. 1939, Annales d'Astrophysique, 2, 271

Cowie, L. L., Barger, A. J., Bautz, M. W., Brandt, W. N., & Garmire, G. P. 2003, ApJ, 584, L57

Dalal, N., Holder, G., & Hennawi, J. F. 2004, ApJ, 609, 50

Danese, L., de Zotti, G., & di Tullio, G. 1980, Astronomy and Astrophysics, 82, 322

Davidson, K. 1972, ApJ, 171, 213

Davis, T. A., Bureau, M., Cappellari, M., Sarzi, M., & Blitz, L. 2013, Nature, 494, 328

De Rosa, G., Peterson, B. M., Ely, J., et al. 2015, ApJ, 806, 128

Denney, K. D. 2012, ApJ, 759, 44

Dodelson, S. 2003, Modern cosmology

Dressler, A. 1980, ApJ, 236, 351

Eddington, A. S. 1926, The Internal Constitution of the Stars

Edelson, R., Vaughan, S., Malkan, M., et al. 2014, ApJ, 795, 2

Edelson, R., Gelbord, J. M., Horne, K., et al. 2015, ApJ, 806, 129

Edelson, R. A., & Krolik, J. H. 1988, ApJ, 333, 646

Edri, H., Rafter, S. E., Chelouche, D., Kaspi, S., & Behar, E. 2012, ApJ, 756, 73

Einstein, A. 1917, Sitzungsberichte der Königlich Preußischen Akademie der Wissenschaften (Berlin), Seite 142-152., 142

Einstein, A., & de Sitter, W. 1932, Proceedings of the National Academy of Science, 18, 213

Eisenstein, D. J., Annis, J., Gunn, J. E., et al. 2001, AJ, 122, 2267

Eisenstein, D. J., Zehavi, I., Hogg, D. W., et al. 2005, ApJ, 633, 560

Ellis, G. F. R. 2006, ArXiv Astrophysics e-prints, astro-ph/0602280

Elvis, M. 2000, ApJ, 545, 63

Erb, D. K. 2015, Nature, 523, 169

Ettori, S., De Grandi, S., & Molendi, S. 2002, Astronomy and Astrophysics, 391, 841

Fabian, A. C. 1994, ARA&A, 32, 277

—. 2012, ARA&A, 50, 455

Fabian, A. C., Zoghbi, A., Ross, R. R., et al. 2009, Nature, 459, 540

Ferland, G. J., Peterson, B. M., Horne, K., Welsh, W. F., & Nahar, S. N. 1992, ApJ, 387, 95

Feroz, F., & Hobson, M. P. 2008, MNRAS, 384, 449

Feroz, F., Hobson, M. P., & Bridges, M. 2009, MNRAS, 398, 1601

Ferrarese, L., & Ford, H. 2005, Space Science Reviews, 116, 523

Ferrarese, L., & Merritt, D. 2000, ApJ, 539, L9

Friedmann, A. 1922, Zeitschrift fur Physik, 10, 377

Fujita, Y. 2004, Publications of the Astronomical Society of Japan, 56, 29

Gaskell, C. M. 2009, New Astronomy Reviews, 53, 140

Gaskell, C. M., & Peterson, B. M. 1987, ApJ, 65, 1

Gaskell, C. M., & Sparke, L. S. 1986, ApJ, 305, 175

Gebhardt, K., Bender, R., Bower, G., et al. 2000, ApJ, 539, L13

Giacconi, R., Murray, S., Gursky, H., et al. 1972, ApJ, 178, 281

Gilbert, K. M., & Peterson, B. M. 2003, ApJ, 587, 123

Gillespie, D. T. 1996, American Journal of Physics, 64, 225

Gladders, M. D., & Yee, H. K. C. 2000, AJ, 120, 2148

Goad, M. R., & Korista, K. T. 2014, MNRAS, 444, 43

—. 2015, MNRAS, 453, 3662

Goad, M. R., Korista, K. T., & Knigge, C. 2004, MNRAS, 352, 277

Goad, M. R., Korista, K. T., & Ruff, A. J. 2012, MNRAS, 426, 3086

Goad, M. R., O'Brien, P. T., & Gondhalekar, P. M. 1993, MNRAS, 263, 149

Gott, III, J. R., & Rees, M. J. 1975, Astronomy and Astrophysics, 45, 365

Gottlöber, S., & Yepes, G. 2007, ApJ, 664, 117

Gottloeber, S., Hoffman, Y., & Yepes, G. 2010, ArXiv e-prints, arXiv:1005.2687

Greene, J. E., Hood, C. E., Barth, A. J., et al. 2010, ApJ, 723, 409

Grier, C. J., Peterson, B. M., Pogge, R. W., et al. 2012, ApJ, 755, 60

Grier, C. J., Martini, P., Watson, L. C., et al. 2013a, ApJ, 773, 90

Grier, C. J., Peterson, B. M., Horne, K., et al. 2013b, ApJ, 764, 47

Guennebaud, G., Jacob, B., et al. 2010, Eigen v3, http://eigen.tuxfamily.org

Haardt, F., & Maraschi, L. 1991, ApJ, 380, L51

Haas, M., Chini, R., Ramolla, M., et al. 2011, Astronomy and Astrophysics, 535, A73

Haehnelt, M. G., & Kauffmann, G. 2000, MNRAS, 318, L35

Haider, M., Steinhauser, D., Vogelsberger, M., et al. 2015, ArXiv e-prints, arXiv:1508.01525

Harvey, D., Massey, R., Kitching, T., Taylor, A., & Tittley, E. 2015, Science, 347, 1462

Hashimoto, Y., Henry, J. P., & Boehringer, H. 2008, MNRAS, 390, 1562

Hasinger, G., Miyaji, T., & Schmidt, M. 2005, Astronomy and Astrophysics, 441, 417

Heckman, T. M., & Best, P. N. 2014, ARA&A, 52, 589

Heisler, C. A., Lumsden, S. L., & Bailey, J. A. 1997, Nature, 385, 700

Hoekstra, H., Yee, H. K. C., & Gladders, M. D. 2004, ApJ, 606, 67

Hönig, S. F. 2014, ApJ, 784, L4

Hönig, S. F., Watson, D., Kishimoto, M., & Hjorth, J. 2014, Nature, 515, 528

Horne, K. 1994, in Astronomical Society of the Pacific Conference Series, Vol. 69, Reverberation Mapping of the Broad-Line Region in Active Galactic Nuclei, ed. P. M. Gondhalekar, K. Horne, & B. M. Peterson, 23–25

Horne, K. 1999, in Astronomical Society of the Pacific Conference Series, Vol. 162, Quasars and Cosmology, ed. G. Ferland & J. Baldwin, 189

Horne, K., Korista, K. T., & Goad, M. R. 2003, MNRAS, 339, 367

Horne, K., Welsh, W. F., & Peterson, B. M. 1991, ApJ, 367, L5

Hubble, E. 1929, Proceedings of the National Academy of Science, 15, 168

Hunter, J. D. 2007, Computing In Science & Engineering, 9, 90

Ishibashi, W., & Fabian, A. C. 2012, MNRAS, 427, 2998

Jauzac, M., Clément, B., Limousin, M., et al. 2014, MNRAS, 443, 1549

Jauzac, M., Jullo, E., Eckert, D., et al. 2015, MNRAS, 446, 4132

Jenkner, H., Lasker, B. M., Sturch, C. R., et al. 1990, AJ, 99, 2082

Jiang, L., Fan, X., Vestergaard, M., et al. 2007, AJ, 134, 1150

Jiang, L., Shen, Y., McGreer, I. D., et al. 2016, ApJ, 818, 137

Joachimi, B., Cacciato, M., Kitching, T. D., et al. 2015, Space Science Reviews, arXiv:1504.05456

Kaiser, N. 2014, MNRAS, 438, 2456

Kasliwal, V. P., Vogeley, M. S., & Richards, G. T. 2015, MNRAS, 451, 4328

Kaspi, S., Brandt, W. N., Maoz, D., et al. 2007, ApJ, 659, 997

Kaspi, S., Maoz, D., Netzer, H., et al. 2005, ApJ, 629, 61

Kaspi, S., Smith, P. S., Netzer, H., et al. 2000, ApJ, 533, 631

Kasun, S. F., & Evrard, A. E. 2005, ApJ, 629, 781

Kelly, B. C., Bechtold, J., & Siemiginowska, A. 2009, ApJ, 698, 895

Kelly, B. C., Becker, A. C., Sobolewska, M., Siemiginowska, A., & Uttley, P. 2014, ApJ, 788, 33

Kelly, B. C., & Merloni, A. 2012, Advances in Astronomy, 2012, 970858

Kelly, B. C., & Shen, Y. 2013, ApJ, 764, 45

Kilerci Eser, E., Vestergaard, M., Peterson, B. M., Denney, K. D., & Bentz, M. C. 2015, ApJ, 801, 8

King, A. L., Davis, T. M., Denney, K. D., Vestergaard, M., & Watson, D. 2014, MNRAS, 441, 3454

King, A. L., Martini, P., Davis, T. M., et al. 2015, MNRAS, 453, 1701

Kinney, A. L., Rivolo, A. R., & Koratkar, A. P. 1990, ApJ, 357, 338

Klypin, A., & Holtzman, J. 1997, ArXiv Astrophysics e-prints, astro-ph/9712217

Klypin, A. A., Trujillo-Gomez, S., & Primack, J. 2011, ApJ, 740, 102

Koester, B. P., McKay, T. A., Annis, J., et al. 2007, ApJ, 660, 239

Koratkar, A. P., & Gaskell, C. M. 1991, ApJ, 75, 719

Korista, K. T., & Goad, M. R. 2004, ApJ, 606, 749

Kormendy, J., & Ho, L. C. 2013, ARA&A, 51, 511

Kormendy, J., & Richstone, D. 1995, ARA&A, 33, 581

Kozłowski, S., Kochanek, C. S., Udalski, A., et al. 2010, ApJ, 708, 927

Krolik, J. H., & Done, C. 1995, ApJ, 440, 166

Krolik, J. H., Horne, K., Kallman, T. R., et al. 1991, ApJ, 371, 541

Latif, M. A., Schleicher, D. R. G., Schmidt, W., & Niemeyer, J. 2013, MNRAS, 433, 1607

Leccardi, A., & Molendi, S. 2008, Astronomy and Astrophysics, 487, 461

Lemaître, G. 1927, Annales de la Société Scientifique de Bruxelles, 47, 49

Libeskind, N. I., Knebe, A., Hoffman, Y., et al. 2011, MNRAS, 411, 1525

Limousin, M., Morandi, A., Sereno, M., et al. 2013, Space Science Reviews, 177, 155

Livio, M., & Riess, A. G. 2013, Physics Today, 66, 41

Lotz, J., Mountain, M., Grogin, N. A., et al. 2014, in American Astronomical Society Meeting Abstracts, Vol. 223, American Astronomical Society Meeting Abstracts, 254.01

LSST Science Collaboration, Abell, P. A., Allison, J., et al. 2009, ArXiv e-prints, arXiv:0912.0201

Lundmark, K. 1924, MNRAS, 84, 747

MacLeod, C. L., Ivezić, Ž., Kochanek, C. S., et al. 2010, ApJ, 721, 1014

Magorrian, J., Tremaine, S., Richstone, D., et al. 1998, AJ, 115, 2285

Marconi, A., Axon, D. J., Maiolino, R., et al. 2008, ApJ, 678, 693

Markevitch, M., Gonzalez, A. H., Clowe, D., et al. 2004, ApJ, 606, 819

Mathews, W. G., Blumenthal, G. R., & Grandi, S. A. 1980, ApJ, 235, 971

Mathur, S. 2000, MNRAS, 314, L17

McCarthy, I. G., Schaye, J., Ponman, T. J., et al. 2010, MNRAS, 406, 822

McHardy, I. M., Arévalo, P., Uttley, P., et al. 2007, MNRAS, 382, 985

McHardy, I. M., Cameron, D. T., Dwelly, T., et al. 2014, MNRAS, 444, 1469

McLure, R. J., & Jarvis, M. J. 2002, MNRAS, 337, 109

Meneghetti, M., Rasia, E., Merten, J., et al. 2010, Astronomy and Astrophysics, 514, A93

Merloni, A., & Heinz, S. 2008, MNRAS, 388, 1011

Metzroth, K. G., Onken, C. A., & Peterson, B. M. 2006, ApJ, 647, 901

Miyoshi, M., Moran, J., Herrnstein, J., et al. 1995, Nature, 373, 127

More, A., Cabanac, R., More, S., et al. 2012, ApJ, 749, 38

Mushotzky, R. F., Edelson, R., Baumgartner, W., & Gandhi, P. 2011, ApJ, 743, L12

Navarro, J. F., Frenk, C. S., & White, S. D. M. 1997, ApJ, 490, 493

Nelson, C. H., Green, R. F., Bower, G., Gebhardt, K., & Weistrop, D. 2004, ApJ, 615, 652

Nelson, D., Vogelsberger, M., Genel, S., et al. 2013, MNRAS, 429, 3353

Nelson, D., Pillepich, A., Genel, S., et al. 2015, Astronomy and Computing, 13, 12

Netzer, H. 2003, ApJ, 583, L5

—. 2015, ARA&A, 53, 365

Newton, I. 1687, Philosophiae Naturalis Principia Mathematica. Auctore Js. Newton, doi:10.3931/e-rara-440

Newton, I. 1692, Original letter from Isaac Newton to Richard Bentley, dated 17 January 1692/3

Niederste-Ostholt, M., Strauss, M. A., Dong, F., Koester, B. P., & McKay, T. A. 2010, MNRAS, 405, 2023

O'Brien, P. T., Goad, M. R., & Gondhalekar, P. M. 1995, MNRAS, 275, 1125

Onken, C. A., Ferrarese, L., Merritt, D., et al. 2004, ApJ, 615, 645

Osterbrock, D. E., & Pogge, R. W. 1985, ApJ, 297, 166

Pancoast, A., Brewer, B. J., & Treu, T. 2011, ApJ, 730, 139

—. 2014a, MNRAS, 445, 3055

Pancoast, A., Brewer, B. J., Treu, T., et al. 2014b, MNRAS, 445, 3073

Park, D., Woo, J.-H., Treu, T., et al. 2012, ApJ, 747, 30

Peebles, P. J., & Ratra, B. 2003, Reviews of Modern Physics, 75, 559

Peebles, P. J. E. 1974, Astronomy and Astrophysics, 32, 197

—. 1980, The large-scale structure of the universe

Peebles, P. J. E., & Dicke, R. H. 1968, ApJ, 154, 891

Pei, L., Barth, A. J., Aldering, G. S., et al. 2014, ApJ, 795, 38

Penston, M. V. 1991, in Variability of Active Galactic Nuclei, ed. H. R. Miller & P. J. Wiita, 343

Perez, E., Robinson, A., & de La Fuente, L. 1992, MNRAS, 256, 103

Perlmutter, S., Aldering, G., Goldhaber, G., et al. 1999, ApJ, 517, 565

Peterson, B. M. 1993, PASP, 105, 247

—. 1997, An Introduction to Active Galactic Nuclei

Peterson, B. M., & Wandel, A. 2000, ApJ, 540, L13

Peterson, B. M., Wanders, I., Bertram, R., et al. 1998a, ApJ, 501, 82

Peterson, B. M., Wanders, I., Horne, K., et al. 1998b, PASP, 110, 660

Peterson, B. M., Denney, K. D., De Rosa, G., et al. 2013, ApJ, 779, 109

Phillips, D. L. 1962, Journal of the ACM (JACM), 9, 84

Piffaretti, R., & Valdarnini, R. 2008, Astronomy and Astrophysics, 491, 71

Pijpers, F. P., & Wanders, I. 1994, MNRAS, 271, 183

Planck Collaboration, Ade, P. A. R., Aghanim, N., et al. 2016, Astronomy and Astrophysics, 594, A13

Planelles, S., Borgani, S., Fabjan, D., et al. 2014, MNRAS, 438, 195

Pogge, R. W., & Peterson, B. M. 1992, AJ, 103, 1084

Pozo Nuñez, F., Ramolla, M., Westhues, C., et al. 2012, Astronomy and Astrophysics, 545, A84

Pozo Nuñez, F., Westhues, C., Ramolla, M., et al. 2013, Astronomy and Astrophysics, 552, A1

Pozo Nuñez, F., Ramolla, M., Westhues, C., et al. 2015, Astronomy and Astrophysics, 576, A73

Press, W. H. 1992, Numerical recipes in Fortran 77: the art of scientific computing, Vol. 1 (Cambridge university press)

Ramos Almeida, C., Martínez González, M. J., Asensio Ramos, A., et al. 2016, MNRAS, 461, 1387

Rapetti, D., Allen, S. W., Mantz, A., & Ebeling, H. 2010, MNRAS, 406, 1796

Rapetti, D., Blake, C., Allen, S. W., et al. 2013, MNRAS, 432, 973

Rees, M. J. 1984, ARA&A, 22, 471

Reshetnikov, V. P. 2005, Physics Uspekhi, 48, 1109

Riebe, K., Partl, A. M., Enke, H., et al. 2011, ArXiv e-prints, arXiv:1109.0003

Riess, A. G., Macri, L. M., Hoffmann, S. L., et al. 2016, ApJ, 826, 56

Robertson, H. P. 1935, ApJ, 82, 284

Robinson, A., & Perez, E. 1990, MNRAS, 244, 138

Roediger, E., & Hensler, G. 2005, Astronomy and Astrophysics, 433, 875

Rozo, E., Rykoff, E. S., Koester, B. P., et al. 2009, ApJ, 703, 601

Rozo, E., Wechsler, R. H., Rykoff, E. S., et al. 2010, ApJ, 708, 645

Ryden, B. 2003, Introduction to cosmology

Rykoff, E. S., Koester, B. P., Rozo, E., et al. 2012, ApJ, 746, 178

Rykoff, E. S., Rozo, E., Busha, M. T., et al. 2014, ApJ, 785, 104

Salamanca, I., Alloin, D., Baribaud, T., et al. 1994, Astronomy and Astrophysics, 282, 742

Salpeter, E. E. 1964, ApJ, 140, 796

Samsing, J., Skielboe, A., & Hansen, S. H. 2012, ApJ, 748, 21

Sarazin, C. L. 1986, Reviews of Modern Physics, 58, 1

Saro, A., Mohr, J. J., Bazin, G., & Dolag, K. 2013, ApJ, 772, 47

Sarzi, M., Rix, H.-W., Shields, J. C., et al. 2001, ApJ, 550, 65

Schawinski, K., Thomas, D., Sarzi, M., et al. 2007, MNRAS, 382, 1415

Schlafly, E. F., & Finkbeiner, D. P. 2011, ApJ, 737, 103

Schmidt, B. P., Suntzeff, N. B., Phillips, M. M., et al. 1998, ApJ, 507, 46

Scoville, N., Aussel, H., Brusa, M., et al. 2007, ApJ, 172, 1

Sergeev, S. G., Doroshenko, V. T., Dzyuba, S. A., et al. 2007, ApJ, 668, 708

Sergeev, S. G., Pronik, V. I., & Sergeeva, E. A. 2001, ApJ, 554, 245

Serlemitsos, P. J., Smith, B. W., Boldt, E. A., Holt, S. S., & Swank, J. H. 1977, ApJ, 211, L63

Seyfert, C. K. 1943, ApJ, 97, 28

Shaw, L. D., Weller, J., Ostriker, J. P., & Bode, P. 2006, ApJ, 646, 815

Shen, Y. 2013, Bulletin of the Astronomical Society of India, 41, 61

Shen, Y., Richards, G. T., Strauss, M. A., et al. 2011, ApJ, 194, 45

Shen, Y., Brandt, W. N., Dawson, K. S., et al. 2015, ApJ, 216, 4

Sijacki, D., Vogelsberger, M., Genel, S., et al. 2015, MNRAS, 452, 575

Silk, J. 2013, ApJ, 772, 112

Silk, J., & Rees, M. J. 1998, Astronomy and Astrophysics, 331, L1

Silverman, J. D., Green, P. J., Barkhouse, W. A., et al. 2008, ApJ, 679, 118

Skielboe, A., Pancoast, A., Treu, T., et al. 2015, MNRAS, 454, 144

Skielboe, A., Wojtak, R., Pedersen, K., Rozo, E., & Rykoff, E. S. 2012, ApJ, 758, L16

Skilling, J., & Bryan, R. K. 1984, MNRAS, 211, 111

Slipher, V. M. 1915, Popular Astronomy, 23, 21

Sparke, L. S. 1993, ApJ, 404, 570

Sparre, M., & Hansen, S. H. 2012, JCAP, 7, 42

Springel, V., White, S. D. M., Jenkins, A., et al. 2005, Nature, 435, 629

Strassmeier, K. G., Granzer, T., Weber, M., et al. 2001, Astronomische Nachrichten, 322, 287

—. 2004, Astronomische Nachrichten, 325, 527

Strateva, I. V., Strauss, M. A., Hao, L., et al. 2003, AJ, 126, 1720

Strauss, M. A., Weinberg, D. H., Lupton, R. H., et al. 2002, AJ, 124, 1810

Tadhunter, C. 2016, Astronomy & Astrophysics Reviews, 24, 10

Tanaka, M., Kodama, T., Arimoto, N., et al. 2005, MNRAS, 362, 268

Tanaka, Y., Nandra, K., Fabian, A. C., et al. 1995, Nature, 375, 659

Taylor, J. R. 1982, An introduction to error analysis. The study of uncertainties in physical measurements

Tikhonov, A. 1963, in Soviet Math. Dokl., Vol. 5, 1035–1038

Tonry, J. L., Dressler, A., Blakeslee, J. P., et al. 2001, ApJ, 546, 681

Tormen, G. 1997, MNRAS, 290, 411

Tremaine, S., Gebhardt, K., Bender, R., et al. 2002, ApJ, 574, 740

Trevese, D., Perna, M., Vagnetti, F., Saturni, F. G., & Dadina, M. 2014, ApJ, 795, 164

Tully, R. B., Rizzi, L., Shaya, E. J., et al. 2009, AJ, 138, 323

Ueda, Y., Akiyama, M., Ohta, K., & Miyaji, T. 2003, ApJ, 598, 886

Ulrich, M.-H., & Horne, K. 1996, MNRAS, 283, 748

Ulrich, M.-H., Maraschi, L., & Urry, C. M. 1997, ARA&A, 35, 445

Umemura, M. 2001, ApJ, 560, L29

Urry, C. M., & Padovani, P. 1995, PASP, 107, 803

van de Voort, F., Schaye, J., Booth, C. M., Haas, M. R., & Dalla Vecchia, C. 2011, MNRAS, 414, 2458

van Uitert, E., Hoekstra, H., Schrabback, T., et al. 2012, ArXiv e-prints, arXiv:1206.4304

Vanden Berk, D. E., Richards, G. T., Bauer, A., et al. 2001, AJ, 122, 549

Vaughan, S., Edelson, R., Warwick, R. S., & Uttley, P. 2003, MNRAS, 345, 1271

Vestergaard, M. 2002, ApJ, 571, 733

—. 2004, ApJ, 601, 676

—. 2011, Black-hole masses of distant quasars, ed. M. Livio & A. M. Koekemoer, 150–172

Vestergaard, M., & Peterson, B. M. 2006, ApJ, 641, 689

Vio, R., Horne, K., & Wamsteker, W. 1994, PASP, 106, 1091

Visvanathan, N., & Sandage, A. 1977, ApJ, 216, 214

Vogelsberger, M., Genel, S., Springel, V., et al. 2014, MNRAS, 444, 1518

Voit, G. M. 2005, Reviews of Modern Physics, 77, 207

Vollmer, B., Cayatte, V., Balkowski, C., & Duschl, W. J. 2001, ApJ, 561, 708

Volonteri, M., Haardt, F., & Madau, P. 2003, ApJ, 582, 559

Wagoner, R. V. 1969, ARA&A, 7, 553

Walsh, J. L., Minezaki, T., Bentz, M. C., et al. 2009, ApJ, 185, 156

Wandel, A., Peterson, B. M., & Malkan, M. A. 1999, ApJ, 526, 579

Wanders, I., & Peterson, B. M. 1996, ApJ, 466, 174

Wanders, I., Goad, M. R., Korista, K. T., et al. 1995, ApJ, 453, L87

Watson, D., Denney, K. D., Vestergaard, M., & Davis, T. M. 2011, ApJ, 740, L49

Weinberg, D. H., Mortonson, M. J., Eisenstein, D. J., et al. 2013, Physics Reports, 530, 87

Welsh, W. F., & Horne, K. 1991, ApJ, 379, 586

Wheeler, J. A. 1990, A journey into gravity and spacetime

White, M., Cohn, J. D., & Smit, R. 2010, MNRAS, 408, 1818

White, R. J., & Peterson, B. M. 1994, PASP, 106, 879

Wilson, A. S., & Heckman, T. M. 1985, in Astrophysics of Active Galaxies and Quasi-Stellar Objects, ed. J. S. Miller, 39–109

Winkler, H. 1997, MNRAS, 292, 273

Wojtak, R., Hansen, S. H., & Hjorth, J. 2011, Nature, 477, 567

Wojtak, R., & Łokas, E. L. 2010, MNRAS, 408, 2442

Woo, J.-H. 2008, AJ, 135, 1849

Woo, J.-H., & Urry, C. M. 2002, ApJ, 579, 530

Woo, J.-H., Treu, T., Barth, A. J., et al. 2010, ApJ, 716, 269

Yang, H.-Y. K., & Reynolds, C. S. 2016, ArXiv e-prints, arXiv:1605.01725

Zensus, J. A. 1997, ARA&A, 35, 607

Zu, Y., Kochanek, C. S., Kozłowski, S., & Peterson, B. M. 2016, ApJ, 819, 122

Zu, Y., Kochanek, C. S., Kozłowski, S., & Udalski, A. 2013, ApJ, 765, 106

Zu, Y., Kochanek, C. S., & Peterson, B. M. 2011, ApJ, 735, 80

Zwicky, F. 1933, Helvetica Physica Acta, 6, 110

Zwicky, F., Herzog, E., & Wild, P. 1968, Catalogue of galaxies and of clusters of galaxies